Justus-Liebig-Universität Giessen

Institut für Theoretische Physik I

Fachbereich 07 - Mathematik und Informatik, Physik, Geographie

Diplomarbeit

Superscaling analysis of inclusive lepton-nucleus scattering reactions simulated in the GiBUU model

Vorgelegt von:

Ivan Lappo-Danilevski

November 8, 2010

Contents

Chapter 1

Introduction

> *"Just now nuclear physicists are writing a great deal about hypothetical particles called neutrinos supposed to account for certain peculiar facts observed in β-ray disintegration. ... I am not much impressed by the neutrino theory. In an ordinary way I might say that I do not believe in neutrinos. ... But I have to reflect that a physicist may be an artist, and you never know where you are with artists. ... Whatever I may think, I am not going to be lured into a wager against the skill of experimenters under the impression that it is a wager against the truth of a theory. If they succeed in making neutrinos, perhaps even in developing industrial applications of them, I suppose I shall have to believe – though I may feel that they have not been playing quite fair."*
>
> Sir Arthur Stanley Eddington, The Philosophy of Physical Science (1939).

Even though, more than eighty years after the proposal of extremely weakly interacting particles by Wolfgang Pauli and more than fifty years after their experimental discovery [RC53], the existence of neutrinos is beyond doubt, our knowledge about these particles is still incomplete. The weak interaction, that couples neutrinos to matter and, due to its lack of strength, makes experimental analyses very demanding, has been shown to greatly resemble the electromagnetic force. As a consequence, modern descriptions regard the neutrino observed in β-decay as a partner particle of the electron, both belonging to the group of leptons.

With the electromagnetic interaction being well understood and all properties of the electron determined with high precision, the electron has in many experiments served as a probe for the analysis of more complex systems, yet not subject to consistent theoretical descriptions, e.g., the nucleus or the nucleon. As the neutrinos couple to additional degrees of freedom, scattering neutrinos on these systems can be a valuable source of information that cannot be obtained from electron-scattering experiments.

In our opinion, the paths of gaining new insight in the fields of neutrino, nuclear and particle physics are intertwined. At certain passages in this work, we will explain how information obtained from neutrino-scattering experiments resolve questions posed by other experiments, how electron-scattering experiments motivate model building for the description of complex systems and why such models are an indispensable tool for the analysis of experiments that aim to determine fundamental neutrino properties. The ambition of this thesis is to shed light on the connections between the aforementioned fields of physics and investigate how progress in the theoretical understanding of lepton-nucleus scattering can be made.

1.1 Motivation

Neutrino physics

To understand why neutrino physics is receiving much attention at the present time, it is necessary to review the status of particle physics two decades ago: With electroweak theory successfully describing lepton-hadron and lepton-lepton interactions and quantum chromodynamics (QCD) describing many aspects of the hadron sector, the standard model of particle physics stood as a framework of unchallenged predictive power. Within this model the neutrino was assumed to be a massless, point-like uncharged particle of spin 1/2, only participating in weak reactions and coming in three flavors, corresponding to the three flavors of the charged leptons, e, μ, τ. Much attention was drawn to the Higgs boson, which was believed to be the last building block of the theory, not yet assessed experimentally.

The fact that the standard-model calculations of the neutrino flux from the sun significantly overestimated the experimentally observed flux was a long-standing puzzle pointing towards physics beyond the standard model. It was hence a startling discovery when the SNO experiment [AAA$^+$01] confirmed neutrino oscillations to be the cause of the observed discrepancy, implying that, contrary to previous beliefs, neutrinos do have a non-vanishing mass and its flavors are mixed by the weak interaction.

Aiming at extending the standard model so that it incorporates neutrino oscillations, one thus has to introduce new input parameters to the theory, namely the masses of the three neutrino mass eigenstates and the three mixing angles θ_{12}, θ_{23} and θ_{13}. While neutrino-oscillation experiments are sensitive to the mixing angles and differences of the squared masses, the precise measurement of the kinematics of the β decay, e.g., with the KATRIN experiment [W$^+$02], offers a possibility to determine upper limits for the absolute mass value, the current limit being $m_{\nu_e} < 2.3$ eV [K$^+$05]. Whether neutrino mixing involves a CP-violating phase, δ, similar to the quark mixing, is also a yet unanswered question[1].

To find reliable answers to these questions, various experiments around the world are being installed or have already taken data. A promising approach are long-baseline experiments [K2K, Mina, MINb, T2K, OPE], aiming at the precise determination of neutrino-oscillation parameters by measuring the interaction of neutrinos with a nuclear target at a long distance from the accelerator, that created the initial neutrino beam. As security reasons do not permit to perform scattering experiments on large hydrogen or deuterium targets, experimentalists aiming to determine neutrino properties are nevertheless forced to employ nuclear targets, having thus to deal with both the uncertain neutrino-nucleon and neutrino-nucleus responses.

[1] It is important to note that the current research goes beyond this minimal extension of the standard model, e.g., by discussing the question if the neutrino mass eigenstates are Dirac or Majorana particles, leading to experimental investigations whether neutrinoless double-beta decay is possible. In this work however, we focus on oscillation-related problems.

Nuclear physics

With the nucleus being a complex system composed of interacting nucleons, that themselves are systems of interacting particles, the correct description of the nuclear ground state is a highly demanding task. Phenomenological parameterizations of ground-state properties, such as the semi-empirical mass formula derived from the liquid-drop model, were among the first successful descriptions of the nuclear ground state. Later, these parameterizations were refined by quantum mechanical shell models, and certain nuclear properties were addressed in quantum-field theory based approaches.

To this day, different properties of the nucleus are handled with very different, partly contradicting models. Nuclear binding energies are, e.g., well described by quantum-mechanical many-body theory, while for scattering reactions it is useful to regard the nucleons as quasifree within the nucleus. Many intrinsic nuclear properties, as the momentum distribution, can up to this day not be directly extracted from experimental data, while their knowledge would be helpful for model building and model validation. And even though electron-scattering experiments were among the first to shed light on the nucleus, some properties of the response in electron scattering experiments, as the non-resonant pion background or the excess of transverse strength are still puzzling.

Nucleon physics

Great progress has been made in the description of the hadronic sector, when, based on the results of electron-scattering experiments, the nucleon was described as consisting of three basic building blocks, the so called constituent quarks, subject to the laws of quantum chromodynamics. The explicit form of the response, however, can up to this day not be calculated from these principles and has been parametrized into form factors. Since data for pure neutrino-nucleon scattering are very scarce, and, due to security reasons, hard to reproduce in future experiments, the neutrino-nucleon form factors constitute a major uncertainty for all neutrino-scattering experiments.

Nevertheless neutrino scattering has been a valuable source of information in addition to electron scattering in the field of hadron physics. It is, e.g., possible to determine the charge of the up and down quark by comparing the form factors obtained from electron- and neutrino-nucleon scattering. As understanding of the nuclear part of the interaction will hopefully increase, we are confident that the data gathered in upcoming neutrino-scattering experiments will also contribute to a better understanding of the nucleon structure.

To conclude, we state that the fields of neutrino, particle and nuclear physics are intertwined, with the combined output having a fundamental impact on our picture of nature at the smallest length scales. With this work, we hope to contribute to the theoretical understanding of the relations between nuclear and neutrino physics, and, more precisely, to derive techniques how the description of lepton-nucleus scattering experiments can be improved.

1.2 Survey

In order to describe the nuclear response to electron scattering, different models have been developed. While at low energy transfers collective modes, like the giant dipole resonance, play a role, for medium energy transfers the interaction is often treated in impulse approximation, i.e., the scattering partner of the electron is assumed to be a quasi-free nucleon. From these considerations the Fermi-gas model [dFW66] was developed, its relativistic formulation and successful application to electron scattering [MSW+71] has inspired the analysis of neutrino scattering in an analogous model [SM72]. Through the use of refined spectral functions and momentum distributions [BPP93], effects beyond the simple Fermi-gas picture were explained and the impact on neutrino-scattering reactions has been studied [BFN+05]. Other treatments have included direct contributions from many-body terms, e.g., 2p-2h meson-exchange currents [DPNA+04], as a refinement to the impulse approximation picture.

On the experimental side, the main focus resides on the inclusive cross section. With the appearance of more data sets, other quantities, e.g., the longitudinal and transverse response [ACD+80] could be extracted, leading to the development of more refined theories. Recently the superscaling analysis, by means of which the responses of different targets at different scattering kinematics can be directly related [DS99], has emerged as a powerful analysis tool. This approach can also be used to predict neutrino-scattering cross sections from electron-scattering data [ABC+05].

In this work we will present a model, based on the impulse approximation and a refined relativistic Fermi gas, that also includes additional nuclear effects, e.g., spectral functions and a hadronic potential. We will show that our model is able to describe electron-nucleus scattering reactions at incoming electron energies of a few GeV. In the following, we will also compare predictions for the longitudinal and transverse responses to experimental data. Finally, we argue that our model is apt to predict the neutrino-nucleus response and also point out uncertainties inherent in any description dealing with neutrino interactions.

1.3 Outline

This work is organized as follows. It is our aim to guide the reader from the fundamental formalism forming the basis of our investigation, presented in Chapters 2, 3 and 4, to the actual implementation of our model in Chapter 5 and its application to current fields of research in Chapter 6.

In Chapter 2, we begin by describing the fundamental interactions on the lepton quark and lepton-nucleon level. Passing to the more complex system of the nucleus, in Chapter 3 we consider important aspects of model building. Most of these ideas are taken up in Chapter 4, where they serve as a motivation for the development of different scaling and superscaling approaches. In Chapter 5, we present our model for the description of lepton-nucleus scattering, which is then applied to current fields of research in Chapter 6. Finally, we draw conclusions from our work in Chapter 7 and also consider ways to further extend this line of research. In addition, the interested reader may find the technical details of our work, e.g., nomenclature and programming related issues, in the appendix.

Chapter 2

Elementary lepton-nucleon interactions

In this chapter we will present different aspects of lepton-nucleon scattering. Starting out with the explanation of the underlying microscopic dynamics in the first section, we then develop a formalism for expressing inclusive cross sections and, in the last three sections, shed light on the most important contributions.

2.1 Electroweak interaction

The interplay between leptons and quarks is governed by the electroweak interaction. Thus, the standard model of particle physics describing the interaction's various parameters is the theoretical basis of most of this work. In this section, we will outline these underlying connections, whereas an explanation of the notations can be found in Appendix A. For a more complete treatment, the reader might consult the literature on this topic, e.g., Refs. [HM08], [PS95] and [Mos99].

2.1.1 Cross sections and Lagrange formalism

A basic connection is made between theories describing hadronic degrees of freedom and particle-accelerator experiments by comparing predicted cross sections with measured ones. While for the experimentalist the cross section is geometrically motivated and, in the most simple case, related to the detector setup and signal by

$$\frac{\text{(number of measured reactions)}}{\text{(number of incoming particles)}} = \frac{\text{(number of target particles} \times \sigma)}{\text{(area of target zone)}}, \tag{2.1}$$

for the theorist the cross section, σ, has the probabilistic interpretation

$$\sigma = \frac{|T_{fi}|^2}{TV} \frac{\text{(number of final states)}}{\text{(initial flux)}}. \tag{2.2}$$

Here, $|T_{fi}|^2$ denotes the quantum mechanical transition probability from the initial state, $|i\rangle$, to the final state, $|f\rangle$, T the time interval of interaction and V a reference volume, while the other parameters depend on the specific process and will be discussed in more detail within the next section.

Assuming minor depletion of the initial state, one can make the first-order perturbation theory ansatz

$$T_{fi} = -\mathrm{i} \int \mathrm{d}^4x \; \phi_f^*(x) V_{\mathrm{int}}(x) \phi_i(x), \tag{2.3}$$

where $\phi_{i(f)}$ stands for the initial-(final-)state wave functions, while $V_{\mathrm{int}}(x)$ represents the interaction potential. Carrying out the integration for the incoming $I_1, \ldots, I_N$ and the outgoing $O_1, \ldots, O_M$ particles will, in general, always yield

$$T_{fi} = -\mathrm{i} N_{I_1} \ldots N_{I_N} N_{O_1} \ldots N_{O_M} (2\pi)^4 \delta^{(4)}(p_{O_1} + \ldots + p_{O_M} - p_{I_1} - \ldots - p_{I_N}) \mathcal{M}. \tag{2.4}$$

While N_I and N_O represent normalization factors and the δ-distribution ensures conservation of four-momentum, the interesting physics is contained within the invariant matrix element, $\mathcal{M}$. It can be directly related to Feynman diagrams of current-current interactions mediated through virtual bosons and fermions. The rules for translating the Feynman diagrams to mathematical expressions can be derived, as shown in Ref. [Sre07], by means of path integrals from the Lagrangian density, $\mathcal{L}$, which represents the action measure of the system.

Though Eq. (2.2) shows a first-order approximation, by performing a series expansion of the weight factor, $\exp(\int \mathrm{d}^4x\mathcal{L})$, associated with each path, one is able to derive expressions for arbitrary orders. These expressions can be interpreted physically through representation as Feynman diagrams. Knowing the complete Lagrangian of the system thus means knowing the structure of all contributions to a certain transition and even though the explicit calculations become more and more intricate with higher orders, impressive agreement of theoretical predictions with high-precision experiments, e.g., the measurement of the anomalous magnetic dipole moment of the electron, gives a proof of concept.

Keeping in mind that the Lagrangian approach is one valid description amongst different ones, we will take it as our starting point, since it is manifestly covariant and easily incorporates the principles of gauge invariance and spontaneous symmetry breaking to motivate the introduction of interacting massive boson fields.

2.1.2 Interaction Lagrangian

Within today's standard model of electroweak interactions the main focus lies on leptons, quarks and their interactions. The lepton family consists of the charged particles e, μ, τ and the uncharged neutrinos ν_e, ν_μ, ν_τ, while quarks come in the flavors u, d, s, c, t and b. As a starting point each fermion is assigned a spinor, f, and the free Lagrangian density

$$\mathcal{L}_0 = \mathrm{i}\bar{f}(\gamma_\mu \partial^\mu - m_f \mathbb{1}_{4\times 4}) f. \tag{2.5}$$

By assuming local $\mathrm{SU}(2) \times \mathrm{U}(1)$ gauge invariance, one is led to the introduction of the gauge fields $\mathbf{W}^\mu$ and B^μ, which are initially massless. Their self-interactions and kinetic energies read

$$\mathcal{L}_{\mathrm{SU}(2)\times\mathrm{U}(1)} = -\frac{1}{4}\mathbf{W}_{\mu\nu}\mathbf{W}^{\mu\nu} - \frac{1}{4}B_{\mu\nu}B^{\mu\nu}. \tag{2.6}$$

To transform them into the observed massless photon field, A, and the massive exchange bosons, $W^\pm, Z^0$, one introduces the Higgs field. This $\mathrm{SU}(2) \times \mathrm{U}(1)_Y$ doublet of 2 complex fields generates the masses of both, bosons and, as a side effect, fermions, through spontaneous symmetry breaking. By then rotating through the Weinberg angle, θ_W, one obtains the observed field degrees of freedom. The interaction Lagrangian, which will allow us to calculate all contributions except for the self-coupling of the gauge fields, then reads[1]

$$\mathcal{L}_{int} = -eJ^\mu_{\mathrm{EM}}A_\mu - \frac{g}{2\sqrt{2}}(J^\mu_{\mathrm{CC}}W^\dagger_\mu + h.c.) - \frac{g}{2\cos\theta_W}J^\mu_{\mathrm{NC}}Z_\mu. \tag{2.7}$$

2.1.3 Electroweak currents

Provided with expressions for the electromagnetic current, J^μ_{EM}, the weak charged current, J^μ_{CC}, and the weak neutral current, J^μ_{NC}, one can directly extract the most important processes from the above equation. In order to keep the example simple, we will restrict the lepton sector to the electron and its SU(2)-partner and the quark sector to the u and d quarks, which carry the charge fractions $Q_u = \frac{2}{3}$ and $Q_d = -\frac{1}{3}$.

The photon field, A, only couples to electrically charged particles. Hence, the electromagnetic current reads

$$J^\mu_{EM} = Q_u\bar{q}_u\gamma^\mu q_u + Q_d\bar{q}_d\gamma^\mu q_d + Q_e\bar{e}\gamma^\mu e = \frac{2}{3}\bar{q}_u\gamma^\mu q_u - \frac{1}{3}\bar{q}_d\gamma^\mu q_d - \bar{e}\gamma^\mu e. \tag{2.8}$$

Apart from mixing the flavors, as will be described in the next subsection, the charged $W^\pm$ bosons maximally violate parity since they couple to left-handed currents only. This is manifest in the use of the $(1-\gamma^5)$ projection operator for the charged current,

$$J^\mu_{CC} = \bar{q}_u\gamma^\mu(1-\gamma^5)q'_d + \bar{\nu}'_e\gamma^\mu(1-\gamma^5)e. \tag{2.9}$$

One speaks of the current having a "V - A" structure, as the vector component, γ^μ, enters with a positive and the axial vector component, $\gamma^\mu\gamma^5$, with a negative sign[2].

Parity is also violated by the neutral current through the operator $(c^f_{\mathrm{V}} - c^f_{\mathrm{A}})\gamma^5$. The axial-vector couplings are given by $c^f_{\mathrm{A}} = T^3_f$ and $c^f_{\mathrm{V}} = T^3_f - 2\sin^2\theta_W Q_f$, with respect to the fermion charge and third component of the weak isospin, T^3_f. They yield maximal violation only for the neutrinos as can be seen in the expression for the neutral current

$$\begin{aligned} J^\mu_{NC} = {} & \bar{q}_u\gamma^\mu\left(\frac{1}{2} - \frac{4}{3}\sin^2\theta_W - \frac{1}{2}\gamma^5\right)q_u + \bar{q}_d\gamma^\mu\left(-\frac{1}{2} + \frac{2}{3}\sin^2\theta_W + \frac{1}{2}\gamma^5\right)q_d \\ & + \bar{e}\gamma^\mu\left(-\frac{1}{2} + 2\sin^2\theta_W + \frac{1}{2}\gamma^5\right)e + \bar{\nu}_e\gamma^\mu\left(\frac{1}{2} - \frac{1}{2}\gamma^5\right)\nu_e. \end{aligned} \tag{2.10}$$

In order to describe current-current scattering, it suffices to insert one of both currents directly into Eq. (2.7) while the other current is plugged in as the source of the potential. The first-order contributions can thus be directly read out. In Fig. 2.1 we depict the most important processes: electromagnetically charged fermions can scatter with each other by exchanging a virtual photon, all fermions can transform into their SU(2)-partner by exchanging a $W^\pm$ boson, all fermions can scatter with other fermions by exchanging a Z^0 boson.

[1] The coupling constant, g, is defined in Appendix A.

[2] This ansatz will be used throughout the following sections for more involved electroweak currents.

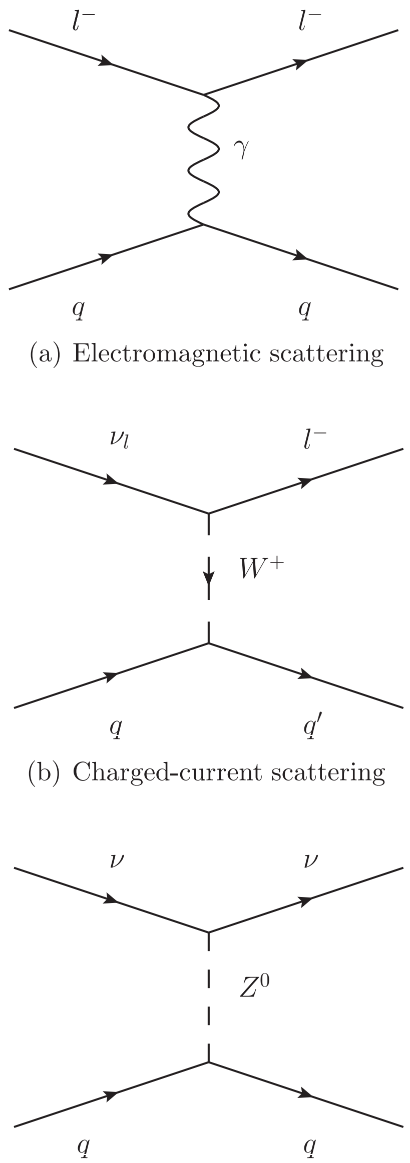

(a) Electromagnetic scattering

(b) Charged-current scattering

(c) Neutral-current scattering

Figure 2.1: First-order electroweak interactions.

2.1.4 Mixing matrices and neutrino oscillations

Apart from giving masses to the gauge bosons, an especially beautiful aspect of the Higgs mechanism is the inclusion of fermion masses. This is actually a necessity, since the simple mass term in the free Lagrangian from Eq. (2.5) is not gauge invariant under chiral SU(2) rotations which act on left-handed components of the spinors only. The new gauge-invariant mass terms read

$$\mathcal{L}_{\text{mass}} = -m_f \bar{f} f \left(1 + \frac{h}{v}\right) \tag{2.11}$$

where m_f are the experimentally found masses of the fermions and are thus input parameters to the theory. Note that experimental evidence for the second term containing a coupling to the Higgs field, h, is still missing, which might be due to the large value of the vacuum expectation value of the Higgs field after spontaneous symmetry breaking, $v/\sqrt{2} = 246/\sqrt{2}$ GeV.

For reasons not yet understood, the W-boson does not couple directly to the mass eigenstates, but to a mixture thereof. Established convention reduces the mixing to the d, s, b-quarks and the neutrinos. Mixing of the quarks is accomplished through the Cabibbo-Kobayashi-Maskawa matrix U^{CKM}, by means of which u'_d from Eq. (2.9) is expressed as

$$q'_d = U^{\text{CKM}}_{di} q_i \mid i \in \{d, s, b\}. \tag{2.12}$$

Similarly, the leptons are transformed by the Pontecorvo-Maki-Nakagawa-Sakata matrix, U^{PMNS}, in the following way

$$\nu'_e = U^{\text{PMNS}}_{ei} \nu_i \mid i \in \{1, 2, 3\}. \tag{2.13}$$

Whereas the three rotation angles and the CP-violating complex phase parameterizing the CKM-matrix are experimentally assessed with more and more precision, the values in the PNMS-matrix are still subject to uncertainties (cf., e.g., the overview of recent data in Ref. [STV08]), leaving room for different theoretical models. Its existence is, nevertheless, widely accepted since it offers the most simple way for explaining the observed oscillations of neutrino flavor eigenstates. Still, the formally correct description of these oscillations is a controversial issue to this day, as discussed in Ref. [AK10]. Here, we shall restrict ourselves to a brief example (cf. Sec. 5.1.1 of Ref. [MP04]) of how mixing between the electron and the muon neutrino can be detected, when initially only a muon neutrino has been produced.

We describe the mixture of mass eigenstates, $\nu_i, i \in \{1, 2\}$, associated with a flavor eigenstate, $\nu_f, f \in \{e, \mu\}$, by a rotation through an angle ϕ, i.e.,

$$\begin{pmatrix} \nu_e \\ \nu_\mu \end{pmatrix} = U \begin{pmatrix} \nu_1 \\ \nu_2 \end{pmatrix} = \begin{pmatrix} \cos\phi & \sin\phi \\ -\sin\phi & \cos\phi \end{pmatrix} \begin{pmatrix} \nu_1 \\ \nu_2 \end{pmatrix}. \tag{2.14}$$

Thus, the muon-flavor state created at the beginning of the experiment is given by

$$|\nu_\mu\rangle = -\sin\phi|\nu_1\rangle + \cos\phi|\nu_2\rangle. \tag{2.15}$$

Since the wave functions of the free massive neutrinos satisfy the Dirac equation, it is natural to assume propagation by means of plane waves,

$$|\nu_i(t, x)\rangle = \exp\left[-\mathrm{i}(E_\nu t - \mathbf{px})\right] |\nu_i(0, 0)\rangle. \tag{2.16}$$

One can simplify the exponent by assuming light speed for the neutrinos and passing to the ultra-relativistic limit

$$E_\nu = \sqrt{m_\nu^2 + \mathbf{p}^2} \approx |\mathbf{p}| + \frac{m_\nu^2}{2|\mathbf{p}|} \equiv E + \frac{m_\nu^2}{2E}, \tag{2.17}$$

where the notation $E \equiv |\mathbf{p}|$ has been introduced since the difference between E and E_ν becomes visible in the oscillation pattern but not in the experimental estimation of the beam-energy, E. The wave function of the propagated muon-flavor eigenstate in a distance L from the point of creation and after flight time L then reads

$$|\nu_\mu(L,L)\rangle = \sum_{i=1,2} \exp\left(-\mathrm{i}\frac{m_i^2 L}{2E}\right)|\nu_i(0,0)\rangle = \sum_{i=1,2} \exp\left(-\mathrm{i}\frac{m_i^2 L}{2E}\right) U_{2i}|\nu_i\rangle. \tag{2.18}$$

On the other hand, the electron neutrino flavor eigenstate is given by

$$|\nu_e\rangle = \sum_{j=1,2} U_{1j}|\nu_j\rangle \tag{2.19}$$

with orthogonal mass eigenstates, ν_j. Consequently the probability of finding a neutrino of electron flavor in L is given by the transition matrix element,

$$P_{\nu_\mu\to\nu_e}(L) = \left|\langle\nu_e^f|\nu_\mu^f(L,L)\rangle\right|^2 = \left|\sum_{i=1,2} U_{1i}^* U_{2i} \exp\left(-\mathrm{i}\frac{m_i^2 L}{2E}\right)\right|^2 = \sin^2(2\phi)\sin^2\left(\frac{\Delta m^2 L}{4E}\right), \tag{2.20}$$

where $\Delta m^2 = |m_{\nu_1}^2 - m_{\nu_2}^2|$ denotes the squared-mass difference. Fig. 2.2 shows this transition probability as a function of L. From the above equation one also sees that such experiments are only sensitive to relative mass differences, but not to absolute mass scales.

2.2 General properties of the lepton-nucleon interaction

As many of the nucleon's properties are not yet well-understood in the fundamental quark-picture, hadronic models, like ours, treat the nucleon as an elementary fermion. The rich variety of responses of the nucleon in leptonic scattering reactions has been grouped into different reaction channels, that have then been parametrized. Whereas an overview of the most prominent reaction channels is given in this section, some details concerning the parameterizations are exposed within the following sections. For a discussion of other effects we refer the reader to the dissertations of T. Leitner [Lei09] and O. Buss [Bus08].

2.2.1 Reaction channels of the nucleon

The elementary interactions of leptons and nucleons can be treated in a similar formalism as those of leptons and quarks, described in Sec. 2.1.3. Again, we consider reactions that are triggered by the exchange of *one* gauge boson. The resulting variety of final states of the nucleon can be classified into different reaction channels:

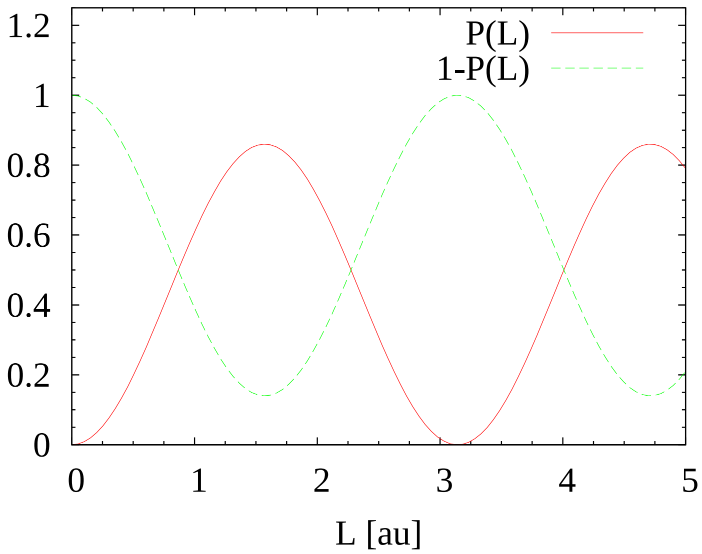

Figure 2.2: Appearance probability P of an electron neutrino after creation of a muon neutrino at origin as a function of the distance L (solid curve) and probability for finding no appearance $1-P$ (dashed curve). For the amplitude of the oscillation, $\sin^2(2\phi_{12})$, an experimentally motivated value of 0.84 was chosen. The wavelength of the oscillation, $2\pi c \cdot 4E/\Delta m^2$, is sensible to both the mass-squared difference, Δm^2_{12} (chosen to be $7.65 \cdot 10^{-5}$ eV), and the (reconstructed) neutrino energy, E.

- The nucleon can pick up the transferred four-momentum as a whole (cf. Fig. 2.3a). Depending on whether this occurs in an electromagnetic or a charged-current driven process, one calls this scenario *elastic* or *quasielastic scattering*. By writing QE we will refer to either both processes or the one that suits the reaction being discussed.

- A different possibility is the pickup of energy by the nucleon's inner degrees of freedom, constituent-quark spin and flavor. This leads to the *production of a hadronic resonance* (RES), which, after a certain life-time, τ, will decay back into a nucleon by emitting mesons or real photons[3]. An example is depicted in Fig. 2.3b.

- The same final state, πN, can also be reached by pion creation without an intermediate resonance (cf. Fig. 2.3c), e.g., by direct interaction with the quark-gluon field inside the nucleon. Usually this reaction channel is referred to as *non-resonant background* (BG).

- The total momentum transfer can be picked up by just one quark, which then exits the nucleon creating a shower of hadronic byproducts due to the principle of confinement (cf. Fig. 2.3d)). This process of *deep inelastic scattering* (DIS), of considerable impact at large energy transfers, allows for a variety of hadronic final states.

[3]This holds true for the vacuum case, while for the in-medium case, treated in the next chapter, the produced resonances can rescatter inside the nucleus and form other final states.

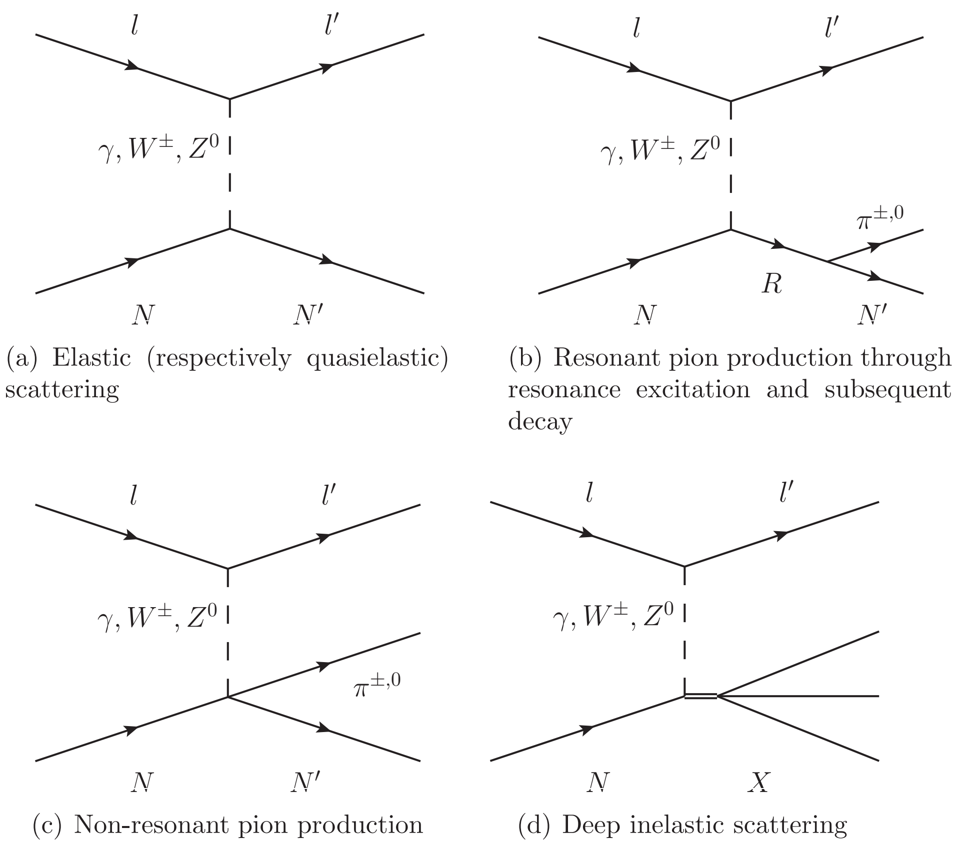

(a) Elastic (respectively quasielastic) scattering

(b) Resonant pion production through resonance excitation and subsequent decay

(c) Non-resonant pion production

(d) Deep inelastic scattering

Figure 2.3: Different reaction channels in lepton-nucleon scattering.

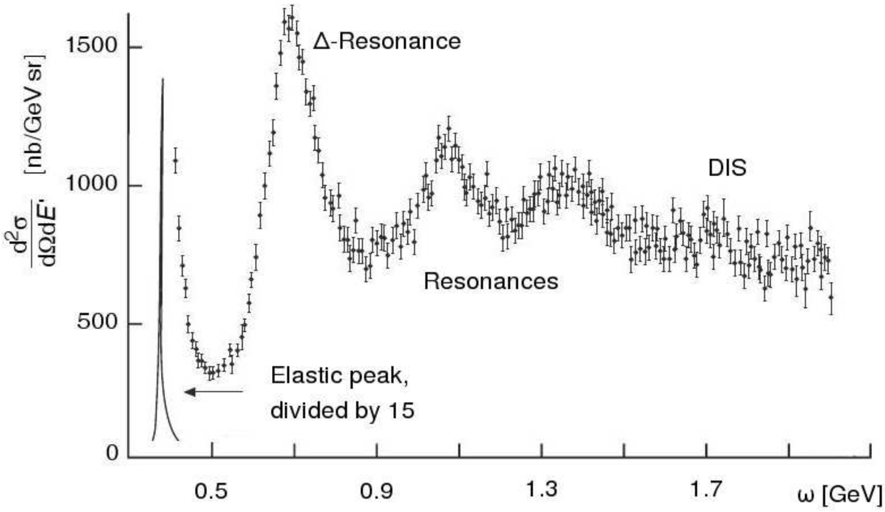

Figure 2.4: An example of the nucleon response in an e-p-scattering experiment. Shown is the double-differential inclusive cross section vs. the energy transfer, ω, with data taken from Ref. [BDK+68]. Energy regions are labeled according to relevant reaction channels.

2.2.2 Magnitudes of the contributions

As one can see for inclusive electron-nucleon scattering in Fig. 2.4, QE scattering is by far the most dominant contribution, being energetically separated from the second pronounced peak, associated with production of the Δ resonance. Other resonance excitations and the DIS part, governing the energy regimes above the Δ peak, cannot be disentangled that easily.

Since in our further analysis invariant masses above 2 GeV will not be considered, contributions from deep inelastic scattering play no role. Nevertheless, we wish to stress the deep connection between Bjorken's x-scaling description of the DIS response, derived in Ref. [BP69] from the idea of one nucleon constituent taking up the entire energy transfer, and the concept of superscaling, that will be explained in Sec. 4.4.

The role of the non-resonant background cannot be estimated from Fig. 2.4, and one has to resort to model calculations and comparisons with predicted pion-production cross sections, as done in [DY57], to motivate its introduction. In Sec. 2.5 we will follow the approach from Ref. [BDW67], where introducing a phenomenological Lagrangian has led to a parameterization of the hadronic vertex function.

Satisfactory accordance between the sum of the three contributions described so far and the data leads us to neglect other conceivable contributions (e.g., 2π non-resonant background) as well as interference between these effects. Consequently, we write the cross section as

$$\mathrm{d}\sigma = \mathrm{d}\sigma_{\mathrm{QE}} + \sum_{\mathrm{Resonances}} \mathrm{d}\sigma_R + \mathrm{d}\sigma_{\mathrm{BG}}. \tag{2.21}$$

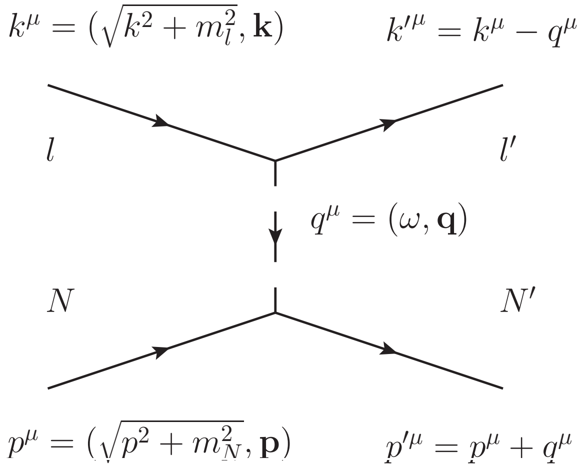

Figure 2.5: Kinematics of QE processes

2.2.3 Kinematics of the lepton-nucleon interaction

In Fig. 2.5, we show a more detailed description of the QE scattering process,

$$l(k) + N(p) \to l(k') + N(p'), \tag{2.22}$$

already depicted in Fig. 2.3a. Throughout this work, we let the incoming lepton define the z-axis. The direction of the outgoing lepton is then given by

$$\mathbf{k}' = (|\mathbf{k}'| \sin\theta \cos\phi, |\mathbf{k}'| \sin\theta \sin\phi, |\mathbf{k}'| \cos\theta). \tag{2.23}$$

Please note that for the rest of this work we will assume one-boson exchange approximation and, due to reasons that will become evident in Sec. 4.4, we stick to the following unusual nomenclature for the virtual photon's four-momentum,

$$\begin{aligned} q^\mu &= p'^\mu - p^\mu = k^\mu - k'^\mu = (\omega, \mathbf{q}) \\ q &= |\mathbf{q}|, \end{aligned}$$

which consists of energy loss, ω, and three-momentum transfer, $\mathbf{q}$. Only if q^μ is given with a Greek index, the four-momentum transfer is to be understood, in other cases q stands for the absolute value of the three-momentum transfer. Consequently, $q^2 = q^i q^i$ is not to be mistaken for $q_\mu q^\mu = -Q^2$, which is also an important quantity and can be expressed as[4].

$$\begin{aligned} Q^2 &= -q_\mu q^\mu \\ &= -k'^2 - k^2 + 2kk' \\ &= -m_l^2 - m_{l'}^2 + 2k^0 k'^0 - 2|\mathbf{k}||\mathbf{k}'| \cos\theta \\ &\underbrace{\approx}_{m_{l,l'}^2 \approx 0} 2k^0 k'^0 (1 - \cos\theta). \end{aligned}$$

[4]Note that the last approximation does not hold for CC ν_μ scattering. A modification will be presented in Sec. 4.6.

Since experiments often work by varying the beam energy and detector angle, throughout this work we are mostly interested in the double-differential cross section $\mathrm{d}\sigma/\mathrm{d}\omega\mathrm{d}\Omega$, with $\mathrm{d}\Omega = \mathrm{d}\phi\ \mathrm{d}\cos\theta$ being the solid-angle element. For the derivation of these cross section formulae we refer the reader to Appendix B of Ref. [Lei09]. Here, we only present the results.

We begin by stating the general expression for the scattering cross section in the case of two incoming particles ($i = 1, 2$) and N outgoing particles ($f = 1, \ldots, N$),

$$\mathrm{d}\sigma = \frac{(2\pi)^4}{4\left[(p_1 \cdot p_2)^2 - m_1^2 m_2^2\right]^{1/2}} \delta\left(\sum_f p_f - \sum_i p_i\right)\left(\prod_f \frac{\mathrm{d}^4 p_f}{(2\pi)^3}\delta(p_f^2 - m_f^2)\right)\overline{|\mathcal{M}|^2}. \tag{2.24}$$

The product of δ functions can be simplified for particles on their mass shell, using

$$\frac{\mathrm{d}^4 p}{(2\pi)^3}\delta(p^2 - m^2) = \frac{\mathrm{d}^3\mathbf{p}}{(2\pi)^3 2p^0} = \frac{1}{(2\pi)^3}\frac{\sqrt{p^{0^2} - m^2}}{2}\mathrm{d}\Omega\mathrm{d}p^0. \tag{2.25}$$

By restriction to lepton-nucleon states, one is led to the QE scattering cross section,

$$\frac{\mathrm{d}\sigma_{\mathrm{QE}}}{\mathrm{d}\omega\mathrm{d}\Omega_{k'}} = \frac{|\mathbf{k}'|}{32\pi^2}\frac{\delta(p'^2 - M_N^2)}{\left[(k \cdot p)^2 - m_l^2 M_N^2\right]^{1/2}}\overline{|\mathcal{M}_{\mathrm{QE}}|^2}. \tag{2.26}$$

For resonance excitations,

$$l(k) + N(p) \to l(k') + R(p') \tag{2.27}$$

the above expression is modified by including the spectral function $\mathcal{A}(p)$, resulting in

$$\frac{\mathrm{d}\sigma_R}{\mathrm{d}\omega\mathrm{d}\Omega_{k'}} = \frac{|\mathbf{k}'|}{32\pi^2}\frac{\mathcal{A}(p')}{\left[(k \cdot p)^2 - m_l^2 M_N^2\right]^{1/2}}\overline{|\mathcal{M}_R|^2}. \tag{2.28}$$

The role of the spectral function will be discussed in more detail in Sec. 2.4 and Sec. 5.1.4. An important quantity is the invariant mass of a resonance,

$$W = \sqrt{p'^2}. \tag{2.29}$$

Throughout this work, we restrict ourselves to processes with $W < 2$ GeV.

Finally, the vector part of the pion-production cross section reads

$$\frac{\mathrm{d}\sigma^{\mathrm{V}}_{N\pi}}{\mathrm{d}\omega\mathrm{d}\Omega_{k'}\mathrm{d}\Omega_{k_\pi}} = \int \mathrm{d}k_\pi^0 \frac{|\mathbf{k}'||\mathbf{k}_\pi|}{512\pi^5}\left[(k \cdot p)^2 - m_l^2 M_N^2\right]^{-1/2}\delta(p^2 - M_N^2)\overline{|\mathcal{M}_{N\pi}|^2}. \tag{2.30}$$

This expression contains contributions from both, resonant and non-resonant processes. An approach to disentanglement of these two quantities and an estimation of the axial contribution will be presented in Sec. 2.5.

boson	coupling strength (G)	Feynman propagator ($\mathrm{i}S^{\mathrm{F}}_{\mu\nu}$)
γ	$\sqrt{4\pi\alpha}$	$\frac{-\mathrm{i}g_{\mu\nu}}{q_\eta q^\eta}$
$W^\pm$	$\frac{g}{2\sqrt{2}}$	$\frac{\mathrm{i}}{q_\eta q^\eta - M_W^2}\left(-g_{\mu\nu} + \frac{q_\mu q_\nu}{M_W^2}\right) \xrightarrow{\vert q_\eta q^\eta\vert \ll M_W^2} \frac{\mathrm{i}g_{\mu\nu}}{M_W^2}$
Z^0	$\frac{g}{2\cos\theta_W}$	$\ldots \to \frac{\mathrm{i}g_{\mu\nu}}{M_Z^2}$

Table 2.1: Overview of boson couplings and propagators, to be used in Eq. (2.31). Here, $g = e/\sin\theta_W$ denotes the electroweak coupling constant. Following [A+08], we take $M_W = 80.425$ GeV and $M_Z = 91.188$ GeV as the boson masses.

2.2.4 Dynamics of the lepton-nucleon interaction

In Sec. 2.1.1 and Eq. (2.24), we already pointed out that the cross section factorizes into kinematical parts and the invariant matrix element, $\mathcal{M}$, which contains all the underlying dynamics of the reaction. For one-boson-exchange diagrams, as the ones in Fig. 2.3, application of the Feynman rules yields a compact relation for the matrix element,

$$-\mathrm{i}\mathcal{M} = (\mathrm{i}Gj^\mu)\,\mathrm{i}S^{\mathrm{F}}_{\mu\nu}\,(\mathrm{i}GJ^\nu)\,, \tag{2.31}$$

where the coupling strength, G, and the boson propagator, $\mathrm{i}S^{\mathrm{F}}_{\mu\nu}$, depend on the exchange boson. The dependencies are listed in Table 2.1. Taking only the leptonic parts of the electroweak currents, already discussed in Sec. 2.1.3, we can introduce the leptonic current as $j^\mu = \bar{l}(k')\gamma^\mu(1 - a\gamma^5)l(k)$, where $a = 0$ for electromagnetic and $a = 1(-1)$ for weak (anti-)lepton processes.

The hadronic current, J^ν, cannot be calculated from first principles and needs to be parametrized using form factors. It lies thus at the heart of hadronic model building and depends very specifically on the interaction and the reaction channel.

To make the connection to a polarization-insensitive experiment via Eq. (2.2), one needs to take first the square of the matrix element and then sum and average over multiple final and the two initial spin states, s_A and s_B, respectively. This leads to the replacement

$$|\mathcal{M}|^2 \to \overline{|\mathcal{M}|^2} \equiv \frac{1}{(2s_A+1)(2s_B+1)} \sum_{\text{all spins}} |\mathcal{M}|^2. \tag{2.32}$$

Keeping the $g_{\mu\nu}$ structure of the propagators in mind, we can perform the contraction and introduce the scalar propagator, $\mathrm{i}S_{\mathrm{F}}$, obtaining the compact relation

$$\overline{|\mathcal{M}|^2} = \sum_{s_i}\sum_{s_f} \left[(\mathrm{i}Gj_\mu)\,\mathrm{i}S_{\mathrm{F}}\,(\mathrm{i}GJ^\mu)\right]^\dagger (\mathrm{i}Gj_\nu)\,\mathrm{i}S_{\mathrm{F}}\,(\mathrm{i}GJ^\nu)^\dagger = C^2 L_{\mu\nu} H^{\mu\nu}. \tag{2.33}$$

In the last step we have rearranged and summarized the terms, introducing the leptonic tensor,

$$L_{\mu\nu} = \frac{1+|a|}{2}\sum_{s_f}\sum_{s_i} {j_\mu}^\dagger j_\nu, \tag{2.34}$$

the hadronic tensor,

$$H^{\mu\nu} = \frac{1}{2}\sum_{s_f}\sum_{s_i} J^{\mu\dagger} J^\nu, \tag{2.35}$$

and the coupling of the interaction, C. The coupling is obtained by combining boson propagator, $\mathrm{i}S_\mathrm{F}$, and the square of the vertex factor, thus reading $C_\mathrm{EM} = 4\pi\alpha/q_\mu q^\mu$ for photons, $C_\mathrm{CC} = \cos\theta_\mathrm{C} G_\mathrm{F}/\sqrt{2}$ for $W^\pm$-bosons and $C_\mathrm{NC} = G_\mathrm{F}/\sqrt{2}$ for Z-bosons[5]. The tensors can be reformulated as traces, yielding, e.g.,

$$L^e_{\mu\nu} = \frac{1}{2}\,\mathrm{Tr}\left[(\not{k}' + m_e)\gamma_\mu(\not{k} + m_e)\gamma_\nu\right] \tag{2.36}$$

for the electron tensor, and further evaluated by means of trace techniques, as described in Ref. [HM08].

2.3 Elastic and quasielastic scattering

In this section, we reconsider ways for describing the single-nucleon QE response, which will be of major importance throughout the rest of this work, not only because it is dominant at energies of a few GeV, as we have seen in Fig. 2.4, but also because it plays a key role in the development of superscaling techniques. Even though the formalism described here is fully capable of treating NC reactions, these reactions are of no relevance to our analysis and, omitting them from further discussion, we refer the interested reader to Ref. [Lei09].

2.3.1 Hadronic current

In Sec. 2.2.4, we already stressed that the hadronic current J^μ lies at the heart of model building, with the hadronic tensor being constructed from it as

$$H^{\mu\nu} = \frac{1}{2}\sum_{s_f}\sum_{s_i} J^{\mu\dagger} J^\nu. \tag{2.37}$$

Separating out the nucleon spinors, $u(p)$, one can express the hadronic current by use of a vertex function, Γ^μ, as

$$J^\mu = \bar{u}(p')\Gamma^\mu u(p). \tag{2.38}$$

For elastic scattering of a spin 1/2 particle, one would suggest the electroweak "V - A"-structure to persist and thus can make the following ansatz

$$\Gamma^\mu_\mathrm{QE} = \mathcal{V}^\mu_\mathrm{QE} - \mathcal{A}^\mu_\mathrm{QE}. \tag{2.39}$$

A standard approach for the vector vertex function, $\mathcal{V}^\mu_\mathrm{QE}$, is to express it in full generality as a linear combination of Lorentz invariant vector entities γ^μ, p^μ and p'^μ. Following Sec. 6.2 of Ref. [PS95], one can express this as

$$\mathcal{V}^\mu_\mathrm{QE} = A\cdot\gamma^\mu + B\cdot(p'^\mu + p^\mu) + C\cdot(p'^\mu - p^\mu), \tag{2.40}$$

where A, B, C are real-valued functions of the only nontrivial Lorentz scalar $q_\mu q^\mu$. By applying current conservation $q_\mu\mathcal{V}^\mu_\mathrm{QE} = 0$, one is able to show $C = 0$. Using the Gordon

[5]Note that $G_\mathrm{F}/\sqrt{2} = g^2/(8M_W^2)$

identity to replace $p'^{\mu} + p^{\mu}$ by the Lorentz tensor $\sigma^{\mu\nu} = \frac{\mathrm{i}}{2}(\gamma^{\mu}\gamma^{\nu} - \gamma^{\nu}\gamma^{\mu})$, one is led to the following expression for the vertex function

$$\mathcal{V}^{\mu}_{\mathrm{QE}} = \mathcal{F}_1\gamma^{\mu} + \mathcal{F}_2\frac{\mathrm{i}\sigma^{\mu\nu}q_{\nu}}{2M_N}. \tag{2.41}$$

In a similar manner, one writes the axial part as a combination of an axial-vector form factor, F_{A}, and a pseudoscalar one, F_{P}, reading

$$-\mathcal{A}^{\mu}_{\mathrm{QE}} = F_{\mathrm{A}}\gamma^{\mu}\gamma^5 + \frac{F_{\mathrm{P}}}{M_N}q^{\mu}\gamma^5. \tag{2.42}$$

2.3.2 Form factors of the nucleon

Vector form factors

The coefficients $\mathcal{F}_1, \mathcal{F}_2$ are placeholders for the interaction- and reaction-channel-dependent form factors, with the nomenclature summarized in Table 2.2. The original motivation for the study of form factors came from analysis of $ep \to ep$ scattering, where by means of Rosenbluth separation one can assess the electric and magnetic Sachs form factors, $G^{p,n}_{\mathrm{E}}$ and $G^{p,n}_{\mathrm{M}}$, as will be further explained in Sec. 6.2. The Sachs form factors are directly related[6] to the electromagnetic form factors of the nucleon via

$$F^{p,n}_1 = \left[G^{p,n}_{\mathrm{E}} + \frac{Q^2}{4M_N^2}G^{p,n}_{\mathrm{M}}\right]\left[1 + \frac{Q^2}{4M_N^2}\right]^{-1} \tag{2.43}$$

and

$$F^{p,n}_2 = \left[G^{p,n}_{\mathrm{E}} - G^{p,n}_{\mathrm{M}}\right]\left[1 + \frac{Q^2}{4M_N^2}\right]^{-1}. \tag{2.44}$$

As a first approximation, the dipole ansatz,

$$G^{p,n}_i(Q^2) = G^{p,n}_i(0)\left(\frac{1}{1+\frac{Q^2}{M_*^2}}\right)^2, \tag{2.45}$$

with $G^{p,n}_i(0)$ and M_* fitted to experimental data, works fairly well. In our model, the updated BBBA2007 parameterization [BABB08], which includes more sophisticated dependencies, is used.

Axial form factors

For parameterization of CC scattering, an established technique is to assume pion-pole dominance, as proposed in Ref. [GML60], and partial conservation of the axial current (PCAC) to find the following connection between F_{A} and F_{P}

$$F_{\mathrm{P}}(Q^2) = \frac{2M_N^2}{Q^2 + m_{\pi}^2}F_{\mathrm{A}}(Q^2). \tag{2.46}$$

[6] Cf., e.g., Eqs. (4.39)-(4.52) in Ref. [Bus08].

interaction	reaction	form factor
EM	$l^- p \to l^- p$	F_i^p
EM	$l^- n \to l^- n$	F_i^n
CC	$\nu n \to l^- p$	$F_i^V = F_i^p - F_i^n$

Table 2.2: Nomenclature for the vector form factors in QE scattering. The placeholders $\mathcal{F}_i$ in Eq. (2.41) are to be substituted with the reaction-specific form factors in the right column. A derivation of the last relation can be found in Appendix D.1 of Ref. [Lei09].

For the Q^2-dependence of the form factor in our model we use the dipole ansatz,

$$F_\mathrm{A}(Q^2) = F_\mathrm{A}(0)\left(\frac{1}{1+\frac{Q^2}{M_\mathrm{A}^2}}\right)^2, \tag{2.47}$$

where the coupling $F_\mathrm{A}(0)$ needs to be taken from neutron beta decay experiments [BEM02][7]. In our model the value $g_\mathrm{A} = 1.267$, as obtained from neutron beta decay and listed by the particle data group [A$^+$08] is used.

For the value of the axial mass, $M_A = 0.999$ GeV is assumed, following the approach of Kuzmin [KLN08] *et al.*, who refitted QE neutrino scattering data relying on the BBBA2007 parameterization. This should guarantee consistency since we also use BBBA2007 vector form factors, as pointed out above. Nevertheless, it should be noted that the value of the axial mass is a controversial issue, since recent data from neutrino-scattering experiments at K2K [K2K] and MiniBooNE [G$^+$06, AA$^+$08] seem to imply axial masses of 1.2 GeV and more. This issue will be taken up again in Sec. 6.4.

2.4 Excitation of baryon resonances

In this section, the influence of resonance excitation on the inclusive cross section will be discussed. Focusing on the region of a few GeV incoming energy, we will be mostly interested in the Δ excitation. Since, depending on the spin of the resonance, the hadronic currents involve different spinors, we will present the formalism for spin $1/2$ and spin $\geq 3/2$ resonances separately. We will begin with an overview of the resonances considered in this work.

[7] Aiming at axial couplings for the resonances, where a direct measurement is not possible, we note that one can also obtain the value of $F_\mathrm{A}(0)$ to five percent precision using the Goldberger-Treiman relation (cf. Sec. 19.3 of [PS95]),

$$g_A = 2 f_\pi \frac{f}{m_\pi}. \tag{2.48}$$

With this equation, one can relate the axial coupling, $g_\mathrm{A} = -F_A(0)$, to the experimentally assessable pion-decay constant, f_π=93 MeV, and the πNN coupling constant, $f/m_\pi = 7.15$ GeV^{-1}. The entire formalism, leading to above equations, is described in Chapter 9 of Ref. [EWE88].

name	mass [GeV]	width [GeV]	spin	isospin	parity
$N, P_{11}(938)$	0.938	0.000	0.5	0.5	+
$\Delta, P_{33}(1232)$	1.232	0.118	1.5	1.5	+
$P_{11}(1440)$	1.462	0.391	0.5	0.5	+
$D_{13}(1520)$	1.524	0.124	1.5	0.5	-
$S_{11}(1535)$	1.534	0.151	0.5	0.5	-
$S_{31}(1620)$	1.672	0.154	0.5	1.5	-
$S_{11}(1650)$	1.659	0.173	0.5	0.5	-
$D_{15}(1675)$	1.676	0.159	2.5	0.5	-
$F_{15}(1680)$	1.684	0.139	2.5	0.5	+
$D_{33}(1700)$	1.762	0.599	1.5	1.5	-
$P_{13}(1720)$	1.717	0.383	1.5	0.5	+
$F_{35}(1905)$	1.881	0.327	2.5	1.5	+
$P_{31}(1910)$	1.882	0.239	0.5	1.5	+
$F_{37}(1950)$	1.945	0.300	3.5	1.5	+

Table 2.3: List of baryons and their properties. We restrict our analysis to these 14 states. The experimental values are taken from the analysis of Manley *et. al.* [MS92].

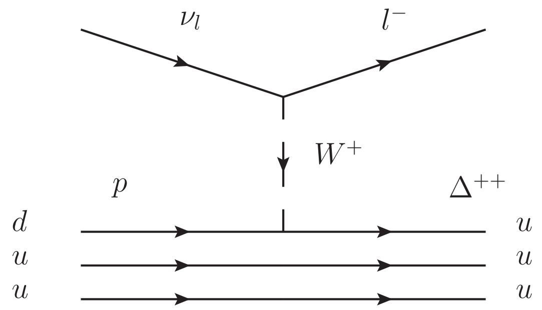

Figure 2.6: Feynman diagram of Δ^{++} production in neutrino scattering.

2.4.1 Resonances with invariant masses smaller than 2 GeV

There is a large number of nucleon excitations known in particle physics (cf. Ref. [A$^+$08]). Most of them have a mass higher than 2 GeV and shall thus not be considered in this work. For our model, we focus on 13 resonances below this threshold, that are included in the MAID2005 analysis [MAI]. They will serve as our starting point for modelling form factors; their properties are listed in Table 2.3.

Generally speaking, resonances consist of excited states of the nucleon, where the struck constituent quarks change their flavor or their spin configuration. As a simple example, the CC excitation of the Δ^{++} is depicted in Fig. 2.6. Within this work we do not take into account resonances containing strangeness, charmness, topness or bottomness, since their production at the primary interaction vertex is Cabibbo suppressed.

In Table 2.3, we make use of standard hadron spectroscopy notation L_{IJ}, where J (I) denotes the spin (isospin) quantum number, and $L = |\mathbf{l} + \mathbf{l}'|$ stands for the sum of the

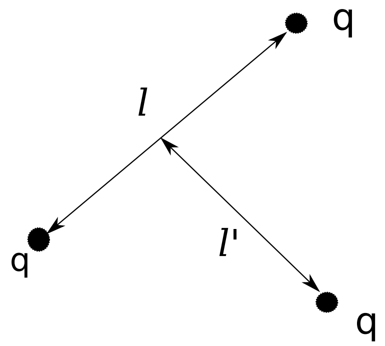

Figure 2.7: Interpretation of the quarks' relative angular momenta adding up to the angular momentum, $\mathbf{L}$, of the nucleon.

quark angular momenta, $\mathbf{l}$ and $\mathbf{l}'$, as depicted in Fig. 2.7. The total angular momentum, $\mathbf{J}$, can be written as a sum of the particles' relative angular momenta and their spin,

$$\mathbf{J} = \mathbf{L} + \mathbf{S}. \tag{2.49}$$

2.4.2 Excitation of spin 1/2 resonances

The treatment of spin 1/2 resonances shows many similarities to the analysis of QE scattering and hence offers a good starting point. In our model, we include the $P_{11}(1440)$, $S_{11}(1535)$, $S_{11}(1650)$ resonances with isospin $I = 1/2$ and the $S_{31}(1620), P_{31}(1910)$ resonances with $I = 3/2$.

Hadronic current

In analogy to Sec. 2.3, we begin by expressing the hadronic current,

$$J^\mu = \bar{N}(p')\Gamma^\mu N(p), \tag{2.50}$$

through the vertex function, Γ^μ. For states with positive parity (e.g., $P_{11}(1440)$), we start with the following ansatz, known from elastic scattering,

$$\Gamma^\mu_{1/2,-} = \mathcal{V}^\mu_{1/2} - \mathcal{A}^\mu_{1/2} \tag{2.51}$$

For states with negative parity (e.g., $S_{11}(1535)$), an additional γ^5 has to be taken into account, yielding

$$\Gamma^\mu_{1/2,+} = \left[\mathcal{V}^\mu_{1/2} - \mathcal{A}^\mu_{1/2}\right]\gamma^5. \tag{2.52}$$

The vector and the axial part are parametrized as

$$\mathcal{V}^\mu_{\mathrm{QE}} = \frac{\mathcal{F}_1}{(2M_N)^2}(Q^2\gamma^\mu + \not{q}q^\mu) + \mathcal{F}_2\frac{\mathrm{i}\sigma^{\mu\nu}q_\nu}{2M_N}, \tag{2.53}$$

$$-\mathcal{A}^\mu_{\mathrm{QE}} = \mathcal{F}_\mathrm{A}\gamma^\mu\gamma^5 + \frac{\mathcal{F}_\mathrm{P}}{M_N}q^\mu\gamma^5, \tag{2.54}$$

involving the use of interaction and reaction-channel-specific form factors.

interaction	reaction	$\mathcal{F}(I=1/2)$	$\mathcal{F}(I=3/2)$
EM	$l^- p \to l^- p$	F_i^p	F_i^N
EM	$l^- n \to l^- n$	F_i^n	F_i^N
CC	$\nu n \to l^- R^{++}$	-	$\sqrt{3} F_i^{\mathrm{V}} = -\sqrt{3} F_i^N$
CC	$\nu n \to l^- R^{+}$	$F_i^{\mathrm{V}} = F_i^p - F_i^n$	$F_i^{\mathrm{V}} = -F_i^N$

Table 2.4: Nomenclature for the vector form factors of spin-1/2-resonance excitations. The placeholders $\mathcal{F}_i$ in Eq. (2.53) are to be substituted with the reaction-specific form factors in the two columns on the right, depending on isospin I.

Vector form factors

Keeping the overlapping peaks in the resonance region of Fig. 2.4 in mind, fitting the form factors to direct cross-section measurements is a forbidding task. Nevertheless, it is well-known [DEK76] that by means of helicity amplitudes an extraction of form factors is possible.

Helicity amplitudes describe the nucleon-resonance-transition probability dependent on the specific polarization of the incoming virtual photon and the spin orientation of nucleon and resonance. In practice, they can be assessed by applying a partial wave analysis to experimental data on photon and electron scattering. Throughout this work, we will use the world-data analysis performed by the MAID group [DT92, DHKT99, MAI]. The expressions relating helicity amplitudes and form factors can be found, e.g. in Sec. 4.5 of Ref. [Bus08]. In Table 2.4, we present the nomenclature taken from Sec. 5.1 of Ref. [Lei09].

Axial form factors

Both, theoretical and experimental information on the axial form factors, are not conclusive [BCBH07]. Following the ideas developed in the previous section, one can apply PCAC and pion-pole dominance to relate F_{A} and F_{P} by

$$F_{\mathrm{P}}(Q^2) = \frac{(M_R \pm M_N) M_N}{Q^2 + m_\pi^2} F_{\mathrm{A}}(Q^2), \tag{2.55}$$

with $+$ $(-)$ for positive (negative) parity resonances. Again, one can use the simple dipole ansatz,

$$F_{\mathrm{A}}(Q^2) = F_{\mathrm{A}}(0) \left(1 + \frac{Q^2}{M_{\mathrm{A}}^{*\,2}}\right)^{-2}. \tag{2.56}$$

In our model, the value $M_{\mathrm{A}}^* = 1$ GeV, known from QE scattering, is assumed for the axial mass. Using off-diagonal Goldberger-Treiman relations [FN79], one can relate the axial coupling to the πNN coupling, f/m_π, by

$$F_{\mathrm{A}}(0) = -C_{\mathrm{iso}} \sqrt{2} f_\pi \frac{f}{m_\pi}, \tag{2.57}$$

with the isospin factors $C_{\mathrm{iso}}(I=1/2) = \sqrt{2}$, $C_{\mathrm{iso}}(I=3/2) = -1/\sqrt{3}$ derived in Appendix A.4 of Ref. [Lei09]. The nomenclature, also taken from Ref. [Lei09], is summarized in Table 2.5.

interaction	reaction	$\mathcal{F}_{\mathrm{A}}(I=1/2)$	$\mathcal{F}_{\mathrm{A}}(I=3/2)$
CC	$\nu n \to l^- R^{++}$	-	$\sqrt{3}\,F_{\mathrm{A}}$
CC	$\nu n \to l^- R^{+}$	F_{A}	F_{A}

Table 2.5: Nomenclature for the axial form factors of spin-1/2-resonance excitations. The placeholder $\mathcal{F}_{\mathrm{A}}$ in Eq. (2.54) is to be substituted with the reaction-specific form factors in the two columns on the right, depending on isospin I. Eq. (2.55) can be used to obtain the corresponding $\mathcal{F}_{\mathrm{P}}$.

2.4.3 Excitation of spin 3/2 resonances

Besides the Δ resonance, $P_{33}(1232)$, we include the $P_{13}(1720)$, $D_{13}(1520)$ and the $D_{33}(1700)$ spin 3/2 resonances.

Hadronic current

The spinors of massive spin 3/2 fermions are described by means of the Rarita-Schwinger formalism, as explained in Ref. [Gre00]. Let $\psi^R_\alpha(p')$ denote the spinor of the outgoing resonance, then the hadronic current is given by

$$J^\mu_{3/2} = \bar{\psi}^R_\alpha(p')\Gamma^{\alpha\mu}_{3/2}u(p). \tag{2.58}$$

Again, different vertex functions apply, depending on parity. For negative parity one writes,

$$\Gamma^{\alpha\mu}_{3/2,-} = \mathcal{V}^{\alpha\mu}_{3/2} - \mathcal{A}^{\alpha\mu}_{3/2}, \tag{2.59}$$

while positive parities demand an additional γ^5, yielding

$$\Gamma^{\alpha\mu}_{3/2,+} = \left[\mathcal{V}^{\alpha\mu}_{3/2} - \mathcal{A}^{\alpha\mu}_{3/2}\right]\gamma^5. \tag{2.60}$$

Due to the different spinor structure, the parameterization involves more terms, and the vector part reads

$$\mathcal{V}^{\alpha\mu}_{3/2} = \frac{\mathcal{C}^{\mathrm{V}}_3}{M_N}(g^{\alpha\mu}\not{q} - q^\alpha\gamma^\mu) + \frac{\mathcal{C}^{\mathrm{V}}_4}{M_N^2}(g^{\alpha\mu}q_\eta p'^\eta - q^\alpha p'^\mu) + \frac{\mathcal{C}^{\mathrm{V}}_5}{M_N^2}(g^{\alpha\mu}q_\eta p^\eta - q^\alpha p^\mu) + C^{\mathrm{V}}_6 g^{\alpha\mu}. \tag{2.61}$$

For the axial part one finds

$$-\mathcal{A}^{\alpha\mu}_{3/2} = \left[\frac{\mathcal{C}^{\mathrm{A}}_3}{M_N}(g^{\alpha\mu}\not{q} - q^\alpha\gamma^\mu) + \frac{\mathcal{C}^{\mathrm{A}}_4}{M_N^2}(g^{\alpha\mu}q_\eta p'^\eta - q^\alpha p'^\mu) + C^{\mathrm{A}}_5 g^{\alpha\mu} + \frac{\mathcal{C}^{\mathrm{A}}_6}{M_N^2}q^\alpha p^\mu\right]\gamma^5. \tag{2.62}$$

Vector form factors

To obtain the vector form factors, our model relies on the extraction from helicity amplitudes provided by MAID2005 [DT92, DHKT99, MAI]. We list the nomenclature, taken from Ref. [Lei09] in Table 2.6.

interaction	reaction	$C^{\mathrm{V}}(I=1/2)$	$C^{\mathrm{V}}(I=3/2)$
EM	$l^- p \to l^- R^+$	C_i^p	C_i^N
EM	$l^- n \to l^- R^0$	C_i^n	C_i^N
CC	$\nu p \to l^- R^{++}$	-	$\sqrt{3}\, C_i^{\mathrm{V}} = -\sqrt{3}\, C_i^N$
CC	$\nu n \to l^- R^+$	$C_i^V = C_i^p - C_i^n$	$C_i^{\mathrm{V}} = -C_i^N$

Table 2.6: Nomenclature for the vector form factors of spin-3/2-resonances. The placeholders $\mathcal{C}_i^{\mathrm{V}}$ in Eq. (2.61) are to be substituted with the reaction specific form factors in the two columns on the right, depending on isospin I.

interaction	reaction	$\mathcal{C}_i^{\mathrm{A}}(I=1/2)$	$\mathcal{C}_i^{\mathrm{A}}(I=3/2)$
CC	$\nu n \to l^- R^{++}$	-	$\sqrt{3}\, C_i^{\mathrm{A}}$
CC	$\nu n \to l^- R^+$	C_i^{A}	C_i^{A}

Table 2.7: Nomenclature for the vector form factors of the spin 3/2 resonances. The placeholders $\mathcal{C}_i^{\mathrm{A}}$ in Eq. (2.62) are to be substituted with the reaction specific form factors in the two columns on the right, depending on isospin I.

Axial form factors

Even though Eq. (2.62) now involves four form factors, one can, by once again making use of pion pole dominance, establish a connection between C_5^A and C_6^A. One then finds [Lei09]

$$C_6^{\mathrm{A}}(Q^2) = \frac{M_N^2}{Q^2 + m_\pi^2} C_5^{\mathrm{A}}(Q^2). \tag{2.63}$$

By once more using the off-diagonal Goldberger-Treimann relation,

$$C_5^{\mathrm{A}}(Q^2 = 0) = -C_{\mathrm{iso}} \sqrt{2}\, f_\pi \frac{f}{m_\pi}, \tag{2.64}$$

one coupling can also be fixed. For the remaining form factors, in our model the Δ and the higher resonances are treated differently since, due to good signal-to-background-ratio, the Δ excitation allows for tests of more refined descriptions.

$\mathbf{P_{13}(1720)}$, $\mathbf{D_{13}(1520)}$ and $\mathbf{D_{33}(1700)}$ resonances: Following Ref. [Adl68], the couplings $C_3^{\mathrm{A}}, C_4^{\mathrm{A}}$ can be neglected for these less pronounced resonances. Consequently, the only entity left to determine is the Q^2-dependence of C_5^{A}. In our model, once again the simple dipole ansatz,

$$C_5^{\mathrm{A}}(Q^2) = C_5^{\mathrm{A}}(0) \left(1 + \frac{Q^2}{{M_{\mathrm{A}}^*}^2}\right)^{-2}, \tag{2.65}$$

with the value $M_{\mathrm{A}}^* = 1$ GeV known from QE scattering, is employed. The nomenclature, taken from Ref. [Lei09] is summarized in Table 2.7.

$\mathbf{P_{33}(1232)}$: For this major contribution, we cannot neglect C_4^{A}, and, following Adler [Adl68], we presume that

$$C_4^{\mathrm{A}}(Q^2) = -\frac{C_5^{\mathrm{A}}(Q^2)}{4} \quad \text{and} \quad C_3^{\mathrm{A}}(Q^2) = 0. \tag{2.66}$$

Since $C_5^{\mathrm{A}}(0)$ is fixed by PCAC through Eq. (2.64), the remaining degree of freedom is the Q^2-dependence of C_5^{A}. Starting again with the dipole ansatz,

$$\left(C_5^{\mathrm{A}}\right)^{\mathrm{DP}}(Q^2) = C_5^{\mathrm{A}}(0)\left(1+\frac{Q^2}{M_{\mathrm{A}}^{\mathrm{DP}\,2}}\right)^{-2}, \tag{2.67}$$

and using the axial mass $M_{\mathrm{A}}^{\mathrm{DP}} = 1\mathrm{GeV}$, in the left panel of Fig. 5.6 of Ref. [Lei09] good accordance with the $\nu p \to l^- p \pi^+$ bubble-chamber data for the differential cross section, $\mathrm{d}\sigma/\mathrm{d}Q^2$, from Brookhaven (BNL) [K$^+$86, K$^+$90] but poor agreement with bubble-chamber data from Argonne (ANL) [B$^+$77, R$^+$82] is achieved. As a refinement, inspired by the deviations from dipole behavior of the QE vector form factor, one can introduce [K$^+$86] the modified dipole ansatz,

$$C_5^{\mathrm{A}}(Q^2) = C_5^{\mathrm{A}}(0)\left[1+\frac{aQ^2}{b+Q^2}\right]\left(1+\frac{Q^2}{M_{\mathrm{A}}^{\Delta\,2}}\right)^{-2}. \tag{2.68}$$

After fitting the parameters to both, BNL and ANL data, one achieves a good accordance (cf. Fig. 5.6 in Ref. [Lei09]) with both data sets, using the parameters $a = -0.25$, $b = 0.04\ \mathrm{GeV}^2$ and $M_{\mathrm{A}}^{\Delta} = 0.95$ GeV, for the Q^2-differential cross section. Unfortunately, the integrated cross sections differs for the two experiments and using the modified dipole ansatz one underestimates the BNL cross section while correctly describing the ANL one (right panel of Fig. 5.7 of Ref. [Lei09]). Hence, a decision for one model has to be made, and for the rest of this work Eq. (2.68) will be used.

2.5 Non-resonant pion background

Since pion-production data from EM scattering lie clearly above the prediction from resonant pion production, the role of the non-resonant pion background has been studied in different experiments and reviewed in Ref. [BL04]. Analyses of pion production in CC reactions, e.g., [RS81] or Section 5.4 of Ref. [Lei09], also show the need for the inclusion of a non-resonant background since for these reactions one misses pion-production strength in the isospin 1/2 channel. In a phenomenological approach, one can express the single-π non-resonant background cross section, $\mathrm{d}\sigma_{\mathrm{BG}}$, as

$$\mathrm{d}\sigma_{\mathrm{BG}} = \mathrm{d}\sigma_{\mathrm{BG}}^{\mathrm{V}} + \mathrm{d}\sigma_{\mathrm{BG}}^{\mathrm{A}} + \mathrm{d}\sigma_{\mathrm{BG}}^{\mathrm{V/A}} \tag{2.69}$$

$$= \mathrm{d}\sigma_{\mathrm{BG}}^{\mathrm{V}} + \mathrm{d}\sigma_{\mathrm{BG}}^{\text{non-V}}, \tag{2.70}$$

where $\sigma_{\mathrm{BG}}^{\mathrm{V/A}}$ stands for the interferences between vector and axial contributions. These interferences may now arise since the entire cross section is parametrized and not the hadronic current. As the non-vector contributions, $\mathrm{d}\sigma_{\mathrm{BG}}^{\text{non-V}}$, appear only in CC scattering experiments, they can be fitted to neutrino data (cf. Sec. 2.5.2).

2.5.1 Vector part

For the vector part of the non-resonant background we will follow Ref. [Bus08] and write it as the difference between the pion production cross section, $\mathrm{d}\sigma_{N\pi}$, as measured in electron-scattering experiments, and the cross section of resonance decay, $\mathrm{d}\sigma^V_{lN\to lR\to lN\pi}$, which relies on the resonance production described in the previous section. For the energy- and solid-angle-differential cross section this relation can be expressed as

$$\frac{\mathrm{d}\sigma^{\mathrm{V}}_{\mathrm{BG}}}{\mathrm{d}\omega\mathrm{d}\Omega_{k'}\mathrm{d}\Omega_{k_\pi}} = \frac{\mathrm{d}\sigma^{\mathrm{V}}_{N\pi}}{\mathrm{d}\omega\mathrm{d}\Omega_{k'}\mathrm{d}\Omega_{k_\pi}} - \sum_R \frac{\mathrm{d}\sigma^{\mathrm{V}}_{lN\to lR\to lN\pi}}{\mathrm{d}\omega\mathrm{d}\Omega_{k'}\mathrm{d}\Omega_{k_\pi}}. \tag{2.71}$$

In order to obtain the first term on the RHS of the above equation, one evaluates the kinematics and finds

$$\frac{\mathrm{d}\sigma^{\mathrm{V}}_{N\pi}}{\mathrm{d}\omega\mathrm{d}\Omega_{k'}\mathrm{d}\Omega_{k_\pi}} = \int \mathrm{d}k^0_\pi \frac{|\mathbf{k}'||\mathbf{k}_\pi|}{512\pi^5}\left[(k\cdot p)^2 - m_l^2 M_N^2\right]^{-1/2}\delta(p^2 - M_N^2)\overline{|\mathcal{M}_{N\pi}|^2}, \tag{2.72}$$

where $\overline{|\mathcal{M}_{N\pi}|^2}$ is evaluated by the usual contraction of the hadronic and the leptonic tensor. A general parameterization has been deduced in Ref. [BDW67] and applied to recent data by the MAID group [MAI]. In analogy to Eq. (2.38), one can express the hadronic current by

$$J^\mu_{N\pi} = \bar{u}(p')\Gamma^\mu_{N\pi}u(p), \tag{2.73}$$

with the vertex function

$$\Gamma^\mu_{N\pi} = \sum_{i=1}^{6} A_i^{N\pi} M_i^\mu. \tag{2.74}$$

It thus consists of six form-factor analogues, $A_i^{N\pi}$, the so-called invariant amplitudes, that again depend on both, interaction and reaction channel, and the corresponding invariants, M_i^μ, which are given by

$$\begin{aligned}
M_1^\mu &= -\mathrm{i}\gamma^5\left(\gamma^\mu \not{q} - q^\mu\right),\\
M_2^\mu &= 2\mathrm{i}\gamma^5\left[P^\mu q\cdot\left(k_\pi - \frac{q}{2}\right) - P\cdot q\left(k_\pi - \frac{q}{2}\right)^\mu\right],\\
M_3^\mu &= -\mathrm{i}\gamma^5\left(\gamma^\mu k_\pi\cdot q - \not{q}k_\pi^\mu\right),\\
M_4^\mu &= -2\mathrm{i}\gamma^5\left(\gamma^\mu q\cdot P - \not{q}P^\mu\right) - 2M_N M_1^\mu,\\
M_5^\mu &= \mathrm{i}\gamma^5\left(q^\mu k_\pi\cdot q - q^2 k_\pi^\mu\right),\\
M_6^\mu &= -\mathrm{i}\gamma^5\left(\not{q}q^\mu - q^2\gamma^\mu\right),
\end{aligned}$$

with $P^\mu = (p+p')^\mu/2$. The invariant amplitudes for charged-current neutrino scattering, $A_i^{N\pi,\mathrm{CC}}$, can be related via isospin relations to the known amplitudes from electroexcitation, $A^{N\pi,\mathrm{EM}}$, following [HNV07].

In order to calculate the cross section of pion production via resonance decay, following Ref. [Bus08] on can make the simplifying assumption that the resonances decay isotropically in their rest-frame. Consequently, the dependence of the decay width on the solid-angle element is a constant and given as

$$\frac{\mathrm{d}\Gamma_{R\to N\pi}}{\mathrm{d}\Omega^{\mathrm{CM}}_{k_\pi}} = \frac{\Gamma_{R\to N\pi}}{4\pi}. \tag{2.75}$$

In this way, the cross section factorizes into resonance excitation and decay and one obtains

$$\frac{\mathrm{d}\sigma^V_{lN\to lR\to lN\pi}}{\mathrm{d}\omega\mathrm{d}\Omega_{k'}\mathrm{d}\Omega_{k_\pi}} = \frac{\mathrm{d}\sigma^{\mathrm{V}}_R}{\mathrm{d}\omega\mathrm{d}\Omega_{k'}}\frac{\mathrm{d}\Gamma_{R\to N\pi}}{\mathrm{d}\Omega_{k_\pi}} = \frac{\mathrm{d}\sigma^{\mathrm{V}}_R}{\mathrm{d}\omega\mathrm{d}\Omega_{k'}}\frac{1}{4\pi}\frac{\Gamma_{R\to N\pi}}{\Gamma_{R\to N\pi}}\frac{\mathrm{d}\Omega^{\mathrm{CM}}_{k_\pi}}{\mathrm{d}\Omega_{k_\pi}}. \tag{2.76}$$

Thus, by evaluating the resonance-production cross section, $\mathrm{d}\sigma^V_R$, from the previous section, inserting the experimental decay widths and performing a solid-angle transformation from center of momentum (CM) to the laboratory system, given in Ref. [BK73] as

$$\frac{\mathrm{d}\Omega^{\mathrm{CM}}_{k_\pi}}{\mathrm{d}\Omega_{k_\pi}} = \frac{\sqrt{p'^2}\,\mathbf{k}_\pi{}^2}{|\mathbf{k}^{\mathrm{cm}}_\pi|(|\mathbf{k}_\pi|p'^0 - |\mathbf{p}'|k^0_\pi\cos\theta_\pi)} \quad \text{with} \quad \theta_\pi = \measuredangle(\mathbf{k}_\pi, \mathbf{p}'), \tag{2.77}$$

one can obtain the cross section for resonance decay and estimate the non-resonant background. A word of caution should be spoken at this point, as the difference in Eq. (2.71) may also become negative. This causes problems if the cross section is to be interpreted probabilistically, e.g., in a Monte-Carlo-sampling algorithm. In Sec. 5.5 of Ref. [Bus08], a way to resolve these complications is presented.

2.5.2 Non-vector part

Since neutrino data are scarce, our model includes a rather simple ansatz for the non-vector part of the non-resonant background, by claiming that the non-vector cross section has the same functional form as the vector part and thus can be obtained through multiplication with a reaction-channel-specific constant, $b^{N\pi}$. The total non-resonant cross section then reads [Lei09]

$$\mathrm{d}\sigma_{\mathrm{BG}} = \mathrm{d}\sigma^{\mathrm{V}}_{\mathrm{BG}} + \mathrm{d}\sigma^{\text{non-V}}_{\mathrm{BG}} = (1 + b^{N\pi})\mathrm{d}\sigma^{\mathrm{V}}_{\mathrm{BG}}. \tag{2.78}$$

A fit to ANL data leads to values of $b^{p\pi^0} = 3$ and $b^{n\pi^+} = 1.5$ (cf. Fig. 6.2 in Ref. [Lei09]).

Chapter 3

Model-building for lepton-nucleus scattering

In this chapter, we present the inclusive lepton-nucleus-scattering cross section, which will be the central point of interest for the rest of this work. At first, basic terminology is introduced in the discussion of electron scattering results. Then, we proceed to highlight different aspects that have to be taken into account when attempting to describe lepton-nucleus scattering.

3.1 Inclusive cross sections

Since quantum-chromodynamics calculations are, up to this day, not able to describe all the properties of the nucleon discussed in the last chapter, the idea of using the same formalism to describe even more complex hadronic systems as the nucleus must be abandoned. Left with no microscopic theory as a starting point, one must resort to phenomenological descriptions of the system's properties that one is interested in. Parameterizations of ground state properties, such as the semi-empirical mass formula derived from the liquid drop model, began emerging soon after the discovery of the nucleus. Later, these parameterizations were refined by quantum-mechanical shell models and certain nuclear properties were addressed in quantum-field theory based approaches as the Walecka mean-field model [Wal74].

Before discussing the predictive power of different model assumptions, it is once again important to ask, which properties we are interested in, as the complexity of the nuclear response contains and surpasses all complexity of the nucleon response. Let us compare the schematic depiction of Q^2 cuts through the nuclear response in Fig. 3.1 to the nucleon response in Fig. 2.4. One sees that while at high $Q^2 > 5$ GeV the response is similar to that of a single nucleon, at lower Q^2 new structures can be found in the spectra.

Looking at the effects for $Q^2 = 0$, i.e., real photon scattering, one finds that while the resonance excitation at high ω is similar to that in elementary reactions, at very low ω there is a pronounced peak, associated with a dominant collective excitation of all nucleons, called the giant resonance.

For intermediate Q^2 in the order of 100 MeV one finds a pronounced peak at $\omega = Q^2/2M_{\text{nucleus}}$ from elastic scattering of the entire nucleus, which is followed by a spectrum

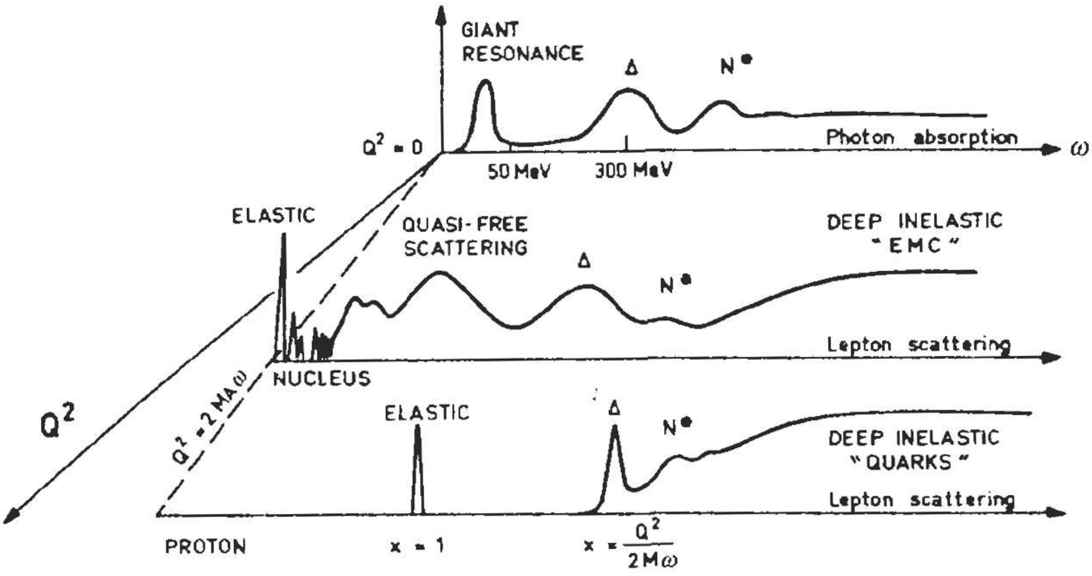

Figure 3.1: Schematic representation of nuclear response function as a function of energy transfer, ω, for different slices of four-momentum transfer Q^2. Taken from [BGPR96].

of nuclear excitations associated with inelastic scattering. Another peak is found at

$$\omega_{\mathrm{QEP}} = Q^2/2M_N. \tag{3.1}$$

It can be associated with the knock-out of a quasi-free nucleon at rest, and is hence referred to as the quasielastic peak (QEP). As for medium four-momentum transfers with $Q^2 \approx 1$ GeV quasielastic scattering dominates the cross section and still plays an important role at higher momentum transfers, its study will be one of the main aspects of this work. Eq. (3.1) falls short of properly describing the position of the peak, since the struck nucleon still experiences binding effects from the other nucleons. In the following, it will be discussed how to include these effects while still sticking to the most simple one-nucleon knock-out picture.

3.2 Modeling the interaction

As a basic assumption, many models begin by treating the lepton part in one-boson-exchange approximation, as we have already done in the previous chapter and depicted in Fig. 2.1a. Following this approach, we focus on the question, to which degrees of freedom the virtual boson couples when it hits the nucleus. There is, actually, a wide range of possibilities, two of which are listed here:

3.2.1 Coupling to a single nucleon: The impulse approximation

In the scenario of impulse approximation, one nucleon is regarded as quasi-free within the nucleus. When hit, it takes up the entire energy and momentum transfer and leaves the nucleus. Taking into account that the largest known nucleon binding energy is found

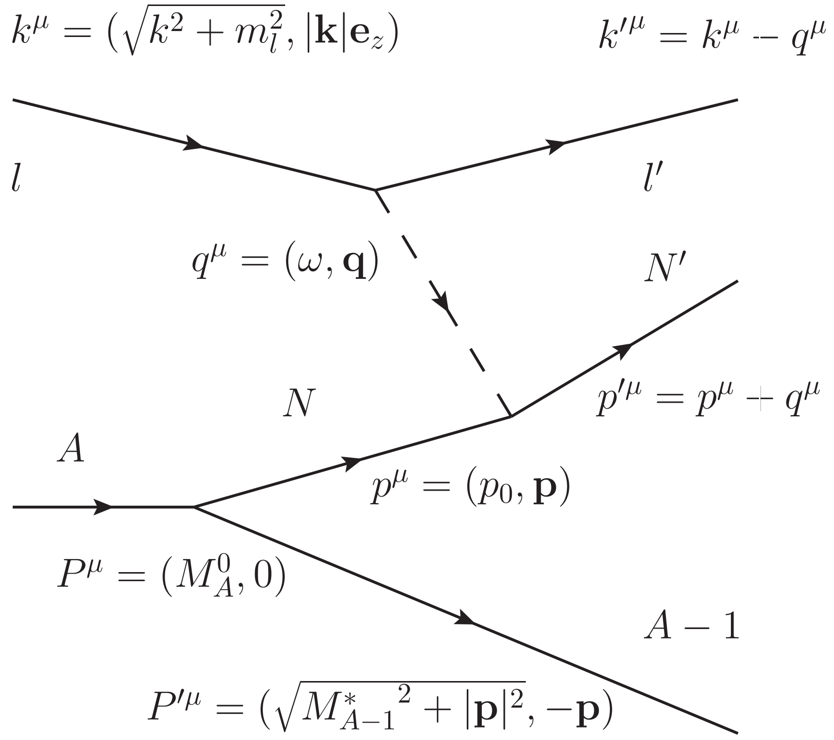

Figure 3.2: Explanation of the impulse approximation: Because the nucleon is quasi-free within the nucleus, it can be described as spontaneously separated from the nucleus with momentum p, then being struck by the virtual boson and consequently leaving the rest nucleus behind.

to be less than 10 MeV [WAT03], this approximation should be appropriate for energy transfers of hundreds of MeV. Our model, that will be explained in Chapter 5, takes this approach as the starting point for both, EM and CC scattering. We note, however, that this concept cannot be expected to hold for low q and the question when and to what extent impulse approximation breaks down is an unresolved issue. A discussion about the implications for neutrino scattering can be found in Ref. [ABF10].

Within this approach, questions concerning off-shell effects have to be addressed. In Fig. 3.2 we have depicted the chain of events in more detail:

1. the nucleon is quasi-free within the nucleus, thus we describe it as spontaneously separated from the nucleus with momentum $\mathbf{p}$, the rest nucleus thus has the momentum $-\mathbf{p}$,

2. after being struck by the virtual boson and changing momentum to $\mathbf{p}' = \mathbf{p} + \mathbf{q}$, it leaves the rest-nucleus behind.

At each vertex, energy conservation has to be fulfilled. As a consequence, all scattering partners, i.e., the nucleus, the rest nucleus and the nucleon, cannot be on shell and in a ground state at the same time.

Evidently, one fixes the initial nucleus in its ground state. In addition, one has the freedom to put the nucleon off mass shell, since it is described by an internal line, and, further, to put the rest nucleus into an excited state, because it is clear that the formation of the energy-minimizing configuration will not occur instantaneously after an inner part of the preceding system has been removed.

At the second vertex one would expect the nucleon to go on shell, but this is by no means a necessity. In fact, at the point of interaction the nucleon is exposed to the hadronic potential, which, depending on the momentum dependence of the potential, might be stronger or weaker than the one acting on the incoming nucleon. More light on these problems is shed throughout the next sections and in Sec. 4.3.

As an approximation, one could circumvent these complications by demanding on-shellness for all particles. To comply with energy conservation, the model then has to use nuclear masses differing from the experimentally observed ones. This approach will be continued in Sec. 4.4.

3.2.2 Nucleon-nucleon correlations

It is an interesting and up until now unresolved issue, at which energies the impulse approximation breaks down and nucleon-nucleon correlations within the nucleus begin to play a significant role, and to what extent they are still present at larger energy transfers. As analysis of the separated longitudinal and transverse responses was a driving force in the study of short range correlation, described, e.g., in the 2p2h excitation model [FF89]. We will postpone the discussion to Sec. 6.2.

3.3 Modeling the scattering partners

From Fig. 3.2, one would expect all incoming and outgoing particles to be represented by plane waves. A more realistic model should take two additional effects into consideration:

Coulomb distortion of the lepton wave function. The more protons a nucleus is made of, the less negligible these distortions of the lepton-wave function become. As Coulomb corrections are momentum dependent (cf., e.g., [dFW66]), their influence on the cross section is an interesting question, discussed, e.g., in Sec. 11 of Ref. [BDS08].

Influence of the hadronic potential on the nucleon. As described above, neither the incoming nor the outgoing nucleon should be expected to be completely free of the nucleon-nucleon potential within the nucleus. Thus a hadronic potential should be defined, leading to an off-shellness of the nucleons.

3.4 Medium-modified cross sections

Assuming one-boson exchange, impulse approximation and neglecting Coulomb corrections, we are now ready to derive the nuclear cross section. Starting with the struck nucleon, we cannot assume its hadronic current to be a quantity without a local dependence anymore. Whether a nucleon at the surface or in the inner part of a heavy nucleus is hit, should have a sizable impact on the response, and in order to obtain the medium-modified matrix element we have to adjust Eq. (2.33) in the following way

$$\overline{|\mathcal{M}|^2} \to \overline{|\mathcal{M}_{\mathrm{med}}(\mathbf{r})|^2}. \tag{3.2}$$

Throughout this work we will present different ways to include medium effects, e.g., in Appendix D.1 we present an approach where the nucleon form factors are modified while in Sec. 5.2.4 the kinematics are changed by the introduction of an effective mass. Using the relations in Sec. 2.2.4 to obtain the cross sections from the squared matrix element, we know the single-nucleon medium-modified cross section to be of the form

$$\mathrm{d}\sigma_{\mathrm{med}}^{lN\to l'f} \propto \overline{|\mathcal{M}_{\mathrm{med}}^{lN\to l'f}(\mathbf{r})|^2} \tag{3.3}$$

$$\mathrm{d}\sigma_{\mathrm{med}}^{lN\to l'X} = \sum_{f=N,\Delta,N\pi,..} \mathrm{d}\sigma_{\mathrm{med}}^{lN\to l'f} \tag{3.4}$$

To obtain the nuclear cross section, we have to integrate over all possible positions, momenta and energies, i.e. the particle-phase-space density, $g_N^<(\mathbf{r}, t = t_0, p)$, yielding

$$\mathrm{d}\sigma^{lA\to l'X} = \sum_{N=n,p} \int \mathrm{d}^3\mathbf{r} \int \frac{\mathrm{d}^4p}{(2\pi)^4} g_N^<(\mathbf{r}, t = t_0, p) f_{\mathrm{corr}} \mathrm{d}\sigma_{\mathrm{med}}^{lN\to l'X}. \tag{3.5}$$

The above equation also includes a correction for the flux of the nucleus,

$$f_{\mathrm{corr}} = \frac{|v_N - v_l|}{|v_A - v_l|}, \tag{3.6}$$

that arises from integrating over single-nucleon cross sections. The discussion about the momentum distribution and off-shellness encoded in the quantity $g_N^<(\mathbf{r}, t = t_0, p)$ is postponed to Chapter 5. To end this section, let us consider the less general but important case of on-shell nucleons, being described by an energy-independent phase-space density $f_N(\mathbf{r}, \mathbf{p}, t = t_0)$. For the study of inclusive scattering we have to integrate over the initial phase-space density at $t = t_0$, omitting the time information in the following. The cross section then reads

$$\mathrm{d}\sigma^{lA\to l'X} = \sum_{N=n,p} \int \mathrm{d}^3\mathbf{r} \int \frac{\mathrm{d}^3\mathbf{p}}{(2\pi)^3} f_N(\mathbf{r}, \mathbf{p}) f_{\mathrm{corr}} \mathrm{d}\sigma_{\mathrm{med}}^{lN\to l'X}. \tag{3.7}$$

Integrating f_N over momentum space (coordinate space) yields the particle density (momentum distribution[1]), i.e.,

$$\int \frac{\mathrm{d}^3\mathbf{p}}{(2\pi)^3} f_N(\mathbf{r}, \mathbf{p}) = \rho_N(\mathbf{r}), \tag{3.8}$$

$$\int \mathrm{d}^3\mathbf{r} f_N(\mathbf{r}, \mathbf{p}) = n_N(\mathbf{p}). \tag{3.9}$$

Performing both integrations yields the normalization,

$$\int \frac{\mathrm{d}^3\mathbf{p}}{(2\pi)^3} \int \mathrm{d}^3\mathbf{r} f_N(\mathbf{r}, \mathbf{p}) = \int \mathrm{d}^3\mathbf{r} \rho_N(\mathbf{r}) = \int \frac{\mathrm{d}^3\mathbf{p}}{(2\pi)^3} n_N(\mathbf{p}) = \mathcal{N}_N, \tag{3.10}$$

where $\mathcal{N}_N$ denotes the number of nucleons of the given species, i.e., $\mathcal{N}_n = N$ and $\mathcal{N}_p = Z$.

[1]Note that in some definitions of the momentum distribution the normalization factor $1/(2\pi)^3$ from Eq. (3.10) does not appear, e.g., in Eq. (6.31) of [BGPR96].

3.5 Modeling the nucleus

3.5.1 Density distributions

As density distributions are accessible via different probes, there are many parameterizations in literature. For heavier nuclei, a good choice is to take the well known Woods-Saxon distribution,

$$\rho_{n,p}(|\mathbf{r}|) = \frac{\rho_0}{1+\exp\left(\frac{|\mathbf{r}|-R_{n,p}}{a_{n,p}}\right)}. \tag{3.11}$$

One possible way to fix the fit parameters for protons in the above equation is the analysis of elastic scattering of electrons on nuclei as performed in Ref. [DJDVDV74]. Since there is no simple way to couple to the neutrons only, it is more difficult to obtain the separated neutron density, but with model calculations of the nuclear ground state, e.g., Ref. [HL98], it is also possible to assess this quantity.

3.5.2 Momentum distributions

A simple starting point for the nucleon-phase-space distributions, $f_{n,p}(\mathbf{r},\mathbf{p})$, is the Fermi-gas model (FG) at temperature $T=0$, with

$$f(|\mathbf{p}|)^{\mathrm{FG}}_{n,p} = N\theta(k_{\mathrm{F}}^{n,p} - |\mathbf{p}|), \tag{3.12}$$

where the normalization constant, N, ensures that Eq. (3.10) holds. Within this approach, nucleons are uniformly distributed in momentum space[2] up to the Fermi momentum, $k_{\mathrm{F}}^{n,p}$, which might differ for protons and neutrons. The Pauli exclusion principle restricts the knocked-out nucleon's momentum to $|\mathbf{p}'| > k_{\mathrm{F}}^{n,p}$, a fact that is referred to as Pauli-blocking. As an approximation one could also consider identical Fermi momenta for the two kinds of nucleons.

A further modification can be introduced by taking into account that the binding of the nucleon depends on its position. This leads to a distance-dependent Fermi momentum, $k_{\mathrm{F}}^{n,p}(|\mathbf{r}|)$. The phase-space distribution then reads

$$f^{\mathrm{LTF}}_{n,p}(|\mathbf{p}|) = \Theta(k_{\mathrm{F}}^{n,p}(|\mathbf{r}|) - |\mathbf{p}|). \tag{3.13}$$

Integrating over the momentum distribution for a given point in space, $\mathbf{r}$, and keeping in mind that each momentum can be occupied by two spin 1/2 particles yields the density distribution

$$\rho_{n,p}(|\mathbf{r}|) = 2\int \frac{\mathrm{d}^3\mathbf{p}}{(2\pi)^3}\Theta(k_{\mathrm{F}}^{n,p}(|\mathbf{r}|) - |\mathbf{p}|) = \frac{\left(k_{\mathrm{F}}^{n,p}(|\mathbf{r}|)\right)^3}{3\pi^2}. \tag{3.14}$$

This relation can be used to connect the model parameter $k_{\mathrm{F}}(|\mathbf{r}|)$ to the experimentally measurable nuclear density, $\rho_{n,p}(|\mathbf{r}|)$, through

$$k_{\mathrm{F}}^{n,p}(|\mathbf{r}|) = \left(3\pi^2\rho_{n,p}(|\mathbf{r}|)\right)^{1/3}. \tag{3.15}$$

For the rest of this work, we will refer to this model as the local Thomas-Fermi gas (LTF).

[2] As a consequence, the dependence on the nucleon's position disappears.

Chapter 4

Superscaling formalism

In this chapter, we introduce the concept of superscaling. We give an overview of different scaling approaches, namely non-relativistic and relativistic y-scaling, after outlining the basic idea behind all scaling analyses. Finally, we illuminate the concept of superscaling and recent modifications to it.

4.1 Introduction to scaling

Scaling is a general phenomenon occurring in various areas of physics that deal with probes weakly interacting with many-body systems [Wes75]. In a typical scattering experiment that exhibits scaling behaviour, a single constituent of the target absorbs the entire energy and momentum transfer. Superscaling is the reduction of the target response to a simple function of one kinematical variable (scaling of first kind) independent of the special form of the target (scaling of second kind). The validity of the concepts of scaling and superscaling applied to inclusive quasi-elastic electron scattering at intermediate energies has been investigated in depth, e.g. in Refs. [DMDS90, DS99, MDS02]. In more recent works, the approach has been extended to neutrino-nucleus scattering [ABC$^+$05]. Whereas for CC neutrino scattering some comparison to different datasets is expected to be possible in the near future with data from SciBooNE [Sci], T2K [T2K] or MINERνA [DST$^+$04], the NC case (cf. Ref. [ABCD06]) is very difficult to assess experimentally, since reconstruction of the incoming/outgoing lepton kinematics is not feasible.

The general approach in the case of lepton-nucleus scattering can be summarized as follows:

1. At first, the **interaction** has to be modeled. This is usually done in impulse approximation, i.e., under the assumption that during the scattering process one virtual photon is exchanged with a single nucleon, which is then knocked-out.

2. Incoming and outgoing **lepton**s are often represented by plane-wave functions, neglecting further interactions with the nuclear Coulomb field.

3. To describe the **nucleus**, one usually makes the ansatz of an ensemble of non-interacting fermions (e.g., a Fermi gas).

4. After the **separation** of the trivial kinematical factors from the cross sections evaluated using the approximations 1-3, one is left with the nuclear response functions.

5. Usually, they can be shown to depend strongly on one combination of kinematical variables (the **scaling variable**) and only weakly on other combinations, which are neglected.

6. After this approximation one can divide out kinematical factors and is left with one universal function (the **scaling function**) depending on only one variable which incorporates all of the nontrivial nucleus response. Dividing the experimental cross sections by the same kinematical factors leads to the experimental scaling function.

7. Finally, one analyzes whether the experimental scaling functions exhibit **scaling of first and second kind**, i.e., whether the scaling function takes on the same values for different kinematical regimes and different nuclear targets.

The above approximations can be refined, eventually leading to a more realistic description. Thus, a variety of different scaling models can be found in the literature (cf., e.g., Ref. [Osb95]). For historical reasons, we shall give a brief overview of well known scaling approaches, focusing on the main results while not evading explicit calculations. It is noteworthy, that all calculations will include the one-boson exchange approximation (cf. Fig. 2.3) leading to the application of the nomenclature developed in Sec. 2.2.3 for the kinematics. Throughout this chapter the shorthand $q = |\mathbf{q}| = \sqrt{(\mathbf{p}_f - \mathbf{p}_i)^2}$ will appear in most formulae, its frequent usage justifying the slight variation from the conventions for the notation of vectors defined in Appendix A.

4.2 Non-relativistic y-scaling

West's seminal analysis [Wes75] of scaling phenomena has been the inspiration for many following studies. However, his analysis is too general for this discussion and we refer the reader to Appendix C.1, where we have extracted a line of reasoning most relevant to this work.

For many reasons, it is more instructive to begin with the non-relativistic Fermi gas and obtain the very same scaling variable, y. As described in Sec. 3.5.2, for the nucleon species N, the global Fermi gas consists of $\mathcal{N}_N$ nucleons evenly distributed in momentum space up to the Fermi momentum, k_{F}^N. Following the derivation in Chapter 5 of Ref. [dFW66] we assume the nucleons to be pointlike and spinless and thus only take scattering off protons into consideration, writing $k_{\mathrm{F}} = k_{\mathrm{F}}^p$. With these approximations, one can write (cf. Sec. 3 of Ref. [dFW66]) the single-proton-cross section as

$$\left(\frac{\mathrm{d}\sigma}{\mathrm{d}\Omega_{k'}\mathrm{d}k^{0'}}\right)_{\mathrm{sp}} = \left(\frac{\mathrm{d}\sigma}{\mathrm{d}\Omega_{k'}}\right)_{\mathrm{Mott}} \left(\frac{Q^2}{q^2}\right)^2 \delta\left[\omega - \left(\frac{(\mathbf{p}+\mathbf{q})^2}{2M_N} - \frac{\mathbf{p}^2}{2M_N}\right)\right] \theta(|\mathbf{p}+\mathbf{q}| - k_{\mathrm{F}}), \quad (4.1)$$

with $\theta(|\mathbf{p}+\mathbf{q}| - k_{\mathrm{F}})$ accounting for Pauli-Blocking and the Mott-cross section given as

$$\left(\frac{\mathrm{d}\sigma}{\mathrm{d}\Omega_{k'}}\right)_{\mathrm{Mott}} = \left(\frac{\alpha\cos(\theta/2)}{2k^0\sin(\theta/2)^2}\right)^2. \quad (4.2)$$

To normalize the phase-space distributions, one must remember that the integral over the entire initial-state phase space must amount to the number of scattering partners, i.e., $\int \mathrm{d}^3\mathbf{r}\rho(\mathbf{r}) = \int \frac{\mathrm{d}^3\mathbf{p}}{(2\pi)^3} n(\mathbf{p}) = Z$, with the proton number, Z. We determine the normalizations to be

$$c_1 \int_\Omega \mathrm{d}^3\mathbf{r} \stackrel{!}{=} Z \rightarrow c_1 = \frac{Z}{|\Omega|} \rightarrow \rho(\mathbf{r}) = \begin{cases} \frac{Z}{|\Omega|} & \mathbf{r} \in \Omega \\ 0 & \text{else,} \end{cases} \tag{4.3}$$

$$c_2 \int_{|\mathbf{p}| \leq k_\mathrm{F}} 2\frac{\mathrm{d}^3\mathbf{p}}{(2\pi)^3} \stackrel{!}{=} Z \rightarrow c_2 = \frac{Z3\pi^2}{k_\mathrm{F}^3} \rightarrow n(\mathbf{p}) = \begin{cases} \frac{Z3\pi^2}{k_\mathrm{F}^3} & |\mathbf{p}| \leq k_\mathrm{F} \\ 0 & \text{else,} \end{cases} \tag{4.4}$$

where k_F denotes the proton Fermi momentum, Ω stands for the arbitrary 3-dimensional normalization region ($|\Omega|$ for its volume) and the factor 2 in Eq. (4.4) accounts for the fact that for any given momentum 2 spin states can be occupied. In combination we obtain the phase space density

$$f(\mathbf{r}, \mathbf{p}) = Z\frac{1}{|\Omega|}\mathbb{1}_\Omega(\mathbf{r})\frac{3\pi^2}{k_\mathrm{F}^3}\theta(k_\mathrm{F} - |\mathbf{p}|), \tag{4.5}$$

with the indicator function, $\mathbb{1}_\Omega(\mathbf{r}) = (1 \text{ if } \mathbf{r} \in \Omega; \quad 0 \text{ else})$.

Note that, while the electrons are treated relativistically, the nucleons' energy in the energy-conserving δ function is evaluated in a non-relativistic manner (thus we refer to this approach as *non-relativistic Fermi gas*).

We have now derived all terms necessary to apply Eq. 3.7 and express the nuclear cross section as[1]

$$\frac{\mathrm{d}\sigma}{\mathrm{d}k^{0\prime}\mathrm{d}\Omega_{k'}} = \int \mathrm{d}^3\mathbf{r} \int \frac{\mathrm{d}^3\mathbf{p}}{(2\pi)^3} 2f(\mathbf{r}, \mathbf{p}) \left(\frac{\mathrm{d}\sigma}{\mathrm{d}\Omega'\mathrm{d}k^{0\prime}}\right)_\mathrm{sp} \tag{4.6}$$

$$= \int \frac{\mathrm{d}^3\mathbf{p}}{(2\pi)^3} 2n(\mathbf{p}) \left(\frac{\mathrm{d}\sigma}{\mathrm{d}\Omega'\mathrm{d}k^{0\prime}}\right)_\mathrm{sp} \tag{4.7}$$

$$= \left(\frac{\mathrm{d}\sigma}{\mathrm{d}\Omega_{k'}}\right)_\mathrm{Mott} \left(\frac{Q^2}{q^2}\right)^2 \underbrace{\frac{3Z}{4\pi k_\mathrm{F}^3} \int_0^{k_\mathrm{F}} \mathrm{d}^3\mathbf{p}\; \theta(|\mathbf{p} + \mathbf{q}| - k_\mathrm{F}) \delta\left[\omega - \left(\frac{(\mathbf{p} + \mathbf{q})^2}{2M_N} - \frac{\mathbf{p}^2}{2M_N}\right)\right]}_{R(\mathbf{q}, \omega)}, \tag{4.8}$$

where $R(\mathbf{q}, \omega)$ denotes the response function.

The non-relativistic expression for the energy conservation facilitates the evaluation of the integral, where now two distinct cases can be regarded:

- For $q \geq 2k_\mathrm{F}$ the Pauli-blocking-Heaviside function, $\theta(|\mathbf{p} + \mathbf{q}| - k_\mathrm{F})$, plays no role, and the response function is given as the positive part of a parabola in y,

$$R(q, \omega) = \begin{cases} \frac{3Z}{4\pi}\left(\frac{M_N}{k_\mathrm{F}}\right)\frac{\pi}{q}\left[1 - \left(\frac{y}{k_\mathrm{F}}\right)^2\right] & \text{for} \quad \frac{q^2}{2M_N} - k_\mathrm{F}\frac{q}{M_N} \leq \omega \leq \frac{q^2}{2M_N} + k_\mathrm{F}\frac{q}{M_N} \\ 0 & \text{else.} \end{cases} \tag{4.9}$$

[1]Note that in passing from Eq. (3.7) to Eq. (4.6), we also make the approximation $f_\mathrm{corr} \approx 1$.

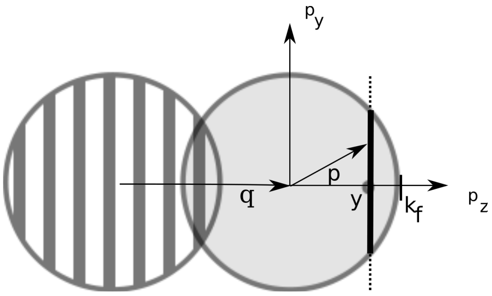

(a) $y > 0$

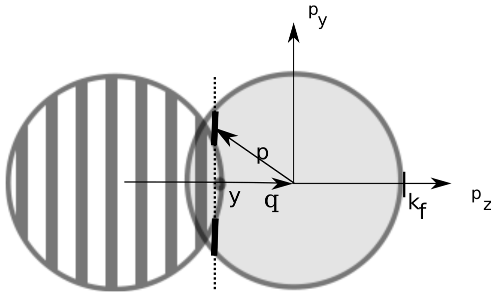

(b) $y < 0$

Figure 4.1: Two-dimensional representation of the initial-state phase space for single-nucleon knockout scattering reactions at a fixed momentum transfer q. The left panel shows a configuration with $2M_N\omega > q^2$, in the right panel we portray a configuration with $2M_N\omega < q^2$. While initially all states with $|\mathbf{p}| < k_\mathrm{F}$ (grey "Fermi circle") are occupied, only those states lying on the dotted straight line are permitted by energy conservation to take part in the reaction. An additional restraint is posed by Pauli-blocking which prevents knocked-out nucleons to be scattered to a state with $|\mathbf{p}| < k_\mathrm{F}$. The region being affected by Pauli-blocking is a "Fermi circle" shifted by the momentum transfer $\mathbf{q}$ (circle filled with stripes). As a consequence, in the right panel only the two bold line segments, which are the intersection of the energy-conservation line with the non-Pauli-blocked phase space, form the initial-state-phase space for the reaction. Passing to three dimensions the circles transform into spheres and the straight into a plane.

Note that the scaling variable,

$$y = \frac{2M_N\omega - q^2}{2q}, \tag{4.10}$$

which also appears in West's more general derivations [Wes75], arises simply as a consequence of energy conservation, since $\mathbf{p} = y\mathbf{e}_q$ is the solution[2] to the equation

$$\omega = \frac{(\mathbf{p}+\mathbf{q})^2}{2M_N} - \frac{\mathbf{p}^2}{2M_N} \tag{4.11}$$

which minimizes $|\mathbf{p}|$. The variable, y, takes on the value 0 at the non-relativistic position of the quasielastic peak, where

$$\omega_0 = \frac{q^2}{2M_N}. \tag{4.12}$$

A graphical interpretation of the energy-conservation condition is given in Fig. 4.1.

- For $q < 2k_\mathrm{F}$ Pauli-blocking is possible. Due to the energy-conserving δ function, $\delta\left(\omega + \frac{\mathbf{p}^2}{2M_N} - \frac{(\mathbf{p}+\mathbf{q})^2}{2M_N}\right)$, blocking only plays a role at $\omega < (2qk_\mathrm{F} - q^2)/2M_N$. As a consequence, the response is given as

$$R(q,\omega) = \begin{cases} \frac{3Z}{4\pi}\left(\frac{M_N}{k_\mathrm{F}}\right)\frac{\pi}{q}\left[1 - \left(\frac{y}{k_\mathrm{F}}\right)^2\right] & \text{for} \quad k_\mathrm{F}\frac{q}{M_N} - \frac{q^2}{2M_N} \leq \omega \leq \frac{q^2}{2M_N} + k_\mathrm{F}\frac{q}{M_N} \\ \frac{3Z}{4\pi}\left(\frac{M_N^2}{k_\mathrm{F}^3}\right)2\pi\frac{\omega}{q} & \text{for} \quad 0 \leq \omega \leq k_\mathrm{F}\frac{q}{M_N} - \frac{q^2}{2M_N} \\ 0 & \text{else.} \end{cases} \tag{4.13}$$

[2]Here, $\mathbf{e}_q$ stands for the unit vector parallel to $\mathbf{q}$.

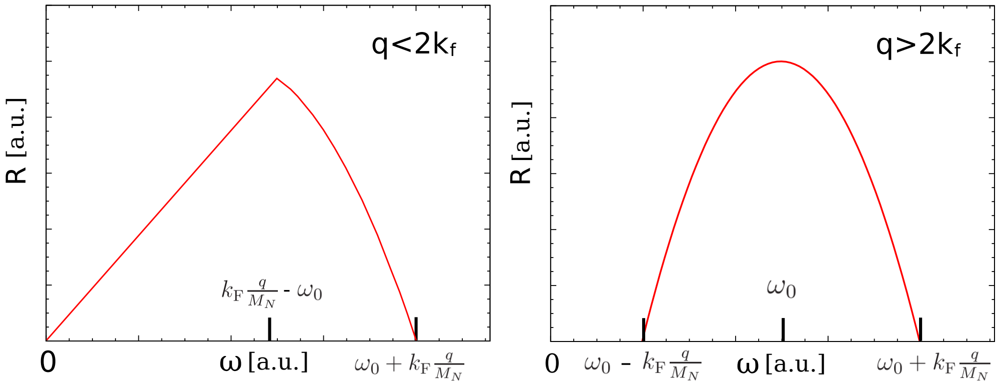

Figure 4.2: Response function, $R(q, \omega)$, as a function of ω. For the left panel, q is chosen such that Pauli-blocking effects play a role. For the right panel, a sufficiently large q has been chosen so that the entire response has a parabolic shape.

While this simple approach misses the position of the QEP, it has been found that adjusting k_F and replacing M_N in the above equations by the fit parameter M^*, called the effective mass, one obtains reasonable accordance with experimental data [MSW+71]. In Fig. 4.2 we portray the two different possible shapes of the response function.

4.3 Relativistic y-scaling in plane wave impulse approximation

Starting in the eighties, groups around Pace, Salmé and Ciofi degli Atti, but also Day and Donnelly have formulated a relativistic version of y-scaling. The first attempts have been quite general and shall be presented here (mostly following the arguments in [CDM97], but also [CdAPS91] and [BGPR96]).

One begins with a fully relativistic description of the semi-inclusive one-nucleon knock-out in electron-nucleus scattering. The process is modeled in one-boson-exchange approximation; the struck nucleon does not couple to the rest of the nucleus (impulse approximation), and both incoming and outgoing leptons are modeled as plane waves. Consequently, this picture is often referred to as the plane-wave-impulse approximation (PWIA). Analyzing the kinematics of the $(e, e'p)$ process, depicted in Fig. 3.2, one finds the following energy-conservation condition:

$$M_A + \omega = \sqrt{(\mathbf{p} + \mathbf{q})^2 + M_N^2} + \sqrt{\mathbf{p}^2 + (M_{A-1}^*)^2}. \tag{4.14}$$

The signifies that the target is at rest prior to the interaction, the rest nucleus thus carrying the momentum $-\mathbf{p}$. The entire momentum transfer is taken by one nucleon, leaving the rest nucleus in an excited state of mass, M_{A-1}^*. Obviously, for a given momentum, there are two extreme kinematical cases: $\mathbf{p}$ being parallel or antiparallel to $\mathbf{q}$. Solving Eq. (4.14) for parallel momentum, $\mathbf{p} = y'\mathbf{e}_q$, we can obtain an analytic expression for the largest value of parallel longitudinal momentum a nucleon can have in order to

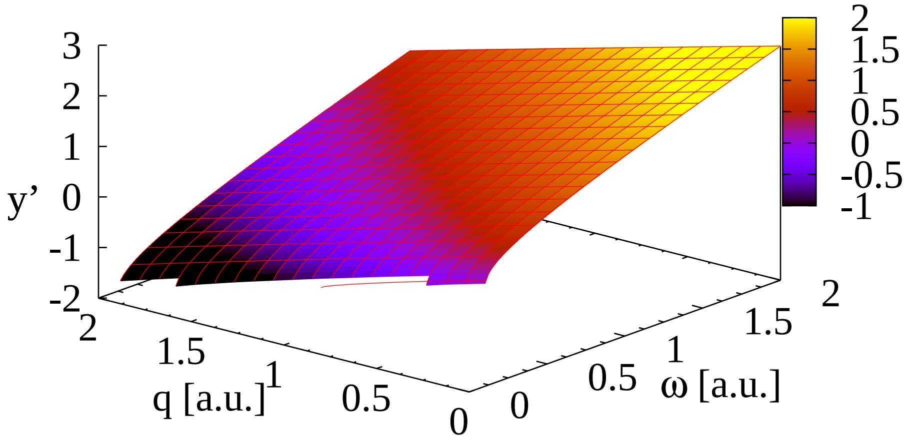

Figure 4.3: Maximum parallel longitudinal momentum, $y'(\omega, q, M^*_{A-1}$ fixed), as a function of both, energy and momentum transfer.

participate in a reaction. It reads [CDM97]

$$y'(M^*_{A-1}) = \frac{1}{2W^2}\Big[(M_A+\omega)\sqrt{W^2-(M^*_{A-1}+M_N)^2}\sqrt{W^2-(M^*_{A-1}-M_N)^2} \\ -q(W^2+(M^*_{A-1})^2-M_N^2)\Big]\,, \tag{4.15}$$

while the invariant mass is given by $W = \sqrt{(M_A+\omega)^2-q^2}$. The largest attainable antiparallel momentum is found to be[3]

$$Y'(M^*_{A-1}) = \frac{1}{2W^2}[(M_A+\omega)\sqrt{W^2-(M^*_{A-1}+M_N)^2}\sqrt{W^2-(M^*_{A-1}-M_N)^2} \\ +q(W^2+(M^*_{A-1})^2-M_N^2)]. \tag{4.16}$$

As shown in Figs. 4.3 and 4.4, regions with $y' > 0$ are associated with large energy transfers. To understand this relation better, we plot the energy loss as a function of parallel nucleon momentum at fixed q in Fig. 4.5. One can see that energy loss increases with the longitudinal momentum in an approximately quadratic manner. The largest energy transfer for fixed q thus occurs, when all $\mathbf{p}_i, \mathbf{p}_f, \mathbf{q}$ point in one direction. This can be assigned to the (leading order) quadratic dependency of the kinetic energy on momentum[4].

Negative values of y' are associated with small energy transfers. This can be understood as follows: very small energy transfers cannot be realised with $\mathbf{p}$ aligned parallel

[3]Note that the solutions y' and $-Y'$ are the two roots of a quadratic equation that arises when inserting $\mathbf{p} = y'\mathbf{e}_q$ into Eq. (4.14) and solving for y'.

[4]Which is a Lorentz invariant property since Q^μ transforms as a four-vector.

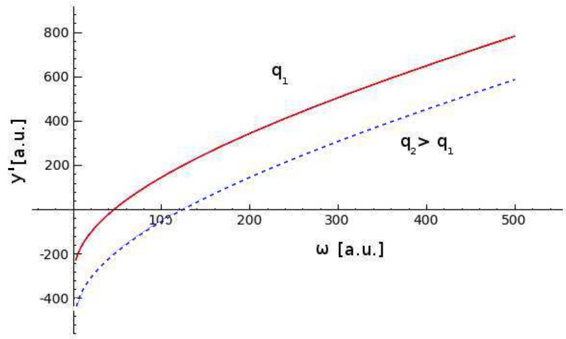

Figure 4.4: Maximum parallel longitudinal momentum, $y'(\omega, q \text{ fixed}, M^*_{A-1} \text{ fixed})$, as a function of ω. The solid curve has been computed with an arbitrary value q_1 for the fixed momentum transfer. The dashed curve has been computed with a fixed momentum transfer $q_2 > q_1$.

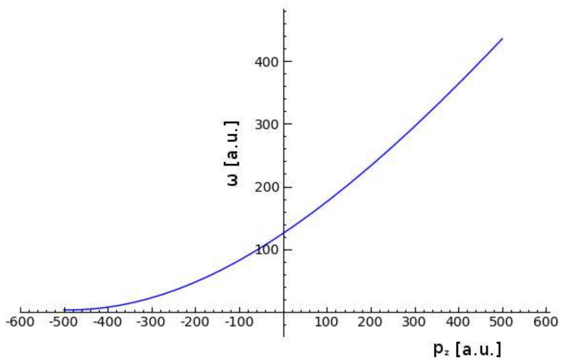

Figure 4.5: Energy transfer, $\omega(p_z, q \text{ fixed}, M^*_{A-1} \text{ fixed})$, as a function of parallel nucleon momentum, p_z.

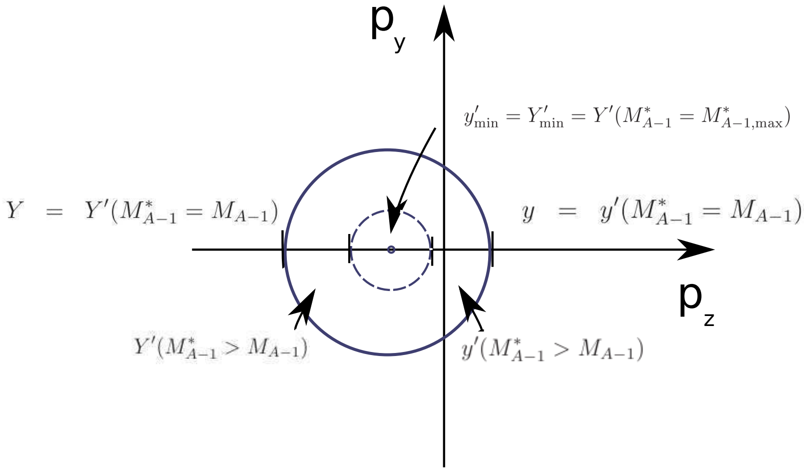

Figure 4.6: Two-dimensional representation of allowed momenta for different rest-nucleon masses, M^*_{A-1}. The solid curve stands for the largest allowed momenta corresponding to the smallest rest-nucleon mass, $M^*_{A-1} = M_{A-1}$. The curve intersects the p_z axis at $p_z = y$ and $p_z = -Y$. The dashed curve represents the allowed momenta for an excited mass state $M^*_{A-1} > M_{A-1}$. The curve intersects the p_z axis at $p_z = -Y(M^*_{A-1})$ and $p_z = y'(M^*_{A-1}) < 0$. The point in the center of both curves stands for the allowed momentum associated with the largest rest-nucleon mass possible for the given kinematics, $M^*_{A-1} = M^*_{A-1,\rm max}$.

to $\mathbf{q}$, thus for low ω only nucleons with antiparallel momentum are allowed to take part in the scattering. To see why $y' < 0$ and $y' > 0$ have to be treated differently, one has to illuminate the role of the mass of the remaining nucleus, M^*_{A-1}. By definition of the ground state $M^*_{A-1} \geq M_{A-1}$. Analyzing Eq. (4.16), one finds the maximum attainable value for anti-parallel momentum to be

$$\begin{aligned} Y = Y'_{\rm max} &= Y'(M^*_{A-1} = M_{A-1}) \\ &= \frac{1}{2W^2}\Big[(M_A+\omega)\sqrt{W^2-(M_{A-1}+M_N)^2}\sqrt{W^2-(M_{A-1}-M_N)^2} \\ &\quad +q(W^2+{M_{A-1}}^2-M_N^2)\Big]\,, \end{aligned} \tag{4.17}$$

while with increasing M^*_{A-1} the Y' will become smaller. In a similar manner, the upper limit for the y' is found to be

$$\begin{aligned} y = y'_{\rm max} &= y'(M^*_{A-1} = M_{A-1}) \\ &= \frac{1}{2W^2}\Big[(M_A+\omega)\sqrt{W^2-(M_{A-1}+M_N)^2}\sqrt{W^2-(M_{A-1}-M_N)^2} \\ &\quad -q(W^2+{M_{A-1}}^2-M_N^2)\Big]\,. \end{aligned} \tag{4.18}$$

Keeping in mind that the energy conservation relation in Eq. (4.14) approximately amounts to an equation of a sphere for $\mathbf{p}$ of the type

$$R^2 = (\mathbf{p}+\mathbf{q})^2, \tag{4.19}$$

we picture the surface of allowed momenta as a sphere in Fig. 4.6, with the positions of the boundaries given by y' and Y'. From the equations for these quantities it can be seen,

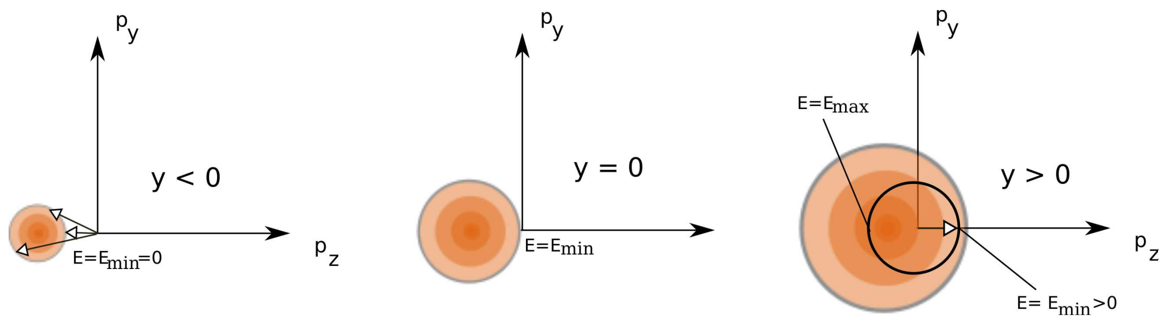

Figure 4.7: Regions of allowed momenta for different kinematical situations. Areas with more intense coloring correspond to areas with higher excitation energies. The arrows represent momenta that minimize the excitation energy, while the inner circle on the right shows different possibilities of aligning the momenta. For $y \leq 0$ every $\mathbf{p}$ within the allowed region can be rotated to the surface of the region where $\mathcal{E} = 0$, for $y > 0$ this is no longer possible for any $\mathbf{p}$. For $|\mathbf{p}| < y$, minimizing excitation energy is done by aligning $\mathbf{p}$ parallel to $\mathbf{q}$, maximizing by aligning in the opposite direction.

that they converge towards a single value for increasing M^*_{A-1}. The surface will eventually become singular, when both, y' and Y', take on the same minimal value at a nucleon mass of $M^*_{A-1,\text{max}} = W - M_N$. For higher excitation energies Eq. (4.16) yields complex results. Thus, as the radius decreases, the convergence point of the surfaces will always be

$$y_c = -q\frac{W^2 + (M^*_{A-1,\text{max}})^2 - M_N^2}{2W^2}. \tag{4.20}$$

Note that, as Eq. (4.14) is continuous in M^*_{A-1} and the surface is connected, in a fully inclusive scenario one obtains a sphere-type volume of allowed momenta, varying the mass from M_{A-1}, associated with allowed momenta on the shell of the volume, up to $M^*_{A-1,\text{max}}$, which only allows for a single momentum close to the center of the volume.

A different way to reflect these findings starts with the excitation energy of the remaining nucleus,

$$\mathcal{E} = E_{A-1} - E^0_{A-1} = \sqrt{\mathbf{p}^2 + (M^*_{A-1})^2} - \sqrt{\mathbf{p}^2 + (M_{A-1})^2}. \tag{4.21}$$

It follows from the definition, that the minimal excitation energy is 0, with the allowed parallel momenta being bounded by y and Y in that case. Let us for the rest of this section use $p = |\mathbf{p}|$ as a short hand. Looking at nucleons with such a fixed absolute momentum, p, two cases, depicted in Fig. 4.7, show substantial differences:

- when $y \leq 0$ the momenta obey the relation $y < p < Y$ and thus for any p fulfilling that relation a $\mathbf{p}$ can be found, so that $\mathcal{E} = 0$
- for $y > 0$ there exist allowed $\mathbf{p}$ with $p < y$, these momenta are associated with excited states only

One can thus easily fix the minimal excitation energy to be

$$\mathcal{E}^{\text{min}}(p) = \max\left(M_A + \omega - \sqrt{p^2 + M_{A-1}} - \sqrt{(p+q)^2 + M_N^2}, 0\right). \tag{4.22}$$

When $y \leq 0$ the minimum excitation energy will always be zero. In the case of $y > 0$ the excitation will be given by the above expression, which can be found by aligning the momentum parallel to $\mathbf{q}$. Since one can always align any allowed momentum antiparallel to $\mathbf{q}$, the maximal excitation energy is given by

$$\mathcal{E}^{\max}(p) = \max\left(M_A + \omega - \sqrt{p^2 + M_{A-1}} - \sqrt{(p-q)^2 + M_N^2}, 0\right). \tag{4.23}$$

To find the overall maximum limit, one has to insert $M^*_{A-1,\max}$ and $\mathbf{p} = y_c \mathbf{e}_q$ into Eq. (6.3) yielding the implicitly lengthy formula

$$\mathcal{E}^{\max} = \sqrt{y_c^2 + M^*_{A-1,\max}} - \sqrt{y_c^2 + M^2_{A-1}}. \tag{4.24}$$

So far, we have analyzed the initial-state-phase space of the struck nucleon and found that energy conservation reduces the available phase space to a sphere-like volume. To parametrize this volume, one can start with the absolute momentum, as done in Ref. [CDM97], and let it vary in the range $\max(-y, 0) \leq p \leq Y$. As a consequence the excitation energy is then bounded by p-dependent limits, i.e., $\mathcal{E}^{\min}(p) \leq \mathcal{E} \leq \mathcal{E}^{\max}(p)$. A different approach starts out by varying the excitation energy in the bounds $0 \leq \mathcal{E} \leq \mathcal{E}^{\max}$ and then varying p in the range $\max(-y'(\mathcal{E}), 0) \leq p \leq Y'(\mathcal{E})$. In any case, the remaining angle integration in ϕ will be trivial, while θ will be bounded by an upper limit depending on both variables in the following way: $0 \leq \theta \leq \theta^{\max}(\mathcal{E}, p)$.

When using the second method, as proposed in Ref. [CdAPS91], due to the complicated structure of Eq. (4.24), it is easier to express the integral in terms of the removal energy,

$$E_\mathrm{R} = (M^*_{A-1} + M_N) - M_A. \tag{4.25}$$

Only in the case of no inner excitation and lack of binding effects will this quantity become 0, depending on binding effects it can also be negative. We can thus rewrite the energy limits in the following way

$$\begin{aligned} E_\mathrm{R}^{\min} &= (M_{A-1} + M_N) - M_A, \\ E_\mathrm{R}^{\max} &= (M^*_{A-1,\max} + M_N) - M_A. \end{aligned} \tag{4.26}$$

As a consequence, the phase-space integration is bounded by the removal energies $E_\mathrm{R}^{\min} \leq E_\mathrm{R} \leq E_\mathrm{R}^{\max}$ and the two momenta $\max(-y'(E_\mathrm{R}), 0) \leq p \leq Y'(E_\mathrm{R})$.

We are now ready to grasp the significance of the scaling variable, y, and the major difference between the cases of positive and negative y. Only in the case of $y \leq 0$ one can attribute a direct physical meaning to y:

The absolute value of y, as defined in Eq. (4.18), is the minimal momentum for a nucleon to be knocked out of the nucleus by a given photon with four-momentum $(\omega, \mathbf{q})$. In addition, this knock-out process will leave the rest nucleus in its ground state, minimizing removal/excitation energy.

In case of $y > 0$ this simple connection is lost, and one is left with the choice between minimizing p or $\mathcal{E}$. Note that minimizing these quantities is important as we expect nucleons to be concentrated in phase-space regions with low p and $\mathcal{E}$.

If we now remind ourselves of the discussion of the QEP in Sec. 3.1, we speak of a quasi-elastic knock-out, when the struck nucleon is at rest and quasi-free, hence has small removal energy. It is thus possible to directly identify the value $y = 0$ as an indicator for the QEP. The great difference in topology for the case $y > 0$, is that as excitation energy increases, y' will diminish and eventually become 0, thus resulting in a process where the struck nucleon is at rest, but has a high removal energy. In such a scenario processes with contributions from inner effects will start to play a dominant role[5].

This argument includes the assumption that the probability $S(p, E_\mathrm{R})$ of hitting a nucleon of momentum p which requires energy E_R to be removed from the nucleus is peaked around $p = 0$ for all removal energies. To avoid confusion, we will refer to $S(p, E_\mathrm{R})$ as the probability function, whereas in many works, e.g. [PS82, CdAPS91], it is called the spectral function. In the context of transport theory, presented in Chapter 5 the term has a slightly different meaning as the spectral function, $\mathcal{A}(\mathbf{r}, t, \mathbf{p})$, explicitly depends on time as well as position and is separated from the phase-space distribution, $f(\mathbf{r}, t, \mathbf{p})$, which also contains information about the momentum distribution. In the special case of a uniformly and infinitely spread fermionic system (here, nuclear matter) all position information is lost and the two quantities $S(p, E_\mathrm{R})$ and $\mathcal{A}(p, E)$ are related to each other, as shown, e.g., in Sec. 3.2 of Ref. [Leh03].

Following the above assumptions (one-boson exchange, plane-wave description, impulse approximation) we are lead to the following separation of single-nucleon contributions and nuclear effects [BGPR96]:

$$\frac{\mathrm{d}^2\sigma}{\mathrm{dE'd\Omega}} = \left[\frac{Z}{A}\sigma_\mathrm{ep} + \frac{N}{A}\sigma_\mathrm{en}\right]\left|\frac{\mathrm{d}\omega}{\mathrm{dp}_\parallel}\right|^{-1} 2\pi \int_{E_\mathrm{R}^\mathrm{min}}^{E_\mathrm{R}^\mathrm{max}} \mathrm{d}E_\mathrm{R} \int_{|y(E_\mathrm{R})|}^{Y'(E_\mathrm{R})} p\ \mathrm{d}p\ S(p, E_\mathrm{R}) \tag{4.27}$$

$$= \left[\frac{Z}{A}\sigma_\mathrm{ep} + \frac{N}{A}\sigma_\mathrm{en}\right]\left|\frac{\mathrm{d}\omega}{\mathrm{dp}_\parallel}\right|^{-1} F(\omega, q). \tag{4.28}$$

Here the factor $\left|\frac{\mathrm{d}\omega}{\mathrm{dp}_\parallel}\right|^{-1}$ accounts for the phase space that is available due to the integration in θ over the energy-conserving δ function, which is also responsible for the appearance of p instead of p^2 in the integral [PS82]. The one-neutron and -proton cross sections, σ_ep and σ_en, are supposed to vary very slowly with p and E_R and are thus factored out of the integral and evaluated at a point within the integration limits[6] (e.g., $E_\mathrm{R} = E_\mathrm{R}^\mathrm{min}$ and $p = |y|$). On the other hand, one should notice that the nucleons will be generally off-vacuum-mass shell due to binding, thus one has to choose a prescription, e.g., Ref. [DF83] which is given in Appendix D.1, to calculate these cross sections.

If one now supposes that $S(p, E_\mathrm{R})$ is peaked around minimal energy and momentum and one is dealing with sufficiently high ω and q, one can safely extend the upper integration limits to infinity. For the deuteron, where $E_\mathrm{R} = E_\mathrm{R}^\mathrm{min}$ is always satisfied due to lack of rest-nucleus degrees of freedom, one can find a very physical interpretation for $F(\omega, q)$:

The probability, $S(p, E_\mathrm{R})$, reduces to a product of the momentum distribution, $n(p)$, and $\delta(E_\mathrm{R} - E_\mathrm{R}^\mathrm{min})$. Instead of writing $y(q, \omega)$ one can interchange dependencies by substituting $\omega \to \omega(y, q)$ and $F(\omega, q) \to F(y, q)$. We find that the only dependence on q in

[5]Note that these contributions are partly responsible for the observed effect of scaling violations that will be described in the following sections.

[6]This approximation is based on the assumption that $S(p, E_\mathrm{R})$ strongly peaks in the vicinity of these limits and that the off-shell cross sections vary relatively little in this vicinity. In model calculations carried out in Ref. [CdAPS91], the assumption was found to hold.

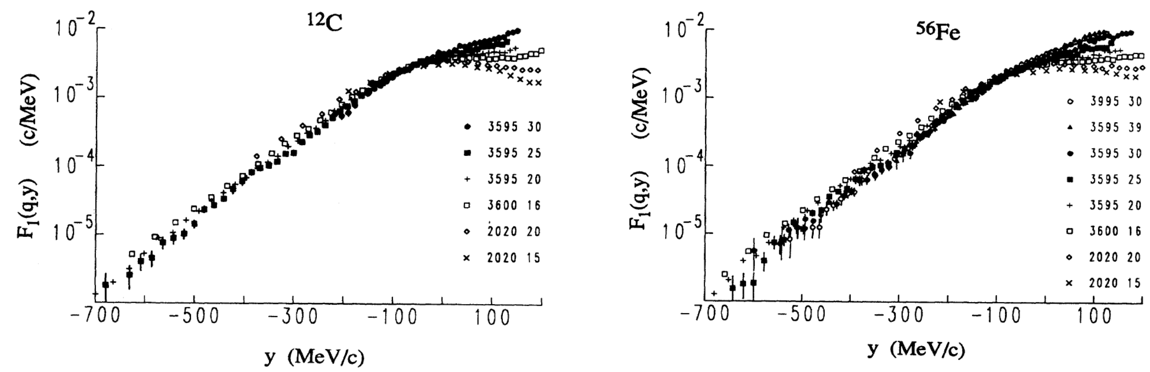

(a) Carbon (b) Iron

Figure 4.8: Experimental scaling function, F, given in 1/MeV plotted vs. y in MeV for ^{12}C and ^{56}Fe, with symbols representing different combinations of incoming energies in MeV (left column) and scattering angles (right column). Taken from [CdAPS91] with data from [DMM^{+}87].

$F(y, q)$ consists of the integration limit $Y(E_{\mathrm{R}})$. Since in the high-q limit we let $Y \to \infty$, our $F(y, q)$ converges to the asymptotic scaling function

$$F_{\infty}(y) = \lim_{q\to\infty} F(y, q) = 2\pi \int_{|y|}^{\infty} pn(p)\mathrm{d}p, \tag{4.29}$$

which is only dependent on y, the remaining **scaling variable**.

Even for more complex nuclei, $n(p)$ can be recovered from $F_{\infty}(y)$; all that needs to be considered is a correction for binding effects, $B(y)$. These have to be estimated from spectral-function calculations using more involved nuclear models. An application of this ansatz can be found in Ref. [CdAPS91].

Summarizing the main aspects and possibilities of this approach, one finds that after starting with PWIA one is able to factorize the one-nucleon knock-out cross-section into a contribution from one-nucleon scattering and trivial kinematics on the one side and an integral over the probability function, $S(E_{\mathrm{R}}, p)$, with limits given by energy conservation on the other. Showing that integration most sensitively depends on the lower momentum limit, y, leads to identifying y as the scaling variable. The integral can be simplified in the case of very high q, yielding the asymptotic scaling function $F_{\infty}(y)$.

When faced with kinematics of a real scattering experiment, the integral cannot be evaluated in an easy fashion. However, the experimental scaling function, $F(y, q)$, obtained by dividing the experimental cross section by the single-nucleon factors, also exhibits reasonable scaling behavior, as portrayed in Fig. 4.8. In Ref. [CdAPS91] it was shown, that the study of the convergence of the scaling function with high q and the extraction of the nucleon momentum distribution, $n(p)$, offer more insight on nuclear dynamics.

4.4 Relativistic Fermi gas and the ψ scaling variable

Even though data exhibit reasonable scaling properties, as shown in the previous section, the y-scaling approach has an important shortcoming. From the definition in Eq. (4.18) one sees that the scaling variable y still depends on the specific experimental values of the nuclear masses, M_{A-1} and M_A. As in the non-relativistic case, one would like to describe the **nucleus** as a collection of independent nucleons, which is most easily achieved in the relativistic Fermi gas (RFG) picture:

Let the nucleus be composed of A free nucleons occupying momenta up to the Fermi momentum, k_{F}. To reduce complexity, the leptons are again modeled as plane waves, and the interaction is treated in impulse approximation.

Again, the starting point is the analysis of possible kinematics. Since the struck nucleon is supposed to be on-shell before and after the interaction, we obtain the following expression for energy conservation,

$$\omega = \sqrt{M_N^2 + (\mathbf{q} + \mathbf{p})^2} - \sqrt{M_N^2 + \mathbf{p}^2}\,. \tag{4.30}$$

Contrary to the energy-conservation relation for the PWIA scenario, given in Eq. (4.14), the above equation does not include contributions from the remaining nucleons. As a consequence, it allows for only one distinct solution,

$$y_{\mathrm{RFG}} = -\frac{q}{2} + \frac{\omega}{2}\sqrt{\frac{4M_N^2 + q^2 - \omega^2}{q^2 - \omega^2}}\,, \tag{4.31}$$

when $\mathbf{p} = y_{\mathrm{RFG}}\mathbf{e}_q$ is aligned parallel to $\mathbf{q}$. Negative y_{RFG}, corresponding to antiparallel alignment, are also possible solutions of Eq. (4.31), but only for low momenta, as $\omega > 0$ and hence $p < q/2$ must be fulfilled. More insight is gained when identifying $|y_{\mathrm{RFG}}|$ as the *minimal absolute momentum of the initial-state nucleon in an on-shell-vacuum scattering reaction.* The minimization of momentum can be understood as in the non-relativistic expansion Eq. (4.30) reduces to (4.11), where additional momentum components orthogonal to $\mathbf{q}$ cancel out.

Plotting y_{RFG} for fixed q, as done in Fig. 4.9, reveals that for low ω it is almost a linear function in ω which passes through zero at the QEP similar to the variable, y, known from PWIA. This again highlights the specific meaning of the QEP being the (ω, q) configuration that allows minimizing of both, initial nucleon momentum and, as we will elucidate in the following paragraphs, final-state energy.

It is more convenient to express the energy of particles of the RFG in terms of dimensionless variables, as proposed in Ref. [AMD+88]. The variables read

$$\begin{aligned} \kappa &\equiv q/2M_N, \quad \lambda \equiv \omega/2M_N, \\ \tau &= \kappa^2 - \lambda^2 = \frac{Q^2}{4M_N^2}, \\ \eta_{\mathrm{F}} &= k_{\mathrm{F}}/M_N, \quad \varepsilon_{\mathrm{F}} = \sqrt{1 + \eta_{\mathrm{F}}^2}\,. \end{aligned} \tag{4.32}$$

An instructive step, presented in Ref. [CDM97], is to recast y_{RFG} in the following form

$$y_{\mathrm{RFG}} = M_N \left[\lambda\sqrt{1 + \frac{1}{\tau}} - \kappa\right]. \tag{4.33}$$

Further, one can use this expression to calculate the corresponding energy of a nucleon with minimal momentum before being struck:

$$
\begin{aligned}
E(|\mathbf{p}| = y_{\mathrm{RFG}}) &= \sqrt{M_N^2 + y_{\mathrm{RFG}}^2} \\
&= M_N(\kappa\sqrt{1+1/\tau} - \lambda) = M_N \Gamma,
\end{aligned}
\tag{4.34}
$$

where the shorthand Γ stands for the dimensionless energy. Finally, one finds for the kinetic energy of this nucleon

$$
\begin{aligned}
E(|\mathbf{p}| = y_{\mathrm{RFG}})_{\mathrm{kin}} &= \sqrt{M_N^2 + y_{\mathrm{RFG}}^2} - M_N \\
&= M_N(\Gamma - 1) = M_N(\varepsilon_{\mathrm{F}} - 1)\frac{\Gamma - 1}{\varepsilon_{\mathrm{F}} - 1} \\
&= M_N(\varepsilon_{\mathrm{F}} - 1)\psi^2.
\end{aligned}
\tag{4.35}
$$

Here, we have introduced the dimensionless variable ψ, which can be recast [BCDP+98] into an explicit form[7] that attributes the correct signs, as

$$
\psi = \frac{1}{\sqrt{\varepsilon_{\mathrm{F}} - 1}} \frac{\lambda - \tau}{\sqrt{(1+\lambda)\tau + \kappa\sqrt{\tau(\tau+1)}}}.
\tag{4.36}
$$

Its square is the kinetic energy of the nucleon before being struck divided by the kinetic energy of a nucleon on the surface of the Fermi sphere, $M_N(\varepsilon_{\mathrm{F}} - 1) = \sqrt{k_{\mathrm{F}}^2 + M_N^2} - M_N$. Hence, ψ can be seen as a *scaled non-relativistic approximation to the relativistic minimal momentum*, y_{RFG}. The two entities can be compared, when making the non-relativistic ansatz for the kinetic energy and introducing y_ψ as

$$
E_{\mathrm{kin}} = M_N(\varepsilon_{\mathrm{F}} - 1)\psi^2 \stackrel{!}{=} \frac{y_\psi^2}{2M_N}
\tag{4.37}
$$

$$
\to y_\psi = M_N\sqrt{2(\varepsilon_{\mathrm{F}} - 1)}\,\psi = \psi\left[k_{\mathrm{F}} + \mathcal{O}\left(\left(\frac{k_{\mathrm{F}}}{M_N}\right)^2\right)\right],
\tag{4.38}
$$

where the last approximation turns out to be fulfilled with good precision for realistic values of $k_{\mathrm{F}}/M_N \approx 1/4$.

It is interesting to compare the different variables, arising from momentum or energy minimization, and in Fig. 4.9 we have plotted the four variables encountered so far. Namely the variable obtained for the non-relativistic Fermi gas, y_{FG}, the one obtained in the relativistic PWIA picture, y_{PWIA}, and the recently introduced y_{RFG} and y_ψ. We find

[7] In terms of dimensionful variables, ψ is calculated from Eq. (4.35) and Eq. (4.31) to be

$$
\psi = \pm\frac{1}{\sqrt{\sqrt{1+\left(\frac{k_{\mathrm{F}}}{M_N}\right)^2} - 1}}\sqrt{1 + \frac{1}{M_N^2}\left(-\frac{q}{2} + \frac{\omega}{2}\sqrt{\frac{4M_N^2 + q^2 - \omega^2}{q^2 - \omega^2}}\right)^2},
$$

where + (-) is to be used when $\omega/(2M_N) \stackrel{(<)}{>} Q^2/(4M_N^2)$.

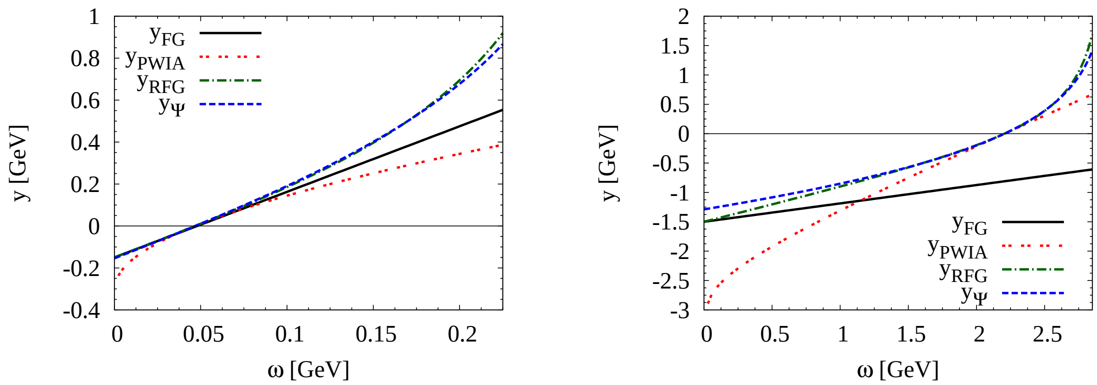

(a) $q = 0.3$ GeV (b) $q = 3$ GeV

Figure 4.9: Comparison of different bounds on parallel momentum: y_{FG} (solid line) defined in Eq. (4.10), y_{PWIA} (dotted line) defined in Eq. (4.18), y_{RFG} (dash-dotted line) and y_ψ (dashed line), which were introduced in this section. In order to easily compute y_{PWIA}, we assumed the large mass number of $A = 197$ and no binding effects, i.e., $M_A = A \cdot M_N$. Realistic masses do not change the general shape.

that at low q, all variables agree with the non-relativistic and linear y_{FG} in the region where it becomes zero. At higher q, y_{FG} is clearly below 0 at the relativistic QEP, where $\omega_{\mathrm{QEP}} = Q^2/2M_N = M_N(\sqrt{1+4\kappa^2} - 1)$, while all other variables are identically 0. One sees, that in this region y_{RFG} is a good approximation for y_ψ, while at very low ω it takes on the same values as the non-relativistic analog. As only in the PWIA scenario the initial-state nucleon is allowed to be off-shell, one observes a considerable difference between y_{PWIA} and all other variables, except at the QEP.

So far, the kinematical properties of the Fermi gas have only entered by providing an energy scale in Eq. (4.35). In order to determine the phase space, one has to consider the restrictions imposed by the FG model. In addition to the upper bound on momentum, k_{F}, for low $q < 2k_{\mathrm{F}}$ there also exists a forbidden region, $|\mathbf{p}+\mathbf{q}| < k_{\mathrm{F}}$, where the nucleon is Pauli-blocked from scattering to a momentum within the Fermi sphere. In a case with no Pauli-blocking, the initial-state momentum-phase space is given simply by the intersection of the Fermi sphere with the surface obtained from energy conservation. While for the non-relativistic case this surface is a plane, it is now slightly parabolic, bending towards larger p_z. When the intersection is not empty, the interpretations of y_{RFG} as the lowest and k_{F} as the largest available momentum remain untouched. When $q < 2k_{\mathrm{F}}$ the simple connection between y_{RFG}, ψ and the minimal momentum are lost, as shown in Fig. 4.10, and thus we do not consider the Pauli-blocked case any further.

To derive a scaling function, we follow [Ros80] and express the double-differential cross section in one-photon-exchange approximation as

$$\frac{\mathrm{d}\sigma}{\mathrm{d}k^{0\prime}\mathrm{d}\Omega_{k'}} = \frac{\alpha^2}{q^4}\frac{k^{0\prime}}{k^0} L_{\mu\nu} W^{\mu\nu}. \tag{4.39}$$

Here, we use the leptonic tensor, Ł$_{\mu\nu}$, defined in Eq. (2.34) and reading in an explicit representation [AMD$^+$88]

$$L_{\mu\nu} = \left(k_\mu k'_\nu + k'_\mu k_\nu - g_{\mu\nu} k \cdot k'\right), \tag{4.40}$$

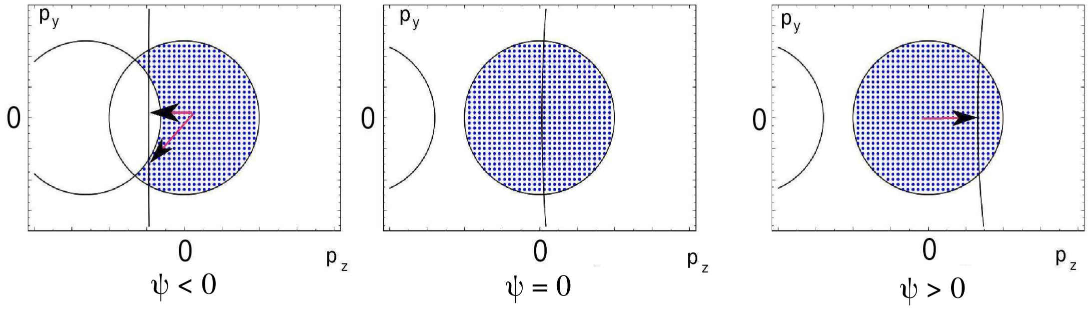

Figure 4.10: Two-dimensional representation of the initial-state phase space (momenta shown in arbitrary units) for different kinematical configurations. Computation of the energy conservation line was performed with fully relativistic kinematics, the remaining entities and their interpretation are identical to Fig. 4.1 and the discussion thereof. In the left panel we have chosen a configuration with $y_{\mathrm{RFG}} < 0$ which in addition exhibits Pauli-blocking (here, $k_{\mathrm{F}} < q < 2k_{\mathrm{F}}$); the situation in the middle panel, with $\psi = 0$, corresponds to kinematics of the vacuum QEP; in the right panel, a configuration with $\psi > 0$ and no Pauli-blocking was chosen, resulting in the minimal nucleon momentum (arrow) being parallel to p_z (i.e., $\mathbf{q}$). In contrast, the kinematical situation in the left panel does not allow for the minimal nucleon momentum (large arrow) to be aligned along p_z (small arrow).

and the single-nucleon hadronic tensor,

$$\begin{aligned} W'^{\mu\nu}(p^\eta + q^\eta, p^\eta) = &-W_1(\tau)\left(g^{\mu\nu} + \frac{q^\mu q^\nu}{Q^2}\right) \\ &+ W_2(\tau)\frac{1}{M_N^2}\left(p^\mu + \frac{p_\eta q^\eta}{Q^2}q^\mu\right)\left(p^\nu + \frac{p_\eta q^\eta}{Q^2}q^\nu\right) \end{aligned} \tag{4.41}$$

where the form factors $W_1(\tau)$ and $W_2(\tau)$ are related to the Sachs form factors introduced in Sec. 2.3.2 through the equations,

$$W_1(\tau) = \tau G_{\mathrm{M}}^2(\tau), \tag{4.42}$$

$$W_2(\tau) = \frac{1}{1+\tau}\left(G_{\mathrm{E}}^2(\tau) + \tau G_{\mathrm{M}}^2(\tau)\right). \tag{4.43}$$

To obtain the scattering-cross section of the relativistic Fermi gas, a normalized sum over all non-Pauli-blocked on-shell momenta up to k_{F} is required. The nuclear hadronic tensor then reads [AMD+88]

$$\begin{aligned} W^{\mu\nu} = &\frac{3\mathcal{N}M_N^2}{4\pi k_{\mathrm{F}}^3}\int \frac{\mathrm{d}^3\mathbf{p}}{E(\mathbf{p})E(\mathbf{p}+\mathbf{q})} \\ &\times \theta(k_{\mathrm{F}} - |\mathbf{p}|)\theta(|\mathbf{p}+\mathbf{q}| - k_{\mathrm{F}})\delta\left\{\omega - [E(\mathbf{p}+\mathbf{q}) - E(\mathbf{p})]\right\} W'^{\mu\nu}(p^\eta + q^\eta, p^\eta), \end{aligned} \tag{4.44}$$

with the normalization factor containing the number of nucleons of a specific kind, $\mathcal{N}$.

Given the hadronic tensor, $W^{\mu\nu}$, one could directly perform the contraction and obtain a cross section [Ros80],

$$\frac{\mathrm{d}^2\sigma}{\mathrm{d}k^{0\prime}\mathrm{d}\Omega_{k'}} = \left(\frac{\mathrm{d}\sigma}{\mathrm{d}\Omega_{k'}}\right)_{\mathrm{Mott}}\left[v_{\mathrm{L}}R_{\mathrm{L}}(q,\omega) + v_{\mathrm{T}}R_{\mathrm{T}}(q,\omega)\right], \tag{4.45}$$

which is separated into contributions from the longitudinal and the transverse response. The responses are defined as

$$R_{\mathrm{L}}(\omega,q)=W^{00},\quad R_{\mathrm{T}}(\omega,q)=-\left(g_{ij}+\frac{q_iq_j}{q^2}\right)W^{ij}\quad i,j\in\{1,2,3\}. \tag{4.46}$$

They will be discussed in more detail in Sec. 6.2. The kinematical factors are defined as

$$v_{\mathrm{L}} = \left(\frac{Q^2}{q^2}\right)^2, \tag{4.47}$$

$$v_{\mathrm{T}} = \frac{1}{2}\frac{Q^2}{q^2}+\tan^2\frac{\theta}{2}. \tag{4.48}$$

To proceed, one needs to evaluate the integral in Eq. (4.44). For the non-Pauli-blocked region, this calculation has been performed in [AMD+88] and yields

$$\begin{aligned} R_{L,T} =& \frac{3\mathcal{N}}{4M_N\kappa\varepsilon_f^3}(\eta_{\mathrm{F}}-\Gamma)\theta(\varepsilon_{\mathrm{F}}-\Gamma)\\ &\times\begin{cases}\dfrac{\kappa^2}{\tau}\{[(1+\tau)W_2(\tau)-W_1(\tau)]+W_2(\tau)\Delta\} & \text{for } L,\\ 2W_2(\tau)+W_2(\tau)\Delta & \text{for } T,\end{cases}\end{aligned} \tag{4.49}$$

with the dimensionless variables as defined above and the kinematical factor,

$$\Delta\equiv\frac{\tau}{\kappa^2}\left[\frac{1}{3}(\varepsilon_{\mathrm{F}}^2+\varepsilon_{\mathrm{F}}\Gamma+\Gamma^2)+\lambda(\varepsilon_{\mathrm{F}}+\Gamma)+\lambda^2\right]-(1+\tau), \tag{4.50}$$

which is shown to be $\approx 1/32$ in Ref. [AMD+88]. It is thus a reasonable approximation to neglect the terms connected with Δ to obtain a linear dependence on Γ, respectively a quadratic dependence on ψ^2 of the form $1-\psi^2$, for the transverse response. With the approximation from Eq. (4.38) this dependence is expressed as $1-(y_\psi/k_{\mathrm{F}})^2$, which matches perfectly with the finding for the non-relativistic response, given in Eq. (4.9).

As the non-relativistic approach has been quite successful in describing the data, one would like to retain a parabolic scaling function as in the non-relativistic case. Thus, the separation of the kinematical factors and the single-nucleon contributions from the scaling function is chosen in the following way

$$\frac{\mathrm{d}^2\sigma}{\mathrm{d}k^{0\prime}\mathrm{d}\Omega}=\frac{\mathcal{N}}{4M_N\kappa}\left(\frac{\mathrm{d}\sigma}{\mathrm{d}\Omega_{k'}}\right)_{\mathrm{Mott}}X(\theta,\tau,\psi;\eta_{\mathrm{F}})S(\psi,\eta_{\mathrm{F}}), \tag{4.51}$$

with the factor

$$\begin{aligned} X(\theta,\tau,\psi;\eta_{\mathrm{F}})\equiv&\left(W_2(\tau)+2W_1(\tau)\tan^2\frac{\theta}{2}\right)\\ &+W_2(\tau)\left[\left(\frac{\tau(1+\tau)}{\kappa^2}-1\right)+\left(\frac{3}{2}\frac{\tau}{\kappa^2}+\tan^2\frac{\theta}{2}\right)\Delta\right]\end{aligned} \tag{4.52}$$

containing the single-nucleon structure. The remaining theoretical scaling function,

$$S(\psi,\eta_{\mathrm{F}})\equiv(1-\psi^2)\theta(1-\psi^2)3\frac{\varepsilon_{\mathrm{F}}-1}{\eta_{\mathrm{F}}^3}, \tag{4.53}$$

contains all relevant information about the nucleon momentum distribution. To study to which extent the assumptions of this model hold, one can perform the same separation as in Eq. (4.51) with the experimental cross section and thus by division obtain the experimental scaling function. In the next section we will discuss methods for improving different properties of experimental scaling functions.

4.5 Superscaling and energy shift

The RFG formalism described above exhibits the same shortcomings as its non-relativistic analog and some of those already mentioned for the PWIA-approach. First of all, the position of the QEP is not exactly reproduced at the kinematics of the vacuum QEP, where y and y_{RFG} equal 0, since due to binding effects the peak is shifted from its vacuum position towards higher ω. Thus, in all cases one has to introduce a fit parameter, E_{shift}, and redefine the ω scale as

$$\omega' \equiv \omega - E_{\mathrm{shift}}, \tag{4.54}$$

consequently also redefining the scaling variable as

$$\psi' \equiv \psi(\lambda = \lambda', \tau = \tau'), \tag{4.55}$$

While the complication of extrapolating to off-shell single-nucleon cross sections is specific to PWIA y-scaling only, we expect a dependence on specific nuclei in every model's scaling function[8]. A straight forward approach [DS99] is to divide all factors containing k_{F} out of the scaling function $S(\psi, \eta_{\mathrm{F}})$ and obtain

$$f(\psi) \equiv S(\psi, \eta_{\mathrm{F}}) \frac{\eta_{\mathrm{F}}^3}{4(\varepsilon_{\mathrm{F}} - 1)} = \frac{3}{4}(1 - \psi^2)\theta(1 - \psi^2). \tag{4.56}$$

Inserting Eq. (4.49) into Eq. (4.45), one finds

$$f(\psi) = k_{\mathrm{F}} \frac{\mathrm{d}^2\sigma/\mathrm{d}\Omega_{k'}\mathrm{d}\omega}{\left(\frac{\mathrm{d}\sigma}{\mathrm{d}\Omega_{k'}}\right)_{\mathrm{Mott}} (v_{\mathrm{L}} G_{\mathrm{L}}^2 + v_{\mathrm{T}} G_{\mathrm{T}}^2)}, \tag{4.57}$$

with the single-nucleon responses,

$$G_{\mathrm{L}}(\kappa, \lambda) = \frac{(\tilde{G}_{\mathrm{E}}^2 + \tilde{W}_2 \Delta)\kappa^2/\tau}{2\kappa\left[1 + (\sqrt{1+\eta_{\mathrm{F}}^2} - 1)(1+\psi^2)/2\right]}, \tag{4.58}$$

$$G_{\mathrm{T}}(\kappa, \lambda) = \frac{2\tau\tilde{G}_{\mathrm{M}}^2 + \tilde{W}_2 \Delta}{2\kappa\left[1 + (\sqrt{1+\eta_{\mathrm{F}}^2} - 1)(1+\psi^2)/2\right]}, \tag{4.59}$$

depending on the averaged form factors

$$\tilde{G}_{\mathrm{E}}^2(\tau) = Z G_{\mathrm{E}p}^2(\tau) + N G_{\mathrm{E}n}^2(\tau), \tag{4.60}$$

$$\tilde{G}_{\mathrm{M}}^2(\tau) = Z G_{\mathrm{M}p}^2(\tau) + N G_{\mathrm{M}n}^2(\tau), \tag{4.61}$$

$$\tilde{W}_1(\tau) = \tau \tilde{G}_M^2(\tau), \tag{4.62}$$

$$\tilde{W}_2(\tau) = \frac{1}{1+\tau}\left(\tilde{G}_{\mathrm{E}}^2(\tau) + \tau\tilde{G}_{\mathrm{M}}^2(\tau)\right). \tag{4.63}$$

[8]This dependence is more involved in the PWIA picture due to experimental nuclear masses, while for the FG and RFG k_{F} is the only nucleus-specific parameter.

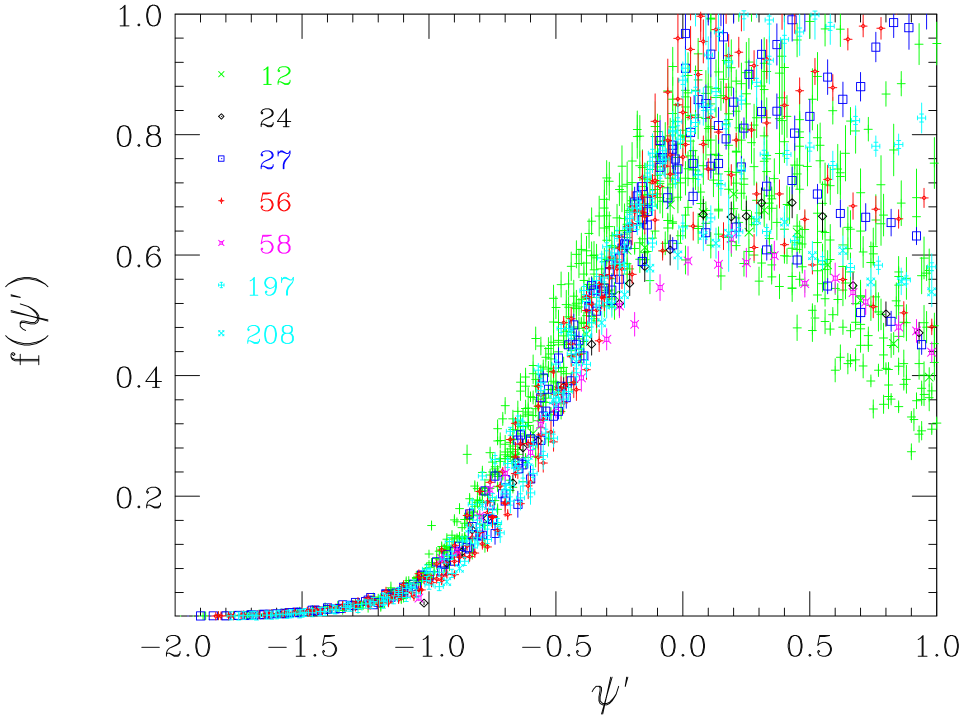

Figure 4.11: Scaling function $f(\psi')$ as a function of ψ' for nuclei with $A \geq 12$, distinguished by color, and different kinematics, obtained from various experiments. Taken from [DS99].

It is an interesting discovery, that even though the experimental scaling function is not of the simple form of a parabola, the above approach in combination with the energy shift has proven to give similar scaling functions for various ranges of A (first-kind scaling) and q (second-kind scaling), as can be seen in Fig. 4.11. Since two separate kinds of scaling are fulfilled, the name superscaling has been given to this property of the data.

4.6 Superscaling analysis of neutrino scattering

As the momentum distribution is a nuclear property and does not depend on the probe, it is tempting to apply the superscaling formalism to neutrino scattering. While NC scattering is experimentally out of reach, the detailed CC response may soon become available. It has already been analyzed in terms of superscaling in Ref. [ABC$^+$05]. Here we shall outline this approach, as it will be applied in Sec. 6.1.3.

As a starting point, one proposes a separation of the scattering-cross section similar to Eq. (4.57), reading

$$\frac{\mathrm{d}\sigma}{\mathrm{d}\Omega_{k'}\mathrm{d}k^{0\prime}} = \sigma_0 \mathcal{F}_\chi^2, \tag{4.64}$$

with the elementary cross section,

$$\sigma_0 = \frac{(G_\mathrm{F}\cos\theta_C)^2}{2\pi^2}\left(k^{0\prime}\cos\tilde{\theta}/2\right)^2, \tag{4.65}$$

depending on the generalized scattering angle,

$$\tan^2 \tilde{\theta}/2 = \frac{Q^2}{4k^0 k^{0\prime} - Q^2}. \tag{4.66}$$

The remaining form-factor analog,

$$\mathcal{F}_\chi = \hat{V}_{\mathrm{CC}} R_{\mathrm{CC}} + 2\hat{V}_{\mathrm{CL}} R_{\mathrm{CL}} + \hat{V}_{\mathrm{LL}} R_{\mathrm{LL}} + \hat{V}_{\mathrm{T}} R_{\mathrm{T}} + 2\chi \hat{V}_{\mathrm{T}'} R_{\mathrm{T}'}, \tag{4.67}$$

contains all nuclear information and also additional information about the probe, as the indicator χ takes on the value 1 for particle and -1 for anti-particle scattering.

Contrary to the separation of the longitudinal and transverse response in electron scattering, where the longitudinal polarization of the photon serves as a natural characteristic (cf. Sec. 6.2), the separation in Eq. (4.67) is one among different options. AS an anolog to the electron case, the responses, $R_{\mathrm{CC}}, R_{\mathrm{CL}}, R_{\mathrm{LL}}, R_{\mathrm{T}}$ and $R_{\mathrm{T}'}$, are obtained from the nuclear tensor. For the details of the derivation we refer the reader to Ref. [ABC+05].

We have already introduced the hadronic tensor for single-nucleon scattering in Sec. 2.3.1. To obtain the nuclear tensor, it is necessary to perform an integration over all target nucleons in the Fermi gas, similar to the integration in Eq. (4.44). But let us postpone this step and write down the kinematical factors obtained from contracting the leptonic with the nuclear tensor. One finds [ABC+05]

$$\hat{V}_{\mathrm{CC}} = 1 - \tan^2\left(\frac{\tilde{\theta}}{2}\right)\delta^2, \tag{4.68}$$

$$\hat{V}_{\mathrm{CL}} = \nu + \frac{1}{\rho'}\tan^2\left(\frac{\tilde{\theta}}{2}\right)\delta^2, \tag{4.69}$$

$$\hat{V}_{\mathrm{LL}} = \nu^2 + \tan^2\left(\frac{\tilde{\theta}}{2}\right)\left(1 + \frac{2\nu}{\rho'} + \rho\delta^2\right)\delta^2, \tag{4.70}$$

$$\hat{V}_{\mathrm{T}} = \left(\frac{1}{2}\rho + \tan^2\left(\frac{\tilde{\theta}}{2}\right)\right) - \frac{1}{\rho'}\tan^2\left(\frac{\tilde{\theta}}{2}\right)\left(\nu + \frac{1}{2}\rho\rho'\delta^2\right)\delta^2, \tag{4.71}$$

$$\hat{V}_{\mathrm{CC}} = \left(\frac{1}{\rho}\tan^2\left(\frac{\tilde{\theta}}{2}\right)\right)\left(1 - \nu\rho'\delta^2\right), \tag{4.72}$$

with the definitions

$$\delta \equiv \frac{m_l}{\sqrt{Q^2}}, \tag{4.73}$$

$$\nu \equiv \frac{\lambda}{\kappa}, \tag{4.74}$$

$$\rho \equiv \frac{\tau}{\kappa^2}, \tag{4.75}$$

$$\rho' \equiv \frac{q}{k^0 + k^{0\prime}}. \tag{4.76}$$

The factor δ deserves special attention, since it accounts for the final-state lepton, e.g. a muon, having a finite mass, m_l. As δ approaches 0, one regains the kinematical factors for electron scattering defined in Eq. (4.47).

Since the integration of the CC nuclear responses involve many more terms than the EM case in Eqs. (4.58) and (4.59), we restrict ourselves to writing the first-order expansion in η_{F} from Ref. [ABC+05]. We begin by rewriting the cross section as

$$\frac{\mathrm{d}\sigma}{\mathrm{d}\Omega \mathrm{d}E'} = \sigma_0 \frac{1}{k_{\mathrm{F}}} f(\psi') \frac{\mathcal{N}}{2\kappa} \mathcal{F}^2_{\chi,\mathrm{s.n.}}, \tag{4.77}$$

where $f(\psi)$ is the scaling function and, $\mathcal{N}$ stands for the number of nucleons involved in the scattering, e.g., $\mathcal{N} = N$ for $\chi = 1$.

The single-nucleon form factor analog is evaluated as,

$$\mathcal{F}^2_{\chi,\mathrm{s.n.}} = X_{\mathrm{L}}^{\mathrm{VV}} + X_{\mathrm{C/L}}^{\mathrm{AA}} + X_{\mathrm{T}} + \chi X_{\mathrm{T'}}, \tag{4.78}$$

with

$$\begin{aligned}
X_{\mathrm{L}}^{\mathrm{VV}} &= \left(\hat{V}_{\mathrm{CC}} - 2\nu \hat{V}_{\mathrm{CL}} + \nu^2 \hat{V}_{\mathrm{LL}}\right) \left(\frac{1}{\rho} G_{\mathrm{E}}^2\right), && (4.79)\\
X_{\mathrm{C/L}}^{\mathrm{AA}} &= \tan^2 \tilde{\theta}/2 \cdot G_{\mathrm{A}}'^2 (1+\delta^2)\delta^2, && (4.80)\\
X_{\mathrm{T}} &= \hat{V}_{\mathrm{T}} \left(2\tau G_M^2 + 2(1+\tau) G_{\mathrm{A}}^2\right), && (4.81)\\
X_{\mathrm{T'}} &= \hat{V}_{\mathrm{T'}} 2\sqrt{\tau(1+\tau)}\, G_{\mathrm{M}} G_A. && (4.82)
\end{aligned}$$

The Sachs-form factors, G_{E} and G_{M}, are defined in Sec. 2.3.2, while the axial-vector and pseudo-vector form factors are related to the ones defined in Sec. 2.3.1 through the relations

$$\begin{aligned}
G_A &= F_A && (4.83)\\
G_P &= 2F_P. && (4.84)
\end{aligned}$$

In the original work, the idea has been to insert a scaling function, $f(\psi')$, obtained from analysis of the longitudinal response of electron scattering into Eq. (4.67) to predict the neutrino response. In Sec. 6.1.3 we will turn this approach around to study to what extent the predicted neutrino response of our model fulfills scaling.

4.7 Superscaling approaches beyond quasielastic scattering

While the methods proposed so far will be employed in the analysis of experimental and GiBUU simulated data in Chapter 6, it is important to point out that the ideas of superscaling have been applied to many other aspects of inclusive lepton-nucleus scattering. One uncertainty, that has been neglected so far, comes from the Coulomb distortion effects, that the lepton wave function will experience in the electric field of heavy nuclei and thus should lead to some effect on second-kind scaling (investigations have been undertaken, e.g., in Ref. [ABB+97]). Further, a major point of interest is the non-scaling of the transverse response, which will be explained in more detail in Sec. 6.2.

In Ref. [MDS02], it has been proposed that scaling violations in the resonance region can be drastically reduced using yet another kind of scaling variable, ψ'_*, incorporating the higher mass, m_*, of the knocked-out resonance. This has also been implemented for CC scattering in Ref. [ABC+05]. In Appendix C.3, we show how this formalism can be applied to the Δ excitation. A similar approach can be applied to the DIS region, integrating over different invariant masses, W. A good summary on this topic is found in Ref. [MAB+09]. It is noteworthy that NC scattering has also been studied [ABCD06].

Chapter 5

Simulation of lepton-nucleus scattering in the GiBUU model

5.1 The Boltzmann-Uehling-Uhlenbeck equation

Transport equations can be applied to a wide range of problems, ranging from fluid mechanics to financial simulations. The underlying microscopic dynamics, as described by the Lagrangian approach in Chapter 2, offers a good starting point for model building. In many applications one looks at non-equilibrium processes that involve a huge number of interacting degrees of freedom, making an exact solution practically impossible. Approximations allow to consider a single-particle phase-space density instead of the individual degrees of freedom, the classical Boltzmann equation being the most prominent example. In special cases, even macroscopic properties can be modeled directly, as pressure and flux in the Navier-Stokes equation. An inspiring overview of these connections can be found in Ref. [Mar07].

As we proposed in Chapter 3, outgoing and incoming particles may be modeled as plane waves. In this configuration, it would not be necessary to involve any transport equation for the calculation, but instead a (most likely numerical) integration of the in-medium single-nucleon-cross section, defined in Eq. (3.5), should be directly performed. On the other hand, the study of heavy-ion collisions, which in their description strongly depend on transport phenomena, has led to the development of consistent treatments of hadronic potentials and spectral functions. It is therefor useful to review the concepts that form the basis of the GiBUU model [GiB], even though, as we are interested in inclusive cross sections only, we will make no use of the transport part of the code and mostly apply it as an initialization of a specific hadronic model and a Monte Carlo integration routine for the above equation.

5.1.1 Green's functions and Wigner transforms

Green's functions represent elementary solutions to differential equations. As an example, that is described, e.g., in Ref. [PS95], we give the electron propagator for the Dirac equation,

$$S_{\mathrm{F}}(p) = \frac{\not{p} + m}{p^2 - m^2 + \mathrm{i}\epsilon}, \tag{5.1}$$

with $\epsilon > 0$ being an arbitrary small. It is an inverse to the differential operator $(\not{p} - m)$ of the Dirac equation in momentum space. Consequently we can use a Fourier transformation to obtain the Green's function in coordinate space, $S_{\mathrm{F}}(x, y)$, which solves the Dirac equation in the following way

$$(\mathrm{i}\not{\partial}_x - m) S_{\mathrm{F}}(x, y) = \delta^4(x - y) \cdot \mathbb{1}_{4\times 4}. \tag{5.2}$$

From a physical point of view, it represents the probability for a particle to be found at x *after* being created at y. This property defines the time-ordered Green's function,

$$S_{\mathrm{F}}(x, y) = \langle 0|T\psi(x)\bar{\psi}(y)|0\rangle = \begin{cases} \langle 0|\psi(x)\bar{\psi}(y)|0\rangle & \text{for} \quad x^0 > y^0, \\ -\langle 0|\bar{\psi}(y)\psi(x)|0\rangle & \text{for} \quad x^0 < y^0, \end{cases} \tag{5.3}$$

where T is the time-ordering operator.

Let

$$\mathrm{i}g(x, y) = \langle T\psi(x)\psi^\dagger(y)\rangle, \tag{5.4}$$

now be the definition for a Green's function, $g(x, y)$, to a general dynamical equation. Following Ref. [Dan84], we can rewrite $g(x, y)$ as

$$g(x, y) = \theta(x_0 - y_0) g^>(x, y) + \theta(y_0 - x_0) g^<(x, y), \tag{5.5}$$

circumventing the time ordering through introduction of the correlation functions,

$$\mathrm{i}g^<(x, y) \equiv \pm\langle \psi^\dagger(y)\psi(x)\rangle, \tag{5.6}$$
$$\mathrm{i}g^>(x, y) \equiv \langle \psi(x)\psi^\dagger(y)\rangle, \tag{5.7}$$

where $g^<(x, y)$ ($g^>(x, y)$) offers the physical interpretation as a pure particle (hole) density. By applying a Wigner transformation,

$$\bar{g}^<(r, p) = \pm\mathrm{i} \int \mathrm{d}^4 y \exp(\mathrm{i}py) g^<(r + y/2, r - y/2), \tag{5.8}$$
$$\bar{g}^>(r, p) = \mathrm{i} \int \mathrm{d}^4 y \exp(\mathrm{i}py) g^>(r + y/2, r - y/2), \tag{5.9}$$

we are led to the quantum analogs of particle and hole phase-space densities, $\bar{g}^{\gtrless}(r, p)$, that also are referred to as correlation functions. The connection to the positive definite phase-space densities of classical mechanics can be achieved through coarse graining, as described in Ref. [Leu00]. We use the upper (lower) sign in the above and the following equations in this section to refer to bosons (fermions).

5.1.2 Phase space equations

As shown in Refs. [Kel64, LL83], one can reformulate the underlying dynamics as the time evolution of the phase-space densities, $\bar{g}^{\gtrless}(r, p)$, by means of the Kadanoff-Baym equation, without loss of dynamical information. By strong approximations such as the gradient expansion, two-body self-energies and small particle widths, one is led to the semi-classical *Boltzmann-Uehling-Uhlenbeck* (BUU) equation.

We shall first present a version that includes off-shell transport through inclusion of the retarded Green's function, g_i^{ret} (the subscript i denoting the particle species), as developed in Refs. [Leh03, Leu00]. The extended BUU equation reads

$$\left[p_0 - H_i^{\mathrm{MF}}, \bar{g}_i^{>}\right]_{\mathrm{P}} + \underbrace{\left[\mathrm{Re}(\bar{g}_i^{\mathrm{ret}}), \bar{\Sigma}_i^{<}\right]_{\mathrm{P}}}_{\mathrm{A_{off-shell}}} = \underbrace{-\bar{\Sigma}_i^{>}\bar{g}_i^{<} + \bar{\Sigma}_i^{<}\bar{g}_i^{>}}_{\mathrm{I_{coll}}}, \tag{5.10}$$

where we use the generalized Poisson brackets

$$[a,b]_{\mathrm{P}} = \frac{\partial a}{\partial p_\mu}\frac{\partial b}{\partial x^\mu} - \frac{\partial a}{\partial x_\mu}\frac{\partial b}{\partial p^\mu}. \tag{5.11}$$

The Hamiltonian, H_i^{MF}, consists of a free-particle Hamiltonian and the interaction with the mean field.

By assuming infinitesimal widths, one is led to the original BUU equation,

$$\left[\frac{\partial}{\partial t} + \frac{\partial H}{\partial \mathbf{p}}\frac{\partial}{\partial \mathbf{r}} - \frac{\partial H}{\partial \mathbf{r}}\frac{\partial}{\partial \mathbf{p}}\right] f_i(\mathbf{r},t,\mathbf{p}) = -\bar{\Sigma}_i^{>} f_i(\mathbf{r},t,\mathbf{p}) + \bar{\Sigma}_i^{<}(1 + f_i(\mathbf{r},t,\mathbf{p})), \tag{5.12}$$

for the so-called Wigner function,

$$f_i(\mathbf{r},t,\mathbf{p}) = \int \mathrm{d}\mathbf{R}\, \exp(\mathrm{i}\mathbf{p}\mathbf{R})\langle \psi^\dagger(\mathbf{r}-\mathbf{R}/2,t)\psi(\mathbf{r}+\mathbf{R}/2,t)\rangle, \tag{5.13}$$

which is an analog of the classical phase-space distribution.

One can interpret $\bar{\Sigma}^{<}$ ($\bar{\Sigma}^{>}$) as gain (loss) terms, that couple the particles to their own and other species, allowing to model, e.g., decays through a loss term or a two-body collision through both gain and loss terms. These entities are connected to the self-energy, as shown in Ref. [KB62]. Their neglect leads to the Vlasov equation,

$$[p_0 - H_i, f_i(\mathbf{r},t,\mathbf{p})]_{\mathrm{P}} = 0. \tag{5.14}$$

5.1.3 Initial conditions

The correlation functions, $\bar{g}_i^{\gtrless}(r,p)$, are not independent [KB62]. They fulfill the boundary conditions

$$\bar{g}_i^{<}(r,p) = f_i(\mathbf{r},t,\mathbf{p})\mathcal{A}_i(r,p)\bar{g}_i^{>}(r,p) = (1 \pm f_i(\mathbf{r},t,\mathbf{p}))\mathcal{A}_i(r,p), \tag{5.15}$$

where we have introduced the *spectral function*,

$$\mathcal{A}_i(r,p) = \bar{g}_i^{>}(r,p) \mp \bar{g}_i^{<}(r,p). \tag{5.16}$$

Consequently, the problem reduces to finding the seven-dimensional Wigner function, $f_i(\mathbf{r},t,\mathbf{p})$, and the eight-dimensional spectral function, $\mathcal{A}_i(r,p)$, instead of two eight-dimensional correlation functions.

In order to compute a solution for the first-order differential equation (5.10), one needs to specify initial conditions. Here, we fix the Dirichlet-type conditions $\mathcal{A}_i(\mathbf{r},t=0,p)$ and $f_i(\mathbf{r},t=0,\mathbf{p})$, which specify the phase-space density for all particle species at time $t=0$.

5.1.4 Spectral functions and self-energies

Some more words are due with regard to the spectral function, $\mathcal{A}_i(r,p)$, defined in Eq. (5.19). Contrary to the Wigner function, $f_i(\mathbf{r},t,\mathbf{p})$, it does not have a classical analog, and for a free non-relativistic particle reduces to the on-shell condition,

$$\mathcal{A}_i(r,p) \to \mathcal{A}_i(p^0,|\mathbf{p}|) = 2\pi\delta\left(p^0 - \frac{|\mathbf{p}|^2}{2m_i}\right). \tag{5.17}$$

Its meaning becomes clearer, if we revise the simple global Fermi-gas model with an isospin-independent Fermi momentum, k_F, from Sec. 3.5.2. For temperature $T=0$ one obtains the phase space-density $f_i(\mathbf{r},t,\mathbf{p}) = f_i(|\mathbf{p}|) \propto \theta(k_\mathrm{F} - |\mathbf{p}|)$, signifying that, up to the limit k_F, momenta are uniformly distributed. In such a position-independent scenario, $\mathcal{A}_i(p)$ describes the probability for a particle to be found with a certain combination of p^0 and $|\mathbf{p}|$, in this way allowing for treatment of off-shell particles. In a more general model, the probability for finding a particle in a state (r,p) is given by the product of the phase-space analog $f_i(\mathbf{r},t,\mathbf{p})$ and the spectral function, $\mathcal{A}_i(r,p)$, which describes off-shell probabilities.

Usually, the directly measurable physical input for a transport simulation is given by the interaction-cross section, σ_{ij}, that defines the collision terms, $\Sigma^{\gtrless}(r,p)$. In Ref. [Bus08] the relation between these quantities is shown explicitly. An important quantity in this context is the self-energy, $\Sigma(x,y)$, that has a direct physical interpretation through the Dyson equation,

$$g(x,y)^{\mathrm{ret}} = g^{\mathrm{ret},0}(x,y) + \int \mathrm{d}^4x'\mathrm{d}^4y' g^{\mathrm{ret},0}(x,y')\Sigma^{\mathrm{ret}}(x',y')g^{\mathrm{ret}}(x',y), \tag{5.18}$$

as the strength of the interaction of a particle with the disturbances in the surrounding system caused by its appearance, as explained in Chapter 10 of Ref. [LL83]. For non-equilibrium processes in gradient expansion, as the ones that our formalism is concerned with, in Ref. [Leu00] the following relation for the spectral function is found to hold

$$\mathcal{A}(r,p) = \frac{\Gamma(r,p)}{\left(p^0 - \frac{\mathbf{p^2}}{2m} - \mathrm{Re}\bar{\Sigma}^{\mathrm{ret}}(r,p)\right)^2 + \frac{1}{4}\Gamma(r,p)^2}, \tag{5.19}$$

where we introduce the collisional width,

$$\Gamma(r,p) = \mathrm{i}\bar{\Sigma}^{>}(r,p) - \mathrm{i}\bar{\Sigma}^{<}(r,p), \tag{5.20}$$

and the Wigner transform of the retarded self-energy, $\bar{\Sigma}^{\mathrm{ret}}(r,p)$. One can write this entity as a combination of the mean-field contribution, $\bar{\Sigma}_{\mathrm{HF}}(r,p)$, and the principal value of an integration over the collisional width [Leu00],

$$\mathrm{Re}\bar{\Sigma}^{\mathrm{ret}}(r,p) = \bar{\Sigma}_{\mathrm{HF}}(r,p) + \mathcal{P}\int \frac{\mathrm{d}k_0}{2\pi}\frac{\Gamma(\mathbf{r},k_0,\mathbf{p})}{\omega - k_0}. \tag{5.21}$$

In Fig. 5.1, we present calculations of the nucleon spectral function in nuclear matter, taken from Sec. 7.7.2 of Ref. [Lei09], for different nucleon momenta. One observes that the spectral function is peaked in the vicinity of the on-shell energy and that with increasing momenta the spectral function broadens.

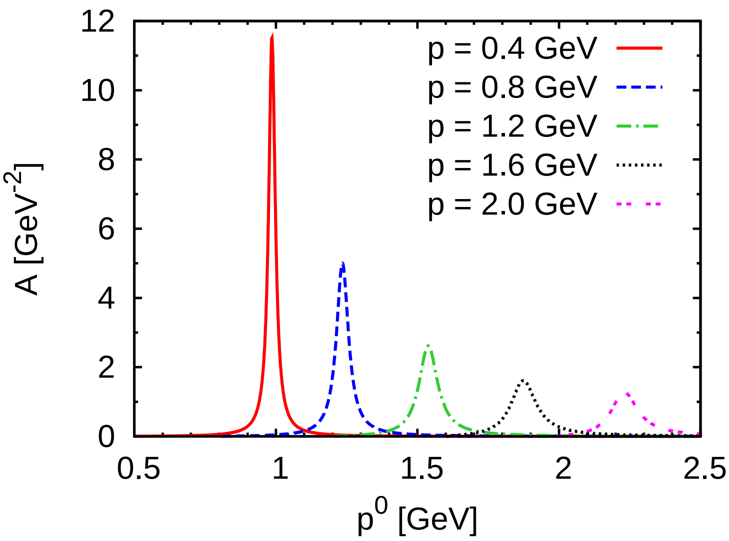

Figure 5.1: Nucleon spectral function as a function of nucleon energy for different fixed momenta indicated by linestyle. Taken from Ref. [Lei09].

5.1.5 Numerical solution: the test-particle ansatz

With the analytic solution far out of reach, the numerical approximation of the BUU equation still poses a demanding task [DPR04]. A widely used approach is the test-particle ansatz, which in addition to straight-forward implementation offers a physical interpretation. The particle-correlation function is approximated through a sum of δ functions, written as [Bus08]

$$\bar{g}^{<}(r,p) = \lim_{n(t)\to\infty} \frac{(2\pi)^4}{N} \sum_{j}^{n(t)} w_j \delta(\mathbf{r} - \mathbf{r}_j(t))\delta(\mathbf{p} - \mathbf{p}_j(t))\delta(p^0 - p_j^0(t)). \tag{5.22}$$

For a convergence towards the full correlation function, one would need infinitely many δ functions, $n(t)$, and the weights, w_j, would have to be real-valued. As a first approximation, we restrict the weights to the values -1,0,1, implying the interpretation of each contributing δ function as a test-particle (+1) or test-hole (-1). In the next step, we restrict our initial state to particles only ($\forall j \quad w_j = 1$) and fill it with $n(0) = A \times N$ particles, where A is the number of physical nucleons and N is called the *number of ensembles*, i.e., the number of test-particles per physical particle.

5.2 The GiBUU model

With the general approach described in the previous section, here, we will focus on the numerical implementation of nuclear processes in the Gießen Boltzmann-Uehling-Uhlenbeck (GiBUU) model. First, we shall present the underlying mechanisms and then compare our approach to experimental data.

5.2.1 Introduction

Starting out as a model to describe heavy-ion collisions [BBCM86, TCE+97, WLM05], the Gießen BUU code has been steadily extended and now describes scattering of electrons as well as photon-, pion-, eletron- and neutrino-induced processes [FCGM04, GF05, ECM+94, LEM00, MFM04, BLMAR07, LBMAR09]. This diversity of applications constitutes a major strength of our model, since the same physical input is constantly tested against experimental data in many different reactions.

With the test-particle approach as the basic ansatz, the recent numerical implementation is carried out in Fortran 2003, allowing for modern programming paradigms. The collaborative development of the code is handled using version control management (Subversion). From 2007 on, the GiBUU code is open source under the GPL license and can be downloaded after registration [GiB].

5.2.2 Nuclear ground state

As described in 5.1.3 we need to specify initial conditions in order to solve the BUU equation. A crucial ingredient is the phase-space density, $f(\mathbf{r}, t, \mathbf{p})$. In the case of lepton-induced scattering, it is given by the initial distributions of nucleons in the ground state of the nucleus and the particles scattered directly at the vertex of interaction with the virtual bosons. Let us now focus on the ground state, continuing the ideas developed in Sec. 3.5.2, and postpone the description of the boson-nucleon reaction to the next subsection.

We use a local Thomas-Fermi (LTF) approximation, as described in Sec. 3.5.2, for the momentum distribution. The nucleon-phase-space distribution is given by a Fermi sphere

$$f_{n,p}(\mathbf{r}, \mathbf{p}) = \Theta(k_F^{n,p}(\mathbf{r}) - |\mathbf{p}|). \tag{5.23}$$

We use

$$k_F(\mathbf{r}) = (3\pi^2 \rho(\mathbf{r}))^{1/3} \tag{5.24}$$

to relate $k_F(\mathbf{r})$ to the density distribution $\rho(\mathbf{r}) \to \rho(|\mathbf{r}|)$, which is parametrized in a harmonic oscillator form,

$$\rho_{n,p}(|\mathbf{r}|) = \rho_0 \left[1 + a_{n,p} \left(\frac{|\mathbf{r}|}{R_{n,p}} \right)^2 \right] \exp \left[- \left(\frac{|\mathbf{r}|}{R_{n,p}} \right)^2 \right], \tag{5.25}$$

for light nuclei and as a Woods-Saxon distribution,

$$\rho_{n,p}(|\mathbf{r}|) = \rho_0 \left[1 + \exp \left(\frac{|\mathbf{r}| - R_{n,p}}{a_{n,p}} \right) \right]^{-1}, \tag{5.26}$$

for heavier nuclei. The parameters are taken from Ref. [NO+93], where the proton distribution is based on the analysis in Ref. [DJDVDV74], while the neutron distribution is obtained from Hartree-Fock calculations. In the initialization routine of the code, the test particles are randomly distributed in position and momentum space, according to the probabilities $4\pi\mathbf{r}^2\rho(|\mathbf{r}|)$ and $4\pi\mathbf{p}^2 n(|\mathbf{p}|)$.

It is easy to further simplify the initialization by decoupling position and momentum initialization with the global Fermi gas (GFG) model, already presented in Sec. 4.2, where both momentum and density distributions reduce to simple spheres of radius k_{F} and R, respectively. In that case, the phase-space distribution reduces to

$$f_{n,p}^{\mathrm{GFG}}(\mathbf{r},\mathbf{p}) = N\Theta(R-|\mathbf{r}|)\Theta(k_{\mathrm{F}}^{n,p}-|\mathbf{p}|), \tag{5.27}$$

with the normalization constant, N, determined by Eq. 3.10.

5.2.3 Hadronic potential

As the presented implementation of the Fermi gas only restricts the momentum distribution, it is still possible to adjust the nucleon energy by introducing a hadronic potential to account for binding effects. The nucleon-mean-field potential is expressed, following an ansatz be Welke et al. [WPK+88], as a sum of a Skyrme contribution depending on the density and a momentum-dependent term, reading

$$V_N(\mathbf{r},\mathbf{p}) = a\frac{\rho(\mathbf{r})}{\rho_0} + b\left(\frac{\rho(\mathbf{r})}{\rho_0}\right)^{\tau} + \frac{2c}{\rho_0}g\int\frac{\mathrm{d}^3\mathbf{p}'}{(2\pi)^3}\frac{f(\mathbf{r},\mathbf{p}')}{1+\left(\frac{\mathbf{p}'-\mathbf{p}}{\Lambda}\right)^2}. \tag{5.28}$$

While the constant for the nucleon degeneracy, $g = 2$, is fixed, the other parameters must be obtained by a fit procedure. By assuming a nuclear-matter-saturation density of $\rho_0 = 0.168\ \mathrm{fm}^{-3}$ and a binding energy of 16 MeV, Teis [Tei97, TCE+97] has obtained five distinct standard parameter sets. In this work the parameterization referred to as "EQS 5" will be used, implying $a = -29.3$ MeV, $b = 57.2$ MeV, $c = -63.3$ MeV, $\tau = -63.3$ MeV, $\Lambda = 2.13$ 1/fm.

Starting from the relativistic Hamiltonian,

$$H = \sqrt{M_N^2+\mathbf{p}^2} + V_N(\mathbf{r},\mathbf{p}), \tag{5.29}$$

it is useful to introduce the scalar potential

$$U_N(\mathbf{r},\mathbf{p}) = \sqrt{\left(\sqrt{M_N^2+\mathbf{p}^2}+V_N(\mathbf{r},\mathbf{p})\right)^2-\mathbf{p}^2} - M_N, \tag{5.30}$$

leading to the new expression

$$H = \sqrt{\left[M_N+U_N(\mathbf{r},\mathbf{p})\right]^2+\mathbf{p}^2}. \tag{5.31}$$

On can thus identify

$$M = \sqrt{p^2} = M_N + U_N(\mathbf{r},\mathbf{p}) \tag{5.32}$$

as an effective mass of an in-medium nucleon. This will be of importance for computing the in-medium cross sections in the next subsection.

5.2.4 Lepton-nucleus cross sections

As for the single-nucleon case we suppose the nuclear cross section to be given as an incoherent sum of medium modified single-nucleon contributions,

$$\mathrm{d}\sigma_{\mathrm{tot}}^{\mathrm{med}} = \mathrm{d}\sigma_{\mathrm{QE}}^{\mathrm{med}} + \sum_{\mathrm{R}}\mathrm{d}\sigma_{\mathrm{R}}^{\mathrm{med}} + \mathrm{d}\sigma_{\mathrm{BG}}^{\mathrm{med}}. \tag{5.33}$$

Next we will present how the in-medium modifications are modeled for the different contributions.

Quasielastic scattering

In Appendix B.2.1 of Ref. [Lei09], the in-medium cross section is derived to be

$$\frac{\mathrm{d}\sigma_{\mathrm{QE}}^{\mathrm{med}}}{\mathrm{d}k'^0 \mathrm{d}\Omega_{k'}} = \frac{|\mathbf{k}'|}{32\pi^2} \left[(k \cdot p)^2 - m_l^2 M^2\right]^{-1/2} \mathcal{A}_N(p', r) \overline{|M_{\mathrm{QE}}^{\mathrm{med}}|^2}. \tag{5.34}$$

Note, that the outgoing nucleon is also subject to the hadronic potential, resulting in an effective mass, M', which may differ from the effective mass of the incoming nucleon, M, due to the momentum dependence of the potential. While the spectral function can be consistently obtained from the GiBUU model by evaluation of Eq. (5.19), the correct treatment of the matrix element for in-medium scattering leads to form factors depending not only on $q_\mu q^\mu$, but on all Lorentz scalars. As the available data do not allow to fix such intricate dependencies, we assume $\overline{|M_{\mathrm{QE}}^{\mathrm{med}}|^2}$ to be determined by the single-nucleon hadronic tensor from Sec. 2.3.1, but calculated with the medium-modified p and p'.

Resonance excitations

For resonance excitations the cross section is modeled in a similar fashion, taking the expression

$$\frac{\mathrm{d}\sigma_{\mathrm{QE}}^{\mathrm{R}}}{\mathrm{d}k'^0 \mathrm{d}\Omega_{k'}} = \frac{|\mathbf{k}'|}{32\pi^2} \left[(k \cdot p)^2 - m_l^2 M^2\right]^{-1/2} \mathcal{A}_R(p', r) \overline{|M_{\mathrm{R}}^{\mathrm{med}}|^2} \tag{5.35}$$

and repeating the steps described for QE scattering, with the single-nucleon hadronic tensor from Sec. 2.4.

Non-resonant single-pion background

The situation differs for non-resonant single-pion background, since we have defined it in Sec. 2.5 as the difference between the expected resonant-pion-production cross section and the observed data for *vacuum*-pion production. Hence, it is advisable to compute this contribution with vacuum kinematics, i.e., $p = (\sqrt{M_N^2 + \mathbf{p}^2}, \mathbf{p})$ for a given $\mathbf{p}$, as

$$\mathrm{d}\sigma_{\mathrm{BG}}^{\mathrm{med}}(p, q^\mu) = \mathrm{d}\sigma_{\mathrm{BG}}^{\mathrm{vac}}(p_{\mathrm{vac}}, q^\mu). \tag{5.36}$$

Response of the Fermi gas

Now that $\mathrm{d}\sigma_{\mathrm{tot}}^{\mathrm{med}}$ is determined, the inclusive nuclear cross section can be written as the sum of the contributions from all nucleons. As in our model the nucleons are distributed in a (local Thomas-)Fermi gas, an integration over the initial-state-phase space has to be performed in the following way

$$\mathrm{d}\sigma_{\mathrm{tot}}^{lA\to l'X} = \sum_{N=n,p} \int \mathrm{d}^3\mathbf{r} \int \frac{\mathrm{d}^3\mathbf{p}}{(2\pi)^3} f(\mathbf{r}, \mathbf{p}) f_{\mathrm{corr}} \mathrm{d}\sigma_{\mathrm{tot},N}^{\mathrm{med}} P_{\mathrm{PB}}(\mathbf{r}, \mathbf{p}). \tag{5.37}$$

Here, $f(\mathbf{r}, \mathbf{p})$ must be taken from Eq. (5.27) or (5.23) respectively and the factor $P_{\mathrm{PB}}(\mathbf{r}, \mathbf{p})$ ensures Pauli-blocking. An additional factor,

$$f_{\mathrm{corr}} = \frac{|v_N - v_l|}{|v_A - v_l|} = \frac{k \cdot p}{k^0 p^0} \frac{1}{|v_A - v_l|} \underbrace{\approx}_{v_A \approx 0, v_l \approx 1} = \frac{k \cdot p}{k^0 p^0} \tag{5.38}$$

enters to correct for the different fluxes (cf. Sec. 5.4 of Ref. [Bus08]).

Numerical implementation

The integration in Eq. (5.37) is carried out in a Monte Carlo sampling method. Let us briefly walk through the steps involved in the implementation of the GiBUU code, following the explanation in Sec. 5.5 of Ref. [Bus08].

1. At first, the properties of the virtual photon are defined as input to the code. These specifications are written to so called job cards, where also parameters concerning the target and simulation are stored. When total cross sections instead of double-differential ones are desired, the code will sample through different virtual photons and perform a numerical integration based on these values.

2. During the initialization of the scattering reaction, a specific nucleon is chosen in a random (Monte Carlo) decision, according to spatial and momentum distributions discussed above. Since the kinematics of only this nucleon will determine the cross section, this step has to be repeated many times to achieve convergence.

3. With the kinematics fixed by the chosen nucleon, the cross sections for all channels are computed according to Eqs. (5.34), (5.35) and (5.36) and then summed.

5.2.5 Model validation: Comparison with electron data

As electron scattering on nuclei has been studied in detail in the past 60 years, there is sufficient data available for comparison. Any theory aiming to describe neutrino-nucleus interactions should be able to describe the electron data. In Fig. 5.2 we present the comparison of GiBUU calculations to data obtained in $(e^{16}\mathrm{O}, e'X)$ reactions. As one can see, for high Q^2 the agreement is reasonably good, while at low Q^2, both an excess strength and a shift of the peak in the ω-region associated with QE scattering become visible. The study of these effects will be a major topic in the following chapter.

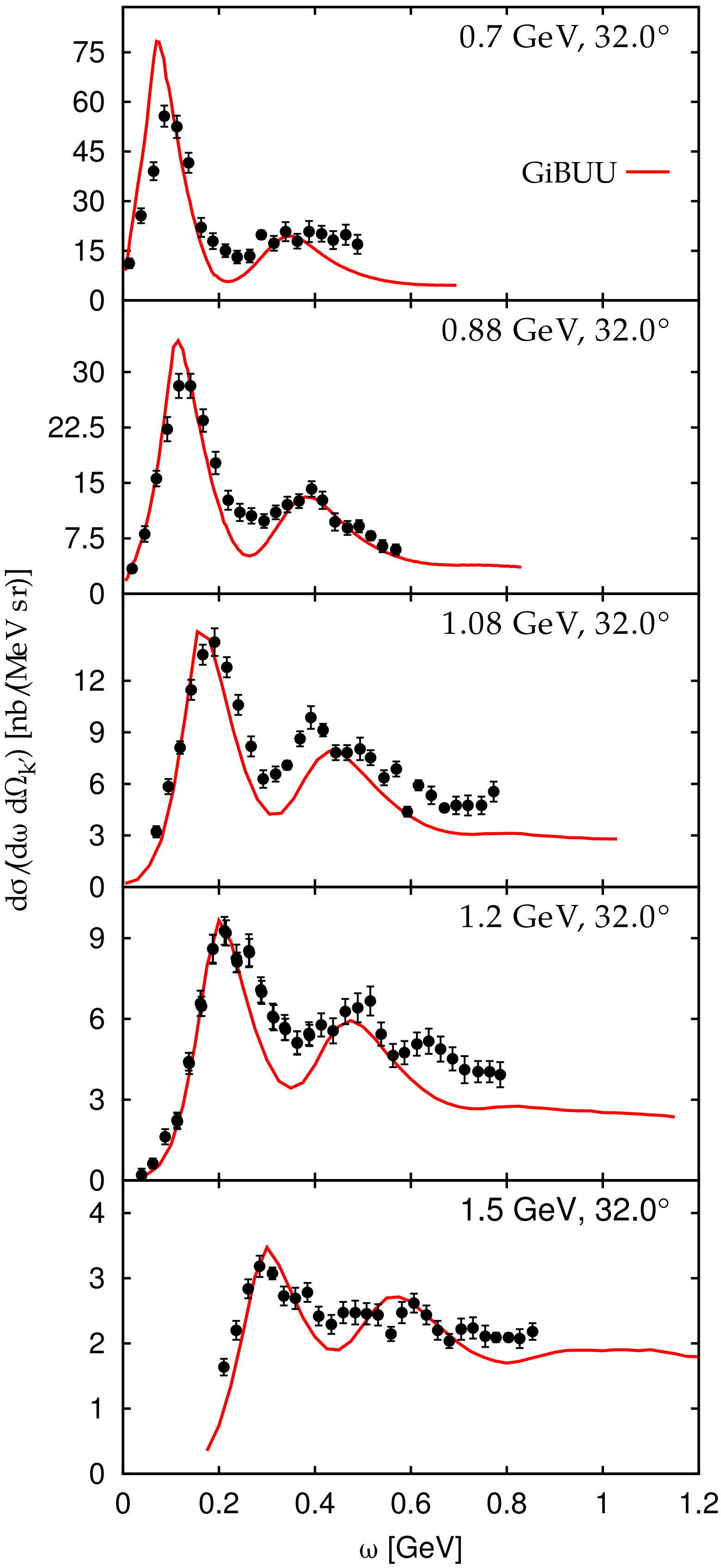

Figure 5.2: Comparison of GiBUU-calculated double-differential cross sections with data for inclusive electron scattering on ^{16}O from Refs. [ARC+95, A+96]. The scattering angles and the incoming energies are specified in the panels. Plot taken from Ref. [LBARM09].

Chapter 6

Applications, predictions and comparisons

Throughout this chapter, we apply the superscaling analysis, described in Chapter 4, to our hadronic model. We study different effects included in our model and compare our results to experimental data and other theoretical approaches. More light is shed on the connection to the analysis of the transverse and longitudinal response and the role of the ground state. Finally, we shall discuss some possible implications for neutrino-scattering experiments.

6.1 Superscaling analysis

6.1.1 Superscaling analysis of electron scattering simulations

As discussed in Sec. 4.4, experimental inclusive electron-nucleus-scattering-cross sections exhibit two distinct kinds of scaling. Here, scaling signifies that the responses can be reduced to a product of single-nucleon contributions and a scaling function, depending mostly on one single kinematic variable ψ' and representing nuclear dynamics. When first-kind scaling is fulfilled scaling functions for different *kinematics* coincide, for second-kind scaling the scaling functions for different *targets* are identical. When both kinds of scaling apply, one speaks of superscaling. Naturally, we begin by investigating whether our model fulfills these requirements. In the following plots we show the dimensionless scaling function[1], f, plotted versus the shifted RFG scaling variable[2], ψ'. The calculations include all contributions described in Sec. 5.2, while the role of the different effects will be studied at a later point of this section.

First-kind scaling

Whereas in Fig. 6.1a the scaling functions of electron scattering on ^{12}C for a fixed momentum transfer, $q = 0.5$ GeV, show some sensitivity on incoming energy, the GiBUU curves in Fig. 6.1b exhibit perfect scaling. This is expected, since in our description of

[1]Given in Eq. (4.57).

[2]Given in Eq. (4.55) as the shifted analog of Eq. (4.36).

this kinematical region the only energy dependent contribution[3] to the cross section is the single-nucleon cross section, which is divided out in the scaling approach. As the functional form of the kinematical dependency changes for the resonance excitation cross section, i.e., the masses in the energy conservation conditions change leading to differing initial-state-phase spaces, our model exhibits scaling violations in the region of $\psi' > 1$.

The direct comparison to data, depicted in Fig. 6.1c, shows an effect already expected from the comparison to electron-scattering data in Sec. 5.2.5. Let us compare our model to the 2 GeV data (plus symbol), which due to the smallest transverse component, are expected to include the smallest amount of additional scaling-violating effects, as will be explained in Sec. 6.2.5. We find that the QEP, expected at $\psi' = 0$, is shifted to smaller ψ' (smaller energy transfers), narrowed and increased in size. We consider this to be an effect of the ground-state initialization and will come back to this issue in Sec. 6.3.

An additional effect is found, when comparing the scaling function for different momentum transfers, q, in Fig. 6.2b. The difference in the region of $\psi' > 0$ has already been ascribed to different kinematics for resonance excitations. The newly found effect consists in the shift and lowering of the scaling function for kinematics with $q_{\mathrm{QEP}} \approx 0.32$ GeV at the QEP. Note that the explicit formula for $q_{\mathrm{QEP,vac}}$ is given in Appendix D.2.

The shift is a simple consequence of the LTF model reproducing the QEP at the position for vacuum kinematics, $\omega_{\mathrm{QEP}} = \sqrt{q^2 + M_N^2} - M_N$, as will be discussed in Sec. 6.3. For the superscaling analysis we apply a fixed binding energy, $E_{\mathrm{shift}} = 0.02$ GeV, in Eqs. (4.54) and (4.55) to correct for the experimentally found shift. This implies that with lower q the ratio $E_{\mathrm{shift}}/\omega_{\mathrm{QEP}}$ is growing. Looking at the shifted non-relativistic analog of ψ, given as $y' = [2M_N(\omega - E_{\mathrm{shift}}) - q^2]/2q$, for vacuum non-relativistic QEP kinematics $\omega_{\mathrm{QEP,nr}} = q^2/2M_N$, one finds that the y value at vacuum QEP kinematics, $y'(\omega = \omega_{\mathrm{QEP,nr}}) = -M_N E_{\mathrm{shift}}/2q$ of y, increases in absolute size as $q \to 0$. A similar relation for ψ' is derived in Appendix D.3.

The reduced size of the peak for $q = 0.32$ GeV can be explained if we relate back to Fig. 4.10, where we show that for $k_{\mathrm{F}} < q < 2k_{\mathrm{F}} \approx 0.5$ GeV, Pauli-blocking reduces the final state-phase space (strength of the response) for $\psi' < 0$. Looking at the data in Fig. 6.2a and Fig. 6.10a, we find that this effect, namely a slight lowering of the scaling function for $q < 2k_{\mathrm{F}}$, is also observed in experiments.

Second-kind scaling

For scattering on different nuclei, we discover quite the opposite behavior. Whereas now the experimental data in Fig. 6.3a show perfect scaling in the region of $\psi' < 0$, scaling-violating effects already set in at $\psi' > -0.5$ for the GiBUU calculations in Fig. 6.3b. We explain this effect with the qualitatively different shape of density profiles for light and heavy nuclei, described in Sec. 5.2.2, and take it as an indication that the LTF approach results in a coupling of momentum and density distributions that is stronger than the one suggested by experimental data. This issue will be discussed in Sec. 6.3.

It is interesting to compare the scaling functions of the two isotopes differing the most, i.e. , ^{12}C, a nucleus for which a successful description as a Fermi gas comes as a surprise, and ^{197}Au, which is believed to already exhibit some properties of uniformly distributed infinite nuclear matter. When comparing to data, cf. Fig. 6.3c, we see that

[3]Note that Pauli-blocking would also play role for $q < 2k_{\mathrm{F}}$.

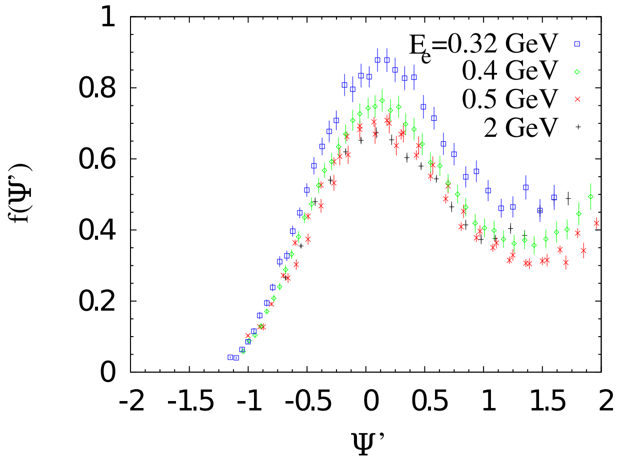

(a) Experimental scaling functions, with data taken from the world data analysis in Ref. [DS99].

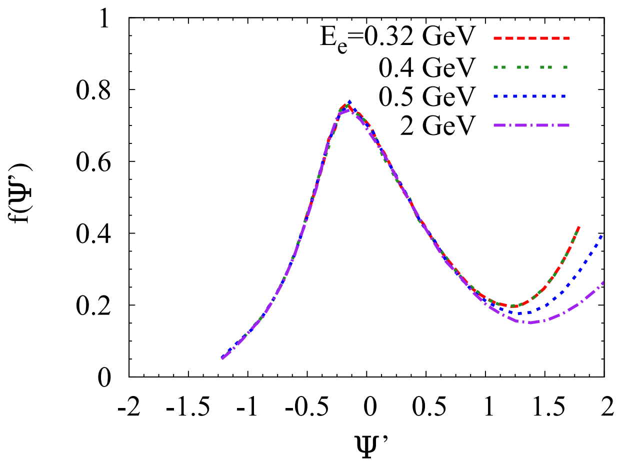

(b) GiBUU simulation of scaling functions.

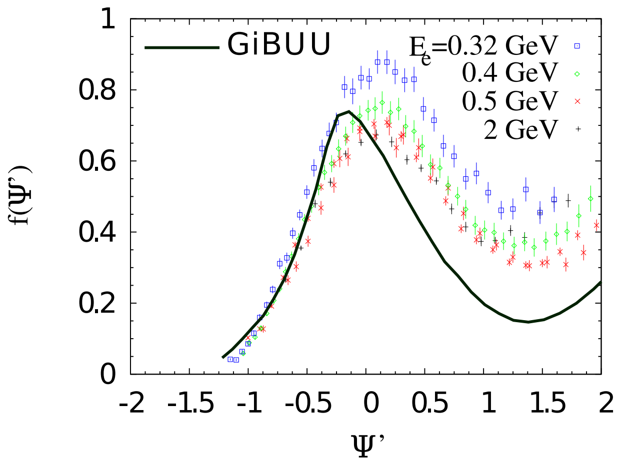

(c) Comparison of data in Fig. (a) with the GiBUU simulated scaling function for 2 GeV scattering from Fig. (b) (solid line).

Figure 6.1: First-kind scaling analysis of electron scattering on ^{12}C at a constant momentum transfer of q=0.5 GeV and incoming energies between 0.32 and 2 GeV, specified by colors and different line shapes/symbols in the plots.

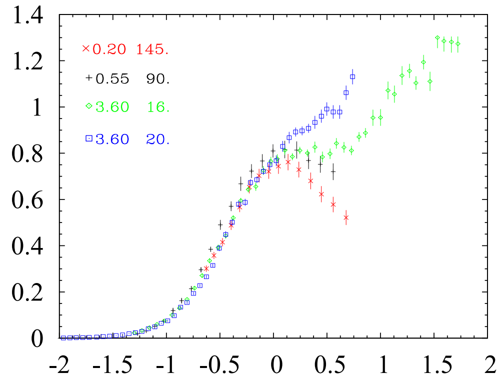

(a) Experimental scaling functions, with data taken from the world data analysis in Ref. [DS99]. The incoming lepton energy in GeV (left column) and scattering angle (right column) are specified in the plot.

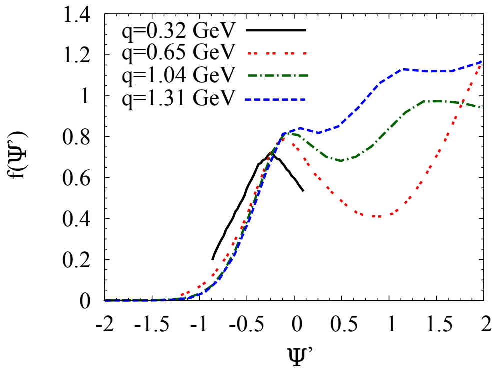

(b) GiBUU simulation of scaling functions for incoming energies as given in (a), with the corresponding curves arranged in the same order. Fixed momentum transfers, $q \approx q_{\mathrm{QEP}}$ for the kinematics in Fig. (a), were used and are specified in the plot.

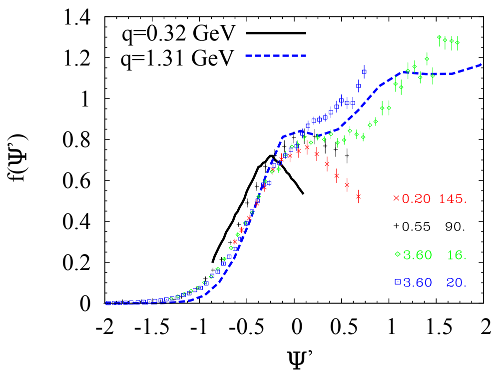

(c) Comparison of data in Fig. (a) with the GiBUU simulated scaling function for scattering at $q = 0.32$ GeV (solid line) and $q = 1.31$ GeV (dashed line) from Fig. (b).

Figure 6.2: First-kind scaling analysis of GiBUU simulated electron scattering on ^{12}C at momentum transfers ranging from q=0.3 GeV to q=1.31 GeV. Note, that the curve for $E = 0.2$ GeV does not span the entire range of ψ' due to kinematical restrictions.

the problems of a narrowed and shifted peak, described above, become evident for ^{12}C, while for ^{197}Au we see a general lack of strength. This is again an implication that the ground-state-initialization constitutes a key issue. It will be discussed in Sec. 6.3.

We can thus summarize that our model exhibits reasonable scaling behaviour. As shown in Figs. 6.1c and 6.3c, our scaling functions also show satisfactory agreement with experimental data. This result is a validation of both, the predictive power and the correct numerical implementation of our model.

6.1.2 Impact of different parameters on the scaling function

Since the scaling function contains all "nuclear" information, it is interesting to investigate the impact of different parameters of our nuclear model on this function. As ground-state initialization plays a key role, we will later discuss this issue in more detail and for now use the LTF model, introduced in Sec. 5.2.2, to evaluate the influence of the other parameters. Since, by construction, only second-kind scaling is broken, we study the four different nuclei already presented in Fig. 6.3.

Hadronic potential

Using a momentum-dependent hadronic potential, as the Welke-type potential discussed in Sec. 5.2, is expected to have a noticeable impact on the QE cross section since the nucleon is subject to different conditions before and after being struck. In Fig. 6.4, we find that the inclusion of the hadronic potential takes strength out of the region around and below the QEP and shifts it into the region above the QEP, much more in accordance with data. However, the QEP itself remains at its initial position. This is unsatisfactory from a conceptual point of view, since the hadronic potential is our only way to model binding effects and thus correct the position of the QEP. These findings were already studied and explained in Refs. [Bus08, LBARM09]: As the LTF correlates low momentum nucleons, which dominate the QE scattering as shown in Sec. 4.3, with areas of low densities, which are subject to the least medium modifications, the region around the QEP is affected the least by a hadronic potential.

Recognizing that the lack of shift is a shortcoming of the LTF approach, we conclude that the inclusion of a hadronic potential is important in order to obtain the shape of the experimental scaling function. This is accomplished by a lowering of the scaling function at and below the QEP and an increase of the scaling function in the region of large ψ'. A possibility to account for the shift while keeping the merits of a hadronic potential in the LTF picture would be the inclusion of a phenomenological energy shift in the GiBUU model. We investigate this possibility towards the end of Sec. 6.3.

In-medium widths

In addition, we have included the effect of in-medium widths, since they allow for a more realistic momentum distribution[4]. In Fig. 6.5, we compare calculations including in-medium widths with calculations that do not include them and find that inclusion of in-medium widths substantially lowers the scaling function at the position of the QEP. It

[4] While, through the use of tabulated spectral functions, consuming large amounts of memory.

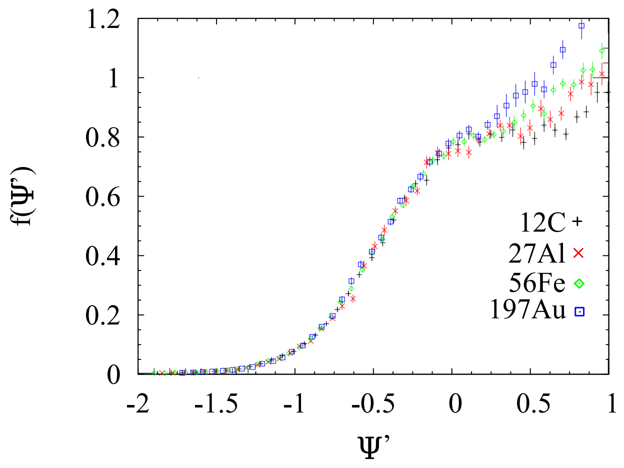

(a) Experimental scaling functions, with data taken from the world data analysis in Ref. [DS99].

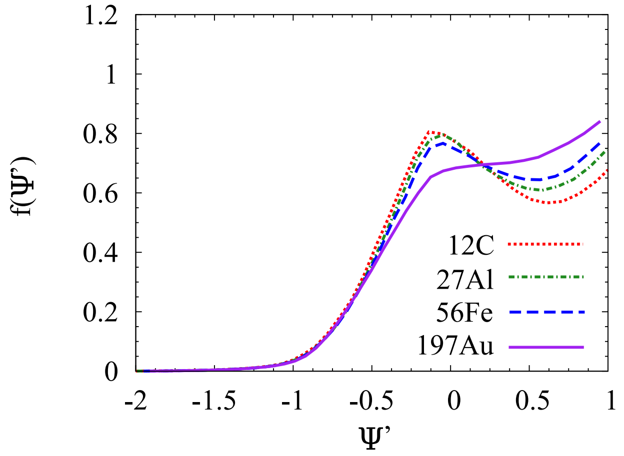

(b) GiBUU simulation of scaling functions.

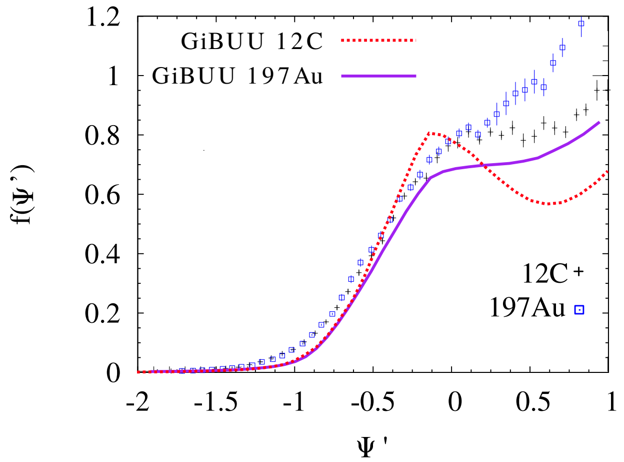

(c) Comparison of data in Fig. (a) with the GiBUU scaling function for carbon (dotted line) and gold (solid line) from Fig. (b).

Figure 6.3: Second-kind scaling analysis of electron scattering on ^{12}C, ^{27}Al, ^{56}Fe and ^{197}Au at a constant momentum transfer of q=1 GeV and incoming electron energy of 3.6 GeV.

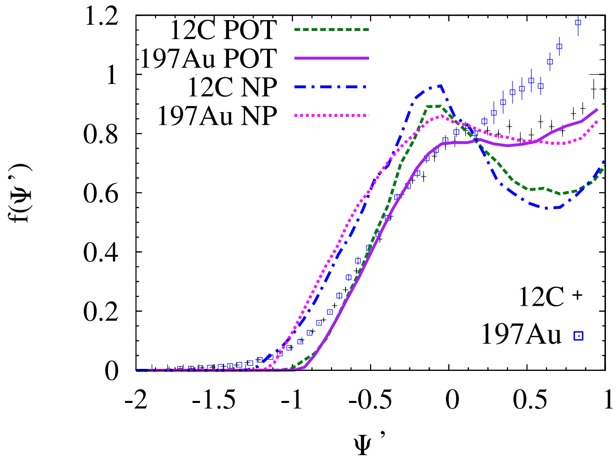

Figure 6.4: Scaling function of GiBUU simulations at a constant momentum transfer of q=1 GeV and incoming electron energy of 3.6 GeV including a potential (dashed and solid line) and those including no potential (dash-dotted and dotted line) compared to experimental data from Ref. [DS99]. Both calculations do not include in-medium widths.

is also noteworthy, that without in-medium widths the scaling function directly vanishes beneath a certain value of ψ', whereas in case of their inclusion it vanishes asymptotically, much more in accord with the experimental data. We explain this effect with the spectral functions' strength on the *high-momentum* side, cf. Fig. 5.1, allowing for larger parallel momenta to be found within the nucleus. Hence, we find that the inclusion of in-medium widths improves the scaling function both quantitatively and qualitatively.

Inclusion of resonance excitations and non-resonant single-pion background

As resonance excitations and the single-π background dominate the response right above the QEP, we have also studied their impact on the scaling function. In Fig. 6.6, one can see that they play no role beneath the QEP. In the region of $\psi' > 0$ they cause violations of scaling, as can be seen in Fig. 6.1b. In any case, the study of their impact offers no insight into the momentum distribution when performed with the superscaling formalism for QE scattering, since the difference in kinematics mixes single-nucleon contributions into the scaling function at $\psi' > 0$.

Some more words are due concerning fact that the full GiBUU prediction (solid line) does not match the curve for $\psi' > 0$ in Fig. 6.1b. As one can see the QE scaling function is decreasing in that kinematical region, hence non-QE effects should fill the gap. We see the large difference as a clear indication that important effects are missing in our implementation and identify them as the excess transverse strength that will be discussed in Sec. 6.2.

6.1.3 Superscaling of the neutrino response

In Sec. 4.6 we already pointed out that the neutrino-scattering response can be analyzed using a similar superscaling method, i.e., by dividing out single-nucleon contributions. While the approach of Amaro *et al.* [ABC+05] consists of using a scaling function obtained

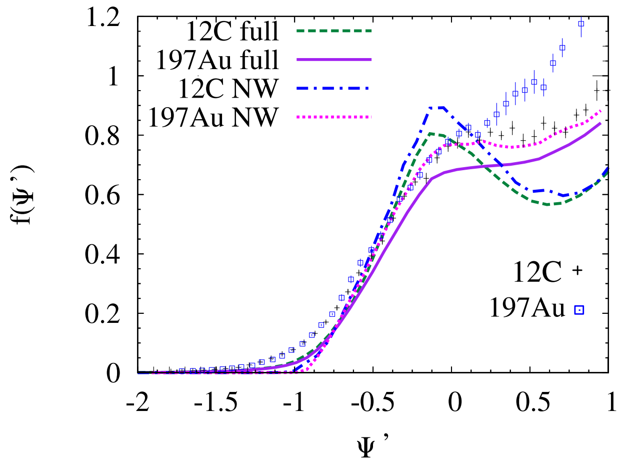

Figure 6.5: Scaling function of full GiBUU simulations at a constant momentum transfer of q=1 GeV and incoming electron energy of 3.6 GeV including in-medium widths (dashed and solid line) and those including no widths (dash-dotted and dotted line) compared to experimental data from Ref. [DS99].

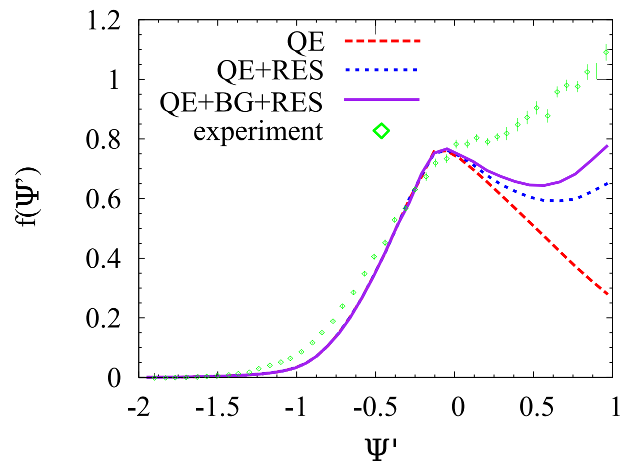

Figure 6.6: Study of contributions from resonance excitations and single-pion non-resonant background for electron scattering on ^{56}Fe at a constant momentum transfer of q=1.0 GeV and incoming electron energy of 3.6 GeV. Data taken from the world-data analysis in Ref. [DS99].

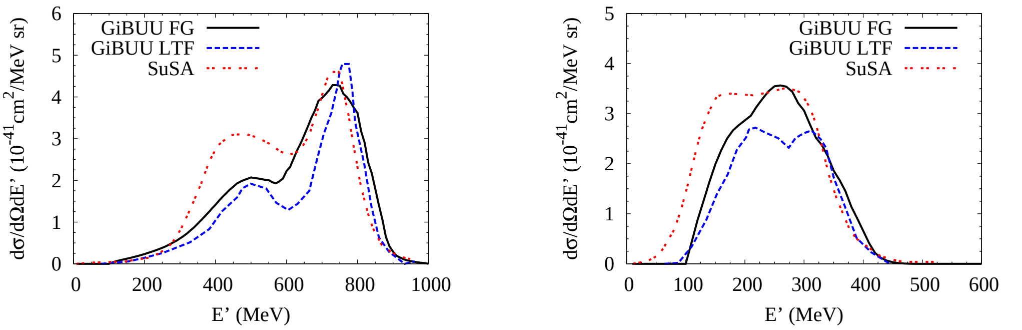

(a) Cross section for $\nu_\mu{}^{12}\mathrm{C} \to \mu X$ scattering with $E = 1$ GeV incoming neutrino energy and $\theta = 45°$.

(b) Cross section for $\nu_\mu{}^{12}\mathrm{C} \to \mu X$ scattering with $E = 1$ GeV incoming neutrino energy and $\theta = 180°$.

Figure 6.7: Comparison of double-differential cross section obtained from superscaling analysis in Ref. [ABC⁺05] (dotted lines) and GiBUU calculations with LTF (dashed lines) and global Fermi-Gas (solid lines) ground states.

from electron scattering to predict neutrino-cross sections, our model directly predicts the neutrino response from the same nuclear input as for electron scattering. In Fig. 6.7 we compare our results to the ones of Amaro and find reasonable agreement with the simple Fermi-gas simulations while generally lower responses with the LTF approach.

Furthermore, we can directly analyze the scaling function of the neutrino response and compare it to those obtained from electron simulations. We start by checking for second-kind scaling, cf. Fig. 6.8a, and find a situation that looks very similar to that of electron scattering in Fig. 6.3b. Comparing electron and neutrino scaling functions in Fig. 6.8b, we see that they are almost identical up to the QEP. Naturally the kinematics of non-scaling contributions differ for the two different currents, and above the QEP the scaling functions diverge.

Checking for first-kind scaling in Fig. 6.9a, we find that, contrary to the electron case, scaling is to some degree violated. We observe that the QEP is shifted towards lower ψ' for lower energies. We also find that these violations lead to larger neutrino-scaling functions at low energies and lower scaling functions at larger energies, when compared to perfectly scaling electron results. A possible explanation is that in Eq. (4.79) and the following we have used a first order expansion in k_F/M_N, and, e.g., have approximated the longitudinal contribution as $G_L(\kappa,\lambda) = \kappa/2 \times X_L^{VV} = \kappa/(2\rho) \times G_E^2$, while the appropriate expression is given in Eq. (4.58). However we do not further investigate this aspect here. We also do not present the neutrino-scattering analog of Fig. 6.2 as those curves exhibit deviations from the electron response of a similar shape and magnitude as seen in Fig. 6.9a. We conclude that besides differences on a level below 10% the GiBUU scaling function for neutrino scattering resembles the shape and size of the scaling function for electron scattering. We consider this finding a proof that the same nuclear dynamics is reproduced.

Furthermore, we have undertaken a superscaling analysis using the PWIA approach described in Sec. 4.3 in Appendix C.2 and also have implemented a superscaling analysis of the Δ-peak following Ref. [MDS02] in Appendix C.3. Both analyses underline the statement that the GiBUU simulated response does superscale. Nevertheless we choose

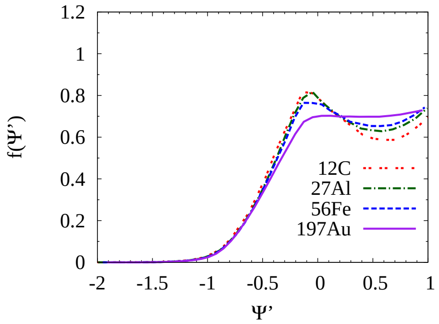

(a) Scaling function of the neutrino response for different nuclei.

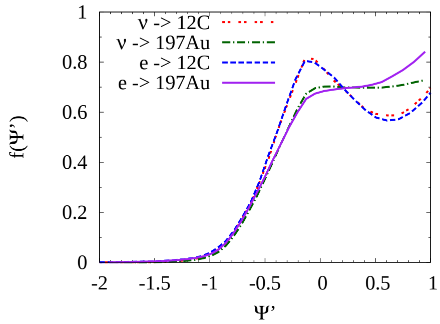

(b) Scaling function of the neutrino response (dotted and dash-dotted line) compared to scaling function of electron response (dashed and solid line) for C and Au.

Figure 6.8: Second-kind scaling analysis of electron and muon-neutrino scattering on ^{12}C, ^{27}Al, ^{56}Fe and ^{197}Au, at a constant momentum transfer of q=1 GeV and incoming electron energy of 3.6 GeV.

to treat them in the appendix, as their discussion would divert from the analysis of the response at the QEP.

6.2 Analysis of the longitudinal and the transverse response

In Sec. 4.4 we have already mentioned, that, after contracting leptonic and hadronic tensors, the double-differential QE cross section reads

$$\frac{\mathrm{d}^2\sigma}{\mathrm{d}E'\mathrm{d}\Omega} = \left(\frac{\mathrm{d}\sigma}{\mathrm{d}\Omega}\right)_{\mathrm{Mott}} \left[\left(\frac{Q^2}{q^2}\right)^2 R_{\mathrm{L}}(q,\omega) + \left(\frac{1}{2}\frac{Q^2}{q^2} + \tan^2\frac{\theta}{2}\right) R_{\mathrm{T}}(q,\omega)\right], \tag{6.1}$$

with $(\mathrm{d}\sigma/\mathrm{d}\Omega)_{\mathrm{Mott}}$ defined in Eq. 4.2. By dividing out kinematical factors one obtains the following equation

$$\Sigma \equiv \frac{\mathrm{d}\sigma}{\mathrm{d}\Omega\mathrm{d}\omega}\frac{\epsilon}{\left(\frac{\mathrm{d}\sigma}{\mathrm{d}\Omega}\right)_{\mathrm{Mott}}}\frac{q^4}{Q^4} = \epsilon R_{\mathrm{L}}(q,\omega) + \frac{q^2}{2Q^2}R_{\mathrm{T}}(q,\omega), \tag{6.2}$$

which, for the case of fixed q and Q^2, expresses the reduced response, Σ, as a linear function of the virtual-photon polarization,

$$\epsilon = \left(1 + \frac{2q^2}{Q^2}\tan^2\frac{\theta}{2}\right)^{-1}. \tag{6.3}$$

In the spirit of the Rosenbluth separation, cf., e.g., Ref. [PRSZ09], it is thus possible to obtain R_{L} as the slope of Σ and R_{T} as the intercept at $\epsilon = 0$.

In practice, however, the separation is complicated by the lack of data. On one hand, it is evidently desirable to include a large range of ϵ into the analysis. On the other

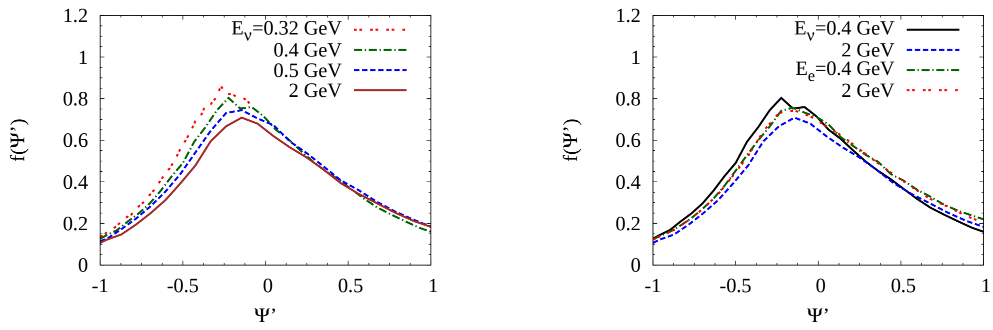

(a) Scaling function of the neutrino response for different nuclei. Note, that due to the non-negligible outgoing lepton mass the range of ψ is limited for lower E_ν.

(b) Scaling function of the neutrino response (solid and dashed line) compared to scaling function of electron response (dash-dotted and dotted line) for incoming lepton energies of $E = 0.4$ GeV and $E = 2$ GeV.

Figure 6.9: First-kind scaling analysis of electron and muon-neutrino scattering on ^{12}C at a constant momentum transfer of q=0.5 GeV and incoming energies between 0.32 and 2 GeV, specified by colors and different line shapes/symbols in the plots.

hand, one has to keep q and Q^2 fixed, or at least not too different, so that interpolation techniques can be applied. These complications have led to different interpretations of the data sets throughout the past (cf., e.g., Ref. [Jou96], where it is argued that past analyses suffered from systematic errors and a too narrow kinematical range). As R_{L} and R_{T} give insight into the properties of the hadronic current, the measurement and prediction of these response functions has been the subject of many studies, some of which are described in Sec. 6.2.5.

6.2.1 Experimental status of the separated responses

Since the non-relativistic Fermi gas, described in Ref. 4.2, has been used as a means for predicting the QE response [MSW$^+$71], the formalism has been extended to the relativistic Fermi gas and compared with different data sets. Unfortunately, the first analyses, e.g., Ref. [ACD$^+$80], included data sets which due to systematical errors or to their limited kinematic regions favored an overestimation of the transverse response with regard to the longitudinal response [Jou96, W$^+$97, DS99, BDS08]. Consequently, it has been long believed that R_{T} is in good agreement with Fermi gas calculations while the quenching of R_{L} poses a puzzle, cf., e.g., Sec. 5.5 of [BGPR96].

This assumed discrepancy has led to an intense study of the Coulomb sum rule (CSR),

$$S_{\mathrm{L}}(q) = \frac{1}{Z}\int_{\omega^+}^{\infty} \mathrm{d}\omega \frac{R_{\mathrm{L}}(\omega, Q^2)}{\tilde{G}_{\mathrm{E}}^2(Q^2)}, \tag{6.4}$$

with ω^+ denoting the minimal energy transfer needed for nucleon knock-out and $\tilde{G}_{\mathrm{E}}^2 = (G_{ep}^2 + G_{en}^2 N/Z)$. In a non-relativistic derivation, described, e.g., in Ref. [BGPR96], it is shown to converge towards 1 for $q \to \infty$. Early work [CG63] suggested to use the CSR as a tool for the study of short-range correlations between the nucleons. Certain experiments, suffering from shortcomings mentioned above, found deviations from the CSR that exceeded 50%.

The world-data analysis by Jourdan [Jou96] and a reanalysis by Morgenstern and Meziani [MM01] show much smaller violations of the CSR and prove the importance of taking Coulomb corrections into account. At the same time the analyses by Jourdan and Williamson [Jou96, W$^+$97] find larger values for R_L and smaller values for R_T.

6.2.2 Superscaling of separated responses

Describing the QE response with a relativistic Fermi gas leads to identical information contained in both, R_L and R_T, since they can be reduced to the same scaling function via[5]

$$f_\mathrm{L} \equiv k_\mathrm{F}\frac{R_\mathrm{L}}{G_\mathrm{L}} \stackrel{!}{=} f^\mathrm{RFG} \stackrel{!}{=} k_\mathrm{F}\frac{R_\mathrm{T}}{G_\mathrm{T}} \equiv f_\mathrm{T}. \tag{6.6}$$

Analyses by Finn *et al.* [FLC84] and Williamson *et al.* [W$^+$97] indicate that first-kind scaling holds for R_L while it is violated for R_T, yielding an *excess in the transverse response*. This finding is in contrast to the early results discussed in the previous subsection and is attributed to meson-exchange currents (MEC) and other non-impulsive effects playing a more important role in the transverse channel.

In Fig. 6.10 we bring an example of the separated scaling functions for different energies, originating from Ref. [DS99] and based on data in Ref. [Jou96]. It is important to point out that at $q = 0.3$ GeV both scaling functions take on similar values, that lie, however, far beneath the RFG scaling parabola. Also, one sees that scaling violations occur in the transverse response, yielding a growing excess strength with higher q.

6.2.3 Separated responses from GiBUU simulations

The Rosenbluth separation has been performed on cross sections calculated in our model. A sufficient set of data points had to be generated[6] due to numerical details explained in Appendix B.2.

In Figs. 6.11 and 6.12, we compare our approach to experimental data, the RFG predictions and model calculations by Fabrocini and Fantoni [FF89], that are based on orthogonalized-correlated-basis theory. Note that the transverse responses of the two experimental analyses agree while Jourdan finds less strength in the longitudinal channel.

[5]To obtain these relations, we compare Eq. (4.45) with Eq. (4.57) and equate them by elemination of the double-differential cross section. After dividing out the Mott cross section, we obtain the relation

$$v_\mathrm{L} R_\mathrm{L} + v_\mathrm{T} R_\mathrm{T} = v_\mathrm{L}\left(\frac{f G_\mathrm{L}}{k_\mathrm{F}}\right) + v_\mathrm{T}\left(\frac{f G_\mathrm{T}}{k_\mathrm{F}}\right), \tag{6.5}$$

which is supposed to hold for arbitrary v_L and v_T in the case of perfect superscaling. Eq. (6.6) follows directly. The observed discrepancies between $\frac{R_\mathrm{L}}{G_\mathrm{L}}$ and $\frac{R_\mathrm{T}}{G_\mathrm{T}}$ motivate the introduction of the separated scaling functions, f_L and f_T.

[6]Note that the non-relativistic LTF [Ros80] and the relativistic Fermi gas allow for an analytical solution, while for our model it is not possible to obtain analytic expressions of the responses, similar to Eq. (4.49). This is due to the integration being complicated by local Fermi momenta, a hadronic potential and finite particle widths. It is, however, possible to perform a numerical integration over the phase space, similar to Eq. (4.44), instead of generating multiple cross sections and performing a separation. With the scaling-extrapolation approach, presented in this Section, we perform a similar computation, though not valid for large ψ'.

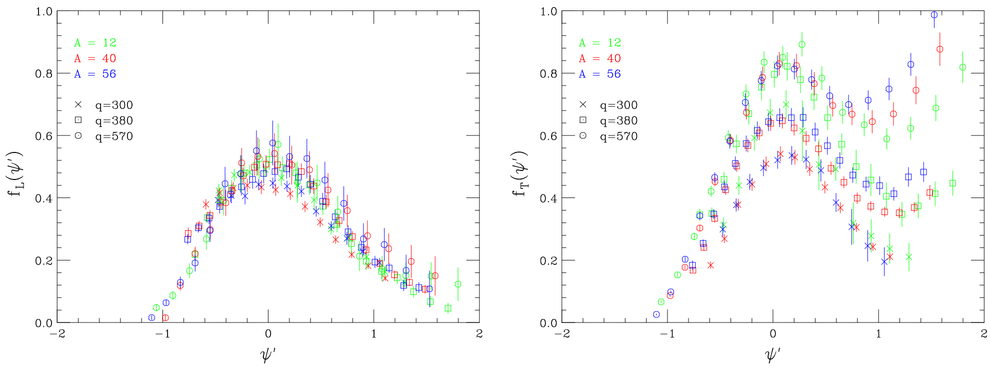

(a) Scaling function of the longitudinal response.
(b) Scaling function of the transverse response.

Figure 6.10: Separated scaling functions f_{L}, f_{R} for different momentum transfers 0.3, 0.38 and 0.57 GeV, assigned to symbols, and the nuclei ^{12}C, ^{40}Ca and ^{56}Fe, with nuclear mass numbers assigned to colors. Taken from Ref. [DS99], with data from the analysis in Ref. [Jou96].

When compared to the data of Williamson, which show the least longitudinal quenching, the simulated curves exhibit the same shortcomings as the inclusive cross sections presented in Sec. 5.2.5 and the scaling functions in Sec. 6.1.1: a narrowing and a shift of the QEP. Note also, that when comparing Fig. 6.12 to Fig. 6.11, the experimental longitudinal response shows a comparable lack of strength, while the transverse response in Fig. 6.12 overshoots model calculations from both, Fabrocini and GiBUU. In accord with Ref. [DS99], this can be interpreted as an excess strength in the transverse channel, that increases with q.

Just as for neutrino scattering, we can turn the superscaling approach around to use it as a means for predicting cross sections. Inserting an extracted scaling function, f, into Eq. (6.6), offers a different possibility for obtaining R_{L} and R_{T}

$$R_{\mathrm{L,T}} \approx f \frac{G_{\mathrm{L,T}}}{k_{\mathrm{F}}}. \tag{6.7}$$

We will call this approach the scaling extrapolation (SE).

It is interesting to observe to what extent GiBUU responses differ when they are obtained via Rosenbluth separation and via the scaling extrapolation. In Fig. 6.13, we compare with data for electron scattering on ^{40}Ca at a fixed momentum of $q = 0.3$ GeV, since the Rosenbluth separation is especially difficult in this case, as discussed in Appendix B.2. We find that, apart from statistical fluctuations affecting the Rosenbluth separated response, the scaling SE approach and the Rosenbluth separation agree perfectly.

This result is a direct consequence of the fact that GiBUU calculations exhibit first-kind scaling to a higher degree than experimental data, since varying electron energy for a fixed q results in varying ϵ and thus different amounts of longitudinal and transverse contributions. Contrary to the scaling functions in Fig. 6.10, we find the separated scaling functions obtained from our model to take on identical values. However, this result may be regarded as a cross-check for the implementation of the Rosenbluth separation and the superscaling analysis and as a time-saving method to predict separated responses of GiBUU simulations for the kinematical regions around the QEP.

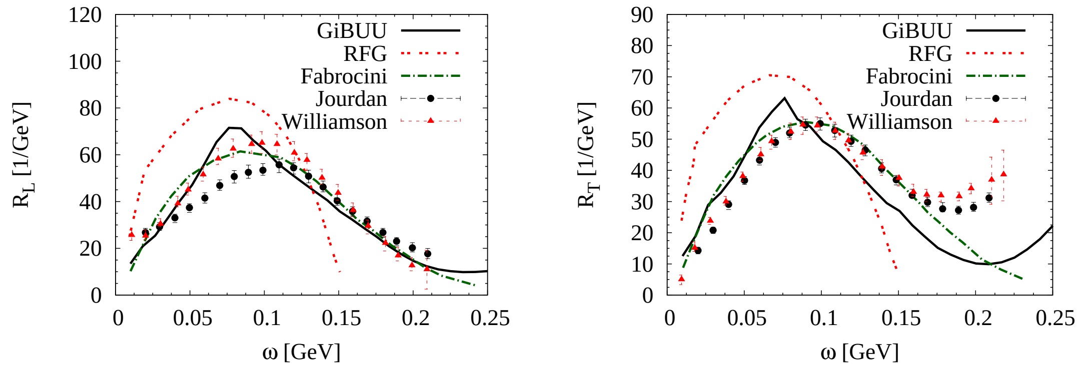

(a) Longitudinal response (b) Transverse response

Figure 6.11: Separated responses for electron scattering on ^{40}Ca at fixed momentum transfer $q = 0.38$ GeV from Ref. [Jou96] (circles) compared to GiBUU calculations with the LTF (solid lines)/ GFG initialization (dotted lines) and model calculations from Ref. [FF89] (dash-dotted lines) as well as data taken at $q = 0.375$ GeV from Ref. [W$^+$97] (triangles). In Fig. 6.15a, we compare to inclusive cross-section obtained at a similar momentum transfer.

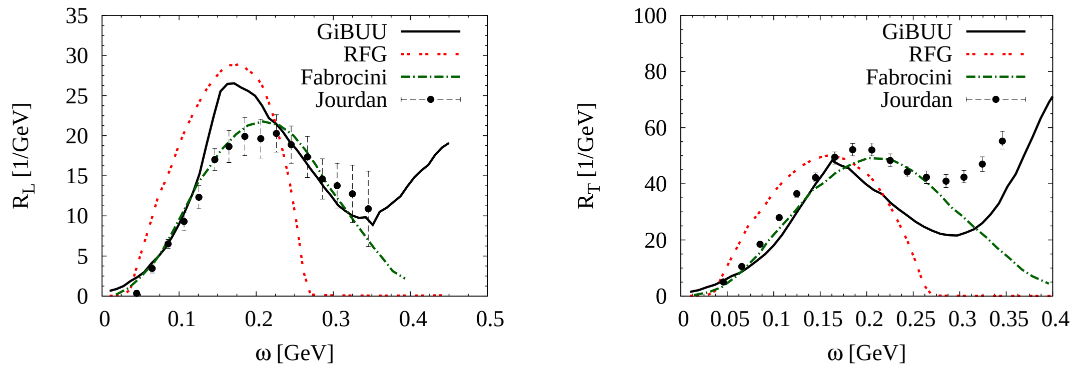

(a) Longitudinal response (b) Transverse response

Figure 6.12: Separated responses for electron scattering on ^{40}Ca at fixed momentum transfer $q = 0.57$ GeV from Ref. [Jou96] (circles) compared to GiBUU calculations with the LTF (solid lines)/ GFG initialization (dotted lines) and model calculations from Ref. [FF89] (dash-dotted lines). In Fig. 6.15b, we compare to inclusive cross-section obtained at a similar momentum transfer.

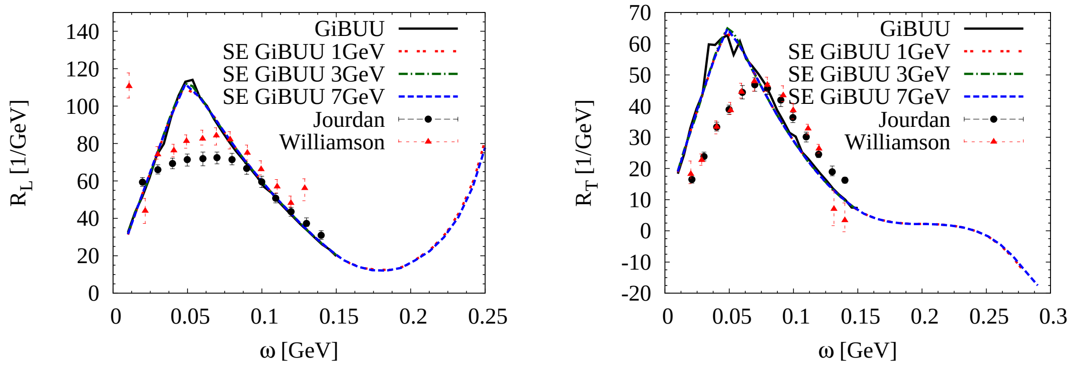

(a) Longitudinal response (b) Transverse response

Figure 6.13: Separated responses for electron scattering on ^{40}Ca at fixed momentum transfer $q = 0.3$ GeV from Ref. [Jou96] (circles) and Ref. [W$^+$97] (triangles) compared to GiBUU calculations obtained using the the Rosenbluth separation (solid lines) and the scaling extrapolation for 1, 3 and 7 GeV incoming electron energy (dotted, dash-dotted and dashed lines).

From Fig. 6.14 we find that our SE method is limited to the area of energy transfers below and not too far above the QEP. For larger energy transfers the Rosenbluth separation (RS) and the SE responses differ significantly, mainly because the SE response gains most of its strength in the longitudinal channel while the RS response, in better accord with data, substantially gains strength in the transverse channel. Thus we can conclude that within the GiBUU model first-kind scaling violations above the QEP arise mainly due to additional strength in the transverse channel. These effects can be attributed to resonance excitations and single-π non-resonant background. As we are mainly interested in the analysis of the QEP, we will nevertheless use the SE method throughout the rest of this section.

To conclude this analysis, we compare our calculations to experimental inclusive cross sections[7], which show the impact of the deviations of our model-response functions from the experimental ones on the inclusive cross section. The difficulties of a shifted and narrowed QEP, that occur in our model calculations, are evident in all plots. The effect of excess-transverse strength can best be seen in Fig. 6.15b, where the kinematics lead to a photon polarization of $\epsilon = 0.0033$ and $q = 0.57$ GeV at the QEP, meaning that the transverse contributions constitute a large part of the total response. In that case we see a large excess of strength at the experimental QEP, when compared to the (shifted) theoretical prediction. The excess is also visible for a similar value of q_{QEP} in Fig. 6.16b, though smaller in size due to larger longitudinal contributions at $\epsilon = 0.4$.

6.2.4 Effects on the separated responses

Finally, we present an analysis of the effects of different model parameters on the separated responses. In Fig. 6.17 we depict the influence of the same parameters as in Sec. 6.1.2, and see a similar effect on the response, although, due to the lower q involved, we can also distinguish the left side of the QEP from other contributions setting in at higher ω. We

[7] A useful collection of data can be found in Ref. [inc].

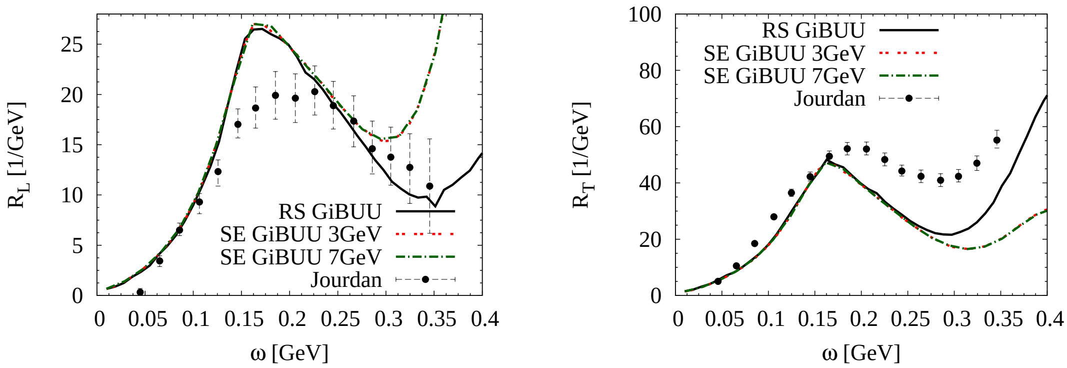

(a) Longitudinal response

(b) Transverse response

Figure 6.14: Separated responses for electron scattering on ^{40}Ca at fixed momentum transfer $q = 0.57$ GeV. Data taken from [Jou96] (circles) is compared with GiBUU responses obtained using the Rosenbluth separation (RS) method (solid line) and the scaling extrapolation (SE) at 3 and 7 GeV (dotted and dash-dotted line).

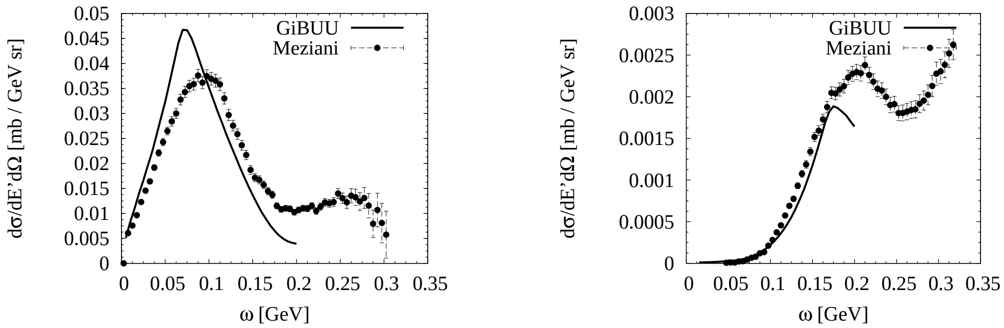

(a) Inclusive cross section for electron-nucleon scattering for incoming energy of 0.4 GeV and $\theta = 60°$, with $q = 0.32$ GeV and $\epsilon = 0.56$ at the QEP.

(b) Inclusive cross section for electron-nucleon scattering for incoming energy of 0.4 GeV and $\theta = 140°$, with $q = 0.57$ GeV and $\epsilon = 0.033$ at the QEP.

Figure 6.15: GiBUU calculations of double-differential inclusive cross section at QEP kinematics for scattering of electrons on ^{40}Ca (solid lines) as a function of energy transfer, ω, compared to data from Ref. [M+84] (circles).

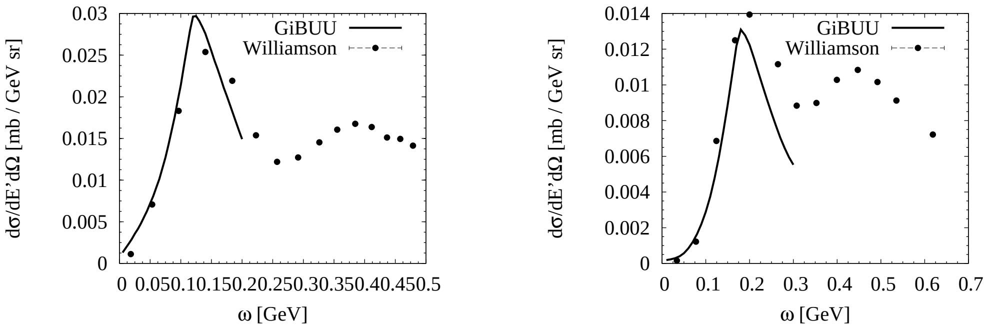

(a) Inclusive cross section for electron-nucleon scattering for incoming energy of 0.681 GeV and $\theta = 45°$, with $q = 0.48$ GeV and $\epsilon = 0.62$ at the QEP.

(b) Inclusive cross section for electron-nucleon scattering for incoming energy of 0.841 GeV and $\theta = 45°$, with $q = 0.6$ GeV and $\epsilon = 0.4$ at the QEP.

Figure 6.16: GiBUU calculations of double-differential inclusive cross section at QEP kinematics for scattering of electrons on ^{40}Ca (solid lines) as a function of energy transfer, ω, compared to data from Ref. [W$^+$97] (circles).

find that the inclusion of a hadron potential is important in order to obtain the correct slope of the response on both sides of the QEP.

6.2.5 Comparison with recent theoretical approaches

Summarizing the findings of this and the preceding section, we can outline a way towards achieving better agreement with electron-scattering data within the GiBUU model. Some issues, namely a shift of the QEP and violations of second-kind scaling, could be resolved with a refined momentum distribution, as will be discussed in the next section.

A more complicated question is raised by the appearance of violations of first-kind scaling with regard to incoming electron energy exhibited by data. Remember that the lack of these effects was the basis for application of the superscaling extrapolation method for obtaining the separated responses in our model. First-kind scale breaking is closely related to the different q dependence of longitudinal and transverse responses [DS99].

This can be further elucidated by looking at the scattering angles associated with the incoming energies in Fig. 6.1. At incoming lepton energy of 2 GeV and a momentum transfer of $q = 0.5$ GeV the kinematics gives a scattering angle of $\theta \approx 15°$ and hence, via Eq. (6.1), a large contribution from R_{L}, yielding a response much lower than RFG expectations. For $E_e = 0.32$ GeV and $q = 0.5$ GeV on the other hand, we have $\theta \approx 145°$ and a response that even exceeds RFG expectations. These two effects match perfectly with the findings in Fig. 6.12, where R_{T} exceeds RFG expectations, while R_{L} stay beneath them, at a ratio comparable with that in Fig. 6.11.

Since we lack separations of experimental data at large q for heavy and medium nuclei, at this point there are two possible conclusions that can be drawn from the presented analysis. Either our general scaling function is, except for the shift, correct at high energies and our model misses a *quenching of the longitudinal response* for all q and a *quenching of both repsonses* for low q, or our scaling function is too high and at high q is compensated by a *rise of the transverse response* of the real data. We will now review

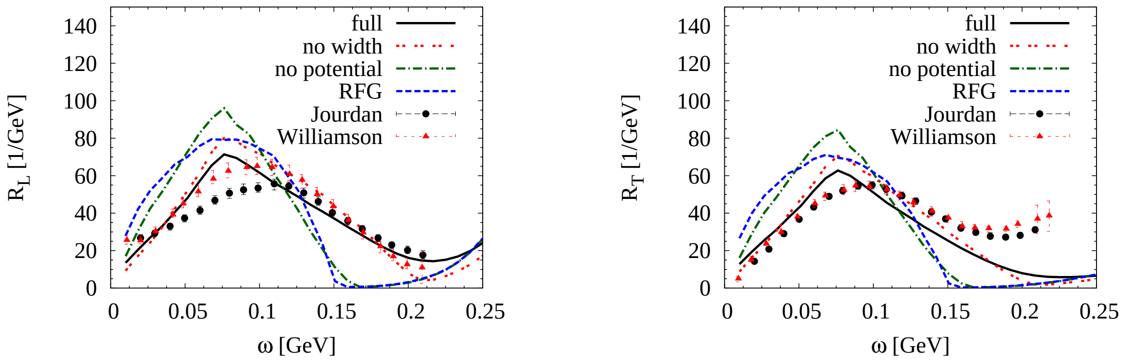

(a) Longitudinal response

(b) Transverse response

Figure 6.17: Study of separated responses for electron scattering on ^{40}Ca at fixed momentum transfer $q = 0.38$ GeV. GiBUU simulations include simple RFG simulation (dashed line), LTF simulation including no further effects (dash-dotted line), LTF simulation including a hadronic potential but no in-medium width (dotted line) and full calculations (solid line). Data taken from [Jou96] (circles) and [W$^+$97] (triangles).

theoretical developments on this question.

The Coulomb-sum-rule puzzle has motivated models that modify the nuclear-momentum distribution by including short-range correlations. An approach based on correlated-basis theory [Cla79] has been extended to include more advanced correlation operators by Pandheripande, Benhar, Fabrocini and Fantoni [FP88, BFF89]. In Refs. [FF89, Fab97] this approach has been applied to the separated responses. Comparing to their calculations in Figs. 6.11 and 6.12, we see that their results are in better agreement with the data than ours. However, one must stress that these non-relativistic calculations are limited to a certain kinematical range and already include meson-exchange currents (MEC) that account for a modification of the transverse response.

A continuation of the work on short-range correlations has been carried out in Ref. [AM09], where also a modification of the y-scaling variable has been introduced, and the connection between nuclear momentum distributions and the scaling function has been investigated. The recent debate on transverse-scaling violations is, however, not mentioned in their work.

A different approach is pursued by the coherent-density-fluctuation model, as developed in [AGK$^+$04, CBA$^+$10]. It is based on the generator-coordinate method [GW57] and includes long-range correlations for a prediction of a universal momentum distribution, that then translates into a scaling function. This scaling function corresponds to a scaling function for electron scattering at medium q, including an asymmetrical shape. So far the issue of scaling violations and separated responses has not been addressed within this approach.

In the BCS based model [BCDM08] by Barbaro *et al.*, the focus lies on the scaling function of the longitudinal response, which is supposed to be free of scaling violations. Their model is also able to reproduce the asymmetric shape of the scaling function.

We find similarities to our model in the relativistic-mean-field (RMF) method [CAB$^+$05, CMHU10], where initial- and final-state nucleons are subject to a relativistic mean field. In accord with our calculations shown in Fig. 6.4, their scaling function is substantially lowered as compared to RFG predictions.

In the semi-relativistic approach [ABC+07] an expansion of the on-shell electromagnetic current in powers of p/M_N, i.e., nucleon momentum over nucleon mass, is carried out in order to expand the validity of calculations performed in the non-relativistic quantum picture. In more recent applications of this method, the influence of MEC and pionic correlations on the transverse response is intensively studied [ABC+10a, AMB+10].

To relate the current status of research to our model, it is important to stress that recent models, that take the different behavior of the longitudinal and transverse response into account, all tend to interpret the longitudinal response as not being affected by scaling-violating effects. From such a standpoint the scaling function of our model at low q must be in any case regarded as too large, and should ideally take on the shape of the longitudinal scaling function for 2 GeV scattering in Fig. 6.10a. A way to reach agreement with the data would be the inclusion of scaling violations via additional cross sections, leading to the same final state (nucleon knock-out), but stemming from different effects. As a first proof of concept, one could also directly modify the transverse scaling function and then reevaluate the total cross section. Anyhow, the basic starting point would be lowering the scaling function to a peak level of about 0.6 and the right position. This will be pursued in the next section.

6.3 Ground-state analysis

Let us begin this discussion by reviewing the results in Sec. 6.1.2. In Fig. 6.4, we find that in our LTF-based model the inclusion of a hadronic potential does change the shape of the scaling function, but the actual position of the QEP is not affected. This finding is unsatisfactory since a hadronic potential is a reasonable way to account for the experimentally observed shift in ω_{QEP} away from its vacuum value, which is attributed to nuclear-binding effects. It can be explained by the density profile of the LTF (cf. Fig. 7.8 in Ref. [Bus08]), that shows a high probability of finding nucleons with low momenta at low densities. These low densities coincide with low potentials, as our Welke-type hadronic potential vanishes with vanishing width. As a consequence the nucleons at rest, i.e. the ones that contribute the most to the QEP, experience the least effects from the nuclear potential.

From this reasoning we can also interpret the violations of second-kind scaling, by recalling the description of nuclear densities in Sec. 5.2.2: As for large nuclei the density in the inner core is very similar and constant, most nucleons are distributed according to the same Fermi momentum. Only for small nuclei, most nucleons are initialized on the surface, where the are bound to have very small momenta, which as a consequence lead to increased strength of the scaling function at the QEP.

It is thus interesting to compare the global Fermi-gas approach to the LTF, while including all the other effects that were shown to improve scaling qualities in Sec. 6.1.2. In Fig. 6.18a, we perform a second-kind-scaling analysis with FG simulations and find that they show very good scaling. The minor deviations arising from the difference between the values[8] for k_{F}. Due to the large contributions at $\psi' > 0$, it is not clear whether the

[8]For both analysis and modelling we have used the k_{F} values 0.22, 0.23, 0.235 and 0.24 GeV for C, Al, Fe and Au [DS99].

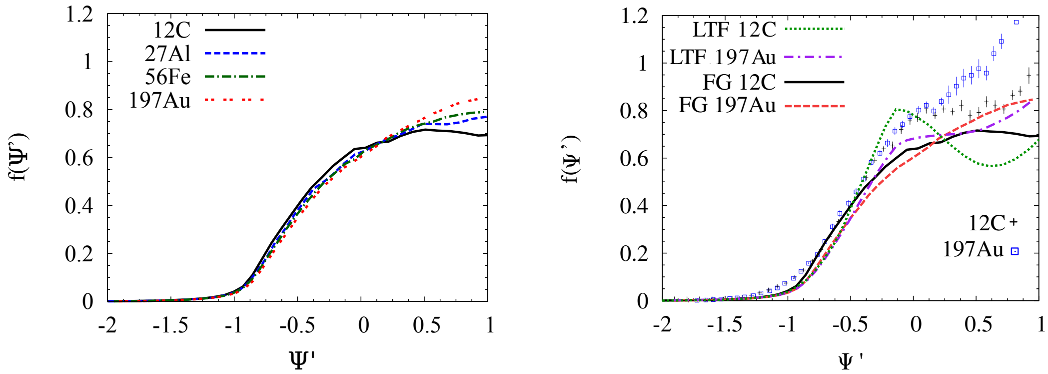

(a) GiBUU simulation of scaling functions with a global Fermi gas.

(b) Comparison of data taken from Ref. [DS99] with GiBUU simulations with a global Fermi gas (solid and dashed line) and a local Thomas-Fermi ground state (dotted and dash-dotted line) for carbon and gold.

Figure 6.18: Second-kind scaling analysis of electron scattering on ^{12}C, ^{27}Al, ^{56}Fe and ^{197}Au at a constant momentum transfer of q=1 GeV and incoming electron energy of 3.6 GeV.

QEP is reproduced at the correct position. When compared to experimental data, in Fig. 6.18b, the results show less agreement than the non-scaling LTF results. We interpret this, following the discussion in the previous section, as an effect of the excess-transverse strength that is missing in our model.

To study whether the position of the QEP is reproduced correctly, it is instructive to focus on the response at low q, where the non-quasielastic contributions to the scaling function are low. To also exclude contributions from the excess-transverse strength, in Fig. 6.19 we compare to the longitudinal scaling function. In addition, we show the corresponding response of a pure RFG model and the LTF model computed for $A = 12$ and $A = 197$. We find that even though the QEP is not correctly reproduced in the global Fermi gas model (at $\psi' \approx 0.25$ rather than at $\psi' \approx -0.25$ with as found in LTF with $q = 1$ GeV) it fits the data in size and shape as well as the LTF response for $A = 197$ and much better than the other calculations. One must state, however, that experimental data is only given for the nuclei ^{12}C, ^{40}Ca and ^{56}Fe. From the good second-kind scaling of experimental data we expect the longitudinal scaling functions to take on the same values for heavier nuclei.

We conclude that the GFG ansatz is better suited to model the longitudinal response and the transverse response at low $q \approx 0.3$ GeV, whereas the LTF approach gives results of the same quality only for heavier nuclei. We expect both approaches to fail for the transverse response at high $q > 0.5$ GeV, and also to not reproduce the QEP at the correct position. The last shortcoming can be corrected for with a phenomenological energy shift, which was shown to lead to a shift in ψ' in Appendix D.3. In Fig. 6.20, we perform a comparison similar to 6.1c but with a phenomenological energy shift and find that in this way the slope is much better fit.

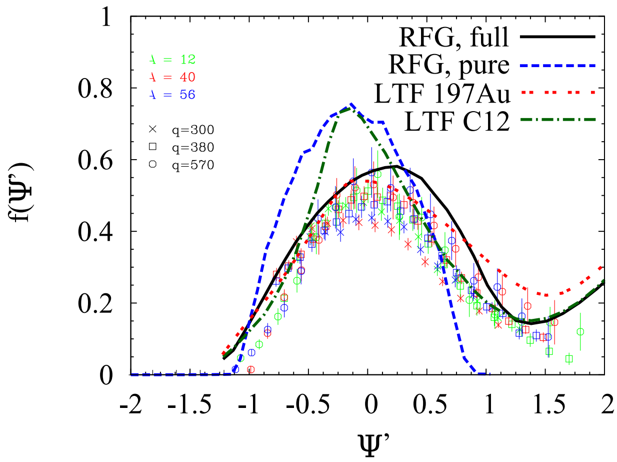

Figure 6.19: Comparison of experimental scaling function taken from Ref. [DS99] for ^{12}C, ^{40}Ca and ^{56}Fe (specified by color) and different q (specified by symbols) with different theoretical models. For ^{12}C and $q = 0.5$ GeV, the global FG model including hadronic potential and spectral functions (solid line) is compared with a global FG not including these effects (dashed line) and a LTF ansatz, for ^{12}C (dash-dotted line) and ^{197}Au (dotted line).

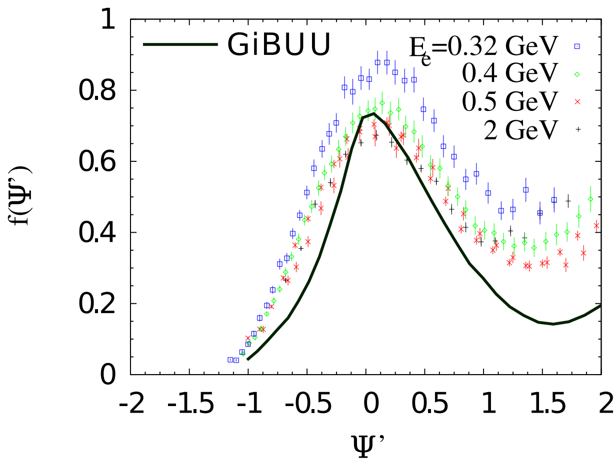

Figure 6.20: Analysis identical to Fig. 6.1c but the GiBUU results are shifted by the canonical value $E_{\mathrm{shift}} = 0.02$ GeV, so that the quasielastic peak of the simulation appears at $\psi' = 0$.

6.4 Relevance for neutrino scattering experiments

With the recent appearance of the first experimental muon-neutrino CC scatterring quasielastic double-differential cross sections for ^{12}C from the MiniBooNE experiment [AA$^+$10] it is very tempting to compare our model to data. However, one should not expect accordance, since in Ref. [LBMAR09] it is already found that the GiBUU prediction for the ratio of pion production over QE scattering underestimates the MiniBooNE data at about a level of 100 % if applied directly and still on a level of 20 % if corrected for final state interactions that lead to misidentifications of CCQE events (cf. Sec. 13.3 of Ref. [Lei09]).

In Fig. 15.1 of Ref. [Lei09] it is shown that other theoretical models suffer from the same shortcomings. In fact, the model advocated by the MiniBooNE collaboration and correctly describing the MiniBooNE data[9] is a relativistic Fermi gas that applies an unusually large axial mass, $M_{\mathrm{A}} = 1.35$ GeV, and a parameter to account for an increased strength of Pauli-blocking, $\kappa = 1.007$ [Kat09]. Remember that, as described in Sec. 2.3.2, in our model we use $M_{\mathrm{A}} = 0.999$ GeV as obtained from the analysis of past neutrino-nucleon data in Ref. [KLN08], in accordance with other analyses, e.g., Ref. [BEM02] where pion electroproduction is analyzed, that also yield values consistent with 1 GeV.

The experimental situation is further complicated by the fact that the incoming neutrino energy is not an observable quantity. It has to be reconstructed from the kinematics of the scattering partners. Furthermore, to obtain exclusive cross sections, like the CCQE one used to obtain the fit for M_{A} in Ref. [AA$^+$08], one has to subtract contributions from other channels. These channels are calculated using event generators, which again include assumptions about the neutrino-nucleus interaction.

Let us relate the findings of the previous sections to neutrino scattering. We have discussed and demonstrated, using the GiBUU model, that models for electron-scattering based on impulse approximation suffer from an underestimation of the transverse response at large momentum transfers, $q > 0.4$ GeV. Many approaches, cf., e.g., the discussion in Ref. [ABC$^+$10a] and the references therein, consider MEC to be the cause of this effect, with 2p-2h calculations, e.g. Ref. [DPNA$^+$04], aiming at fully describing these effects. In the light of the superscaling analysis these effects manifest in an increase of the transverse scaling function. Just by comparison with data we estimate that these effects cause a rise of the transverse scaling function by a factor of 1.8, for $q > 0.5$ GeV. As the neutrino response consists of more intricate components (cf. Eq. 4.67), it is not straight-forward to extrapolate these findings to neutrino cross sections. A first approach would be to include the found excess-transverse strength in the component X_T^{VV}, thus allowing for a response that is twice as high for special kinematics. This approach has been recently pursued in Ref. [ABC$^+$10b], where it is found that inclusion of these effects leads to an increase of the double-differential inclusive muon-neutrino CC cross section, but still underestimates the recently released MiniBooNE data [AA$^+$10]. As for CC scattering there exist more responses which could also be affected by MEC, but have not been yet studied, we find that the theoretical description of neutrino-nucleus-scattering experiments is subject to very large uncertainties.

[9] We should also note that Ref. [MECM09] manages fitting the MiniBooNE data by computing the response in random-phase approximation.

Chapter 7

Summary and conclusive remarks

In this work, we have highlighted the role of nuclear effects in lepton-nucleus scattering using a model that treats neutrino and electron scattering within the same formalism. Performing a superscaling analysis and the separation of the longitudinal and transverse response, we were able to gain more insight into important nuclear effects and thus make suggestions for future improvements on the one hand and point towards uncertainties in the analysis of present experiments on the other.

7.1 Summary

In Chapter 2, we have described the fundamental interactions on the lepton-quark and lepton-nucleon level. We began by outlining the basic formalism underlying all of the calculations. Later, we have argued that three processes play an important role in the kinematic region of our interest, namely QE scattering, resonance excitation and non-resonant single-π background, and presented methods to calculate their contributions.

In Chapter 3, we have considered important aspects for building nuclear models capable of describing lepton-nucleus scattering. First, we have discussed possible frameworks for describing the interaction. We have then highlighted the role of the nuclear ground-state and in-medium modifications to the single-nucleon scattering scenario.

Building on these ideas, in Chapter 4, we have outlined the development of different scaling and superscaling approaches. We have argued that these analysis methods constitute a possible way to disentangle the single-nucleon cross sections from the electron-nucleus cross sections and obtain the nuclear information hidden in experimental data. We have also showed how to derive the scaling variables from energy-conservation considerations and how the different scaling variables relate to each other.

In Chapter 5, we have presented our model for the description of lepton-nucleus scattering, starting from the underlying principles of non-equilibrium quantum-statistical mechanics. We have presented some details on the implementation of the GiBUU model and argued that even though the transport part of the code has not been used for our analysis, the fact that the model is tested against experimental data in different physical applications constitutes a major strength.

Finally, we have applied our model to current fields of research in Chapter 6. We have studied whether the electron- and neutrino-scattering cross sections predicted by our approach exhibit superscaling properties and found that this is the case to a reasonable degree. We have analyzed the slight deviations from experimental data and pointed to their origin, thus substantiating ways for improving the model. The finding that our model scales well is an implication that it can be used for various kinematics and nuclear targets, yielding predictions of similar quality.

We have then separated the longitudinal and the transverse response, and, drawing a connection to the superscaling analyses, found that our model describes the responses reasonably well, while the recently established effect of excess-transverse strength is missing. We have, in the light of these two analyses, further illuminated the role of the ground state and showed that using a hadronic potential, in-medium widths and a phenomenological energy shift, our model is able to describe both slope and size of the scaling function. As a conclusion we state that using the local Thomas Fermi approach our full model describes data best for large nuclei and small contributions from transverse channels, while the global Fermi-gas approach has the advantage of treating all nuclei on an equal footing. Finally, we have argued that the observed uncertainties, especially the transverse contributions, pose a major complication to the evaluation of current neutrino scattering experiments and that no model is so far able to consistently deal with all of the effects mentioned.

We conclude that the implementation of the superscaling analysis and the Rosenbluth separation in the context of the GiBUU model helps disentangle and understand effects that are otherwise hidden in the inclusive cross sections. The comprehensive investigation of the scaling phenomenon performed in Chapter 4 and in Appendix C is a prerequisite to the understanding of the underlying kinematical and statistical effects. Apart from pointing out in which kinematical regions and for what reason our model has good predictive power, we are confident that future attempts to improve the model will benefit from the presented results and the implemented tools.

7.2 Outlook and future improvements

In our analysis, we have shown, that two aspects of the nuclear response deserve special attention. On the one hand, a large role is played by the initial nucleon-momentum distribution, as can best be assessed by the study of scaling functions. On the other hand, the appearance of excess strength in the transverse channel poses an interesting question, as could be seen in the analysis of the separated longitudinal and transverse responses.

It would be an interesting task to improve the initial-state-phase-space distribution in a way that the physical advantages of a local Thomas Fermi description, e.g., smaller Fermi momenta at the surface, are kept, but the binding energy is a constant regardless of nucleon position, thus helping to correct the position of the QEP. Microscopically motivated momentum distributions should also be taken into account.

An effect, that is more difficult to adopt within the framework of the GiBUU model, is the excess strength in the transverse channel. If one were only interested in the description of double-differential inclusive cross sections, a promising ansatz would be to study the excess strength in terms of longitudinal and transverse scaling functions. Starting from a model that correctly describes the response at low q, one could attribute the underestimation of the inclusive cross section at higher q to an underestimation of the transverse scaling function, thus obtaining a q-dependent parametrization of excess in the transverse scaling function, without running into the problem that at higher q separated experimental responses are not available.

Since the treatment of final-state interactions is a strength of the GiBUU model, and such an ad-hoc ansatz would be hard to consistently combine with the transport approach, a microscopic solution to the problem would be more desirable. One possibility would be to introduce an in-medium modification to the hadronic current in Eq. (2.41). It would be worth studying, whether a simple modification of the form factors could already lead to the desired effects, or whether additional terms would have to be introduced, as done in Ref. [DF83] in order to derive the off-shell prescription for the single-nucleon cross section, presented in Appendix D.1. How and whether quantum-mechanical many-body effects can be combined with a transport-based approach also poses an interesting question.

Appendix A

Conventions and notations

A.1 Units and constants

For the sake of simplicity, we use natural units, i.e. $\hbar = c = 1$, throughout this work. Electromagnetic effects are treated in Heaviside-Lorentz units[1]. Thus, only one choice for a scale remains and we pick energy measured in GeV as our basic unit, leading to the following relations for the remaining quantities

$$[\text{energy}] = [\text{mass}] = [\text{momentum}] = [\text{time}]^{-1} = [\text{length}]^{-1}.$$

For conversion to International System of Units, one can apply the useful relation

$$\hbar c \approx 0.197326968 \text{ GeV fm} = 0.197326968 \text{ GeV} \cdot 10^{-15} \text{ m}. \tag{A.1}$$

Within this work, we consider both cross sections for electron scattering, which are usually expressed in units of milibarn ($1 \text{ mb} = 10^{-3} \cdot 10^{-28} \text{ m}^2$), and neutrino scattering, which are often given in 10^{-38} cm^2. In order to increase consistency, we will express energy and solid-angle differential cross sections, which lie in the focus of this work, for both kinds of leptons in the following way

$$\left[\frac{\mathrm{d}\sigma}{\mathrm{d}\Omega \mathrm{d}E_f}\right] = \left[\frac{\text{mb}}{\text{sr GeV}}\right].$$

Moreover, we list the most important physical constants, which our theory takes as input parameters, in Table A.1.

A.2 Definitions and notations

A detailed discussion on definitions of kinematical entities can be found in Sec. 2.2.3. Here we describe our general conventions. For sums of vector components, we use Einstein's summation convention, i.e., $a^i b^i = \sum_i a^i b^i$. Three-vectors are expressed by bold letters, e.g., $\mathbf{p}$, with the usual notation for the Euclidean inner product, i.e., $\mathbf{p} \cdot \mathbf{k}$. Their absolute values, except for q, are always written out explicitly, e.g., as $|\mathbf{p}| = \sqrt{\mathbf{p} \cdot \mathbf{p}}$. Italic letters,

[1]The elementary charge is hence given by $e = \sqrt{4\pi\alpha}$, with $\alpha = 1/137$

quantity	symbol	value
fine-structure constant	α	0.007297
positron charge	$e = \sqrt{4\pi\alpha}$	0.302814
Fermi coupling constant	G_{F}	$1.16637 \cdot 10^{-5}$ GeV^{-2}
Cabbibo mixing angle	$\cos\theta_C$	0.9745
weak-mixing angle	$\sin^2\theta_W$	0.2228
neutrino mass[2]	m_ν	0
electron mass	m_e	0.00051099892 GeV
muon mass	m_μ	0.105658369 GeV
pion mass	m_π	0.138 GeV
nucleon mass	M_N	0.938 GeV
pion decay constant	f_π	0.093 GeV

Table A.1: Frequently used physical constants with values taken from the Particle Data Group 2008 analysis [A$^+$08].

BG	non-resonant single-pion background
CC	charged current
CM	center of momentum
DIS	deep inelastic scattering
EM	electromagnetic
h.c.	hermitian conjugate
LTF	local Thomas-Fermi gas
NC	neutral current
PCAC	partially conserved axial current
QE	quasielastic (elastic for electron scattering)
QEP	quasielastic peak
RHS	right hand side

Table A.2: Frequently used abbreviations.

on the other hand, can describe both a scalar, e.g., p^0, and, as a shorthand, a four-vector $p = p^\mu = (p^0, \mathbf{p})$. Minkowski inner products are written as $p_\mu k^\mu$ or $p \cdot k$, while the shorthand $p^2 = p_\mu p^\mu = {p^0}^2 - |\mathbf{p}|^2$ may also be used.

Abbreviations are written out at first use, but in addition we summarized the most frequently used ones in Table A.2.

A.2.1 Relativistic quantum mechanics

For the relativistic-quantum-mechanics part of our calculations we follow the conventions developed in Chapters 4 and 5 of [HM08]. This means starting out with the "West Coast"

[2]Note that, while long baseline experiments can measure the mass squared difference through comparison of fluxes at long dinstances, cross sections from neutrino scattering experiments are not sensitive to the tiny value of the neutrino mass and it is hence safe to neglect these effects in our calculations.

metric,

$$g^{\mu\nu} = \mathrm{diag}(1, -1, -1, -1), \tag{A.2}$$

and using the Dirac-Pauli representation for both, spin matrices

$$\boldsymbol{\sigma} = (\sigma^1, \sigma^2, \sigma^3) = \left[\begin{pmatrix} 0 & 1 \\ 1 & 0 \end{pmatrix}, \begin{pmatrix} 0 & -i \\ i & 0 \end{pmatrix}, \begin{pmatrix} 1 & 0 \\ 0 & -1 \end{pmatrix}\right], \tag{A.3}$$

and Dirac matrices,

$$\gamma^\mu = (\gamma^0, \boldsymbol{\gamma}) = \left[\begin{pmatrix} \mathbb{1}_2 & 0 \\ 0 & \mathbb{1}_2 \end{pmatrix}, \begin{pmatrix} 0 & \boldsymbol{\sigma} \\ -\boldsymbol{\sigma} & 0 \end{pmatrix}\right]. \tag{A.4}$$

Then we can attribute a spinor in momentum space, $u(p, s)$, to any free fermion of spin $s = \pm\frac{1}{2}$ and positive energy. The spinor must satisfy the Dirac equation

$$(\not{p} - m)u(p, s) = 0, \tag{A.5}$$

with $\not{p} = \gamma_\mu p^\mu$. Coordinate-space wave functions of massive spin 0 particles, e.g. pions, on the other hand, obey the Klein-Gordon equation

$$(\partial_\mu \partial^\mu + m^2)\phi(r) = 0. \tag{A.6}$$

For wave equations of particles of higher spin we refer the reader to Ref. [Gre00].

Treating fermions and bosons in the same manner, we choose the normalization such that we obtain $2E$ particles per unit volume. This implies the orthogonality relations

$$u^\dagger(p, s)u(p, r) = 2E\delta_{sr} \tag{A.7}$$

and

$$\bar{u}(p, s)u(p, r) = 2m\delta_{sr}. \tag{A.8}$$

Appendix B

Numerics and programming

In this chapter, we present our solutions to numerical and computational problems that arose during the course of this thesis. While the work on the GiBUU code was carried out in the FORTRAN programming language, analysis and file management were handled in Python and the UNIX-native bash scripting language. All programs are available in the version control system of the GiBUU project.

B.1 Using Python scripts to automate development and job-card submission

Simulations are usually connected with large amounts of output but sometimes also with a great variety of input files. Both sides (input and output) need to be handled automatically, and usually depending on one another. Here, we present some novel tools for working with GiBUU that were needed to handle the vast amount of separate job cards connected with the superscaling analysis, where the same reaction is analyzed for a wide range of nuclei and kinematics, and the separation of the transverse and the longitudinal response, treated in the next section.

B.1.1 Why Python?

Working on UNIX-like operation systems, a natural choice would be to use Bash scripts to automate file handling. Such efforts have been undertaken by most of the GiBUU users. However, when coming to more complex applications, the scripts become practically unmaintainable since the lack of language functionality (e.g., string handling) needs to be compensated by using chains of external programs with varying syntax and error handling. The considered scripts, containing lines of the following kind

```
free | tr -s ' ' | sed '/^Mem/!d' | cut -d" " -f2-4 >> mem.stats
```

convinced us to look for an alternative. With Python [Pyt] being a mature interpreted language, not only its high level (object-oriented) design patterns but also the interactive debugging possibilities looked very promising.

B.1.2 The general framework

With the natural working environment being the command line, a way for comfortably handling options and arguments that were passed to the scripts had to be found. Unfortunately, employment of the Bash-inspired *getopt* module, included in the standard Python distribution, still resulted in many redundant lines of code, so a new approach was conceived. The ODic module [ODi] was developed, with its main focus on:

- multi-purpose & single-location documentation,
- prevention of design-pattern redundancy,
- user friendly output and
- developer-friendly debugging and testing.

It has served as the basis for the various analytical tools developed throughout the work on this thesis, its rigid structure and testing capabilities allowing for quick enhancement of existing tools.

B.1.3 Example

While most of the developed scripts are concerned with the analysis of data files, a specific script should be mentioned separately. The module *send_jobs.py* has made the automated submission of thousands of jobs to the computing cluster possible, while also organizing the output and deleting redundant files. Since it is already employed by other users and might also be of service to future users of GiBUU and since its structure is a good example of the programming paradigm connected with the ODic module, we will briefly review the code structure of this specific module. To get an impression of the implemented functionality, we state the program's output to the command *send_jobs.py –help*.

```
============
 send_jobs
============

____________________________________________________________
A scientific computing job submitter
____________________________________________________________


SYNOPSIS
========

  send_jobs.py [ OPTIONS ] [ FILES]

DESCRIPTION
===========

  Running "send_jobs.py" with job cards as arguments will copy them to a remote
  machine, automatically submit them to the grid engine, and after completion
  organize the output.
...
```

Now for the code of *send_jobs.py* itself: After specifying the interpreter, the module begins by a so called docstring, indicated by the triple quotes.

```
#!/usr/bin/python

"""=============
 send_jobs
=============

---------------------------------------------------------------------
A scientific computing job submitter
---------------------------------------------------------------------

:Author: Ivan Lappo-Danilevski
...
```

Within our approach the docstring contains both, version information and help messages. It is formatted according to the Restructured Text format [RST], allowing for intuitive editing and automatic conversion to the UNIX man page format.

Now let us jump to the end of the code, where the *main* function is defined. We have omitted some lines to focus attention on the main points.

```
def main(argv=None):
    date=str(datetime.now()).split('.')[0].split(' ')
    defaults = {('c','clean'): False,
                ('','patience'): 300.,
...
...
                ('','maxjobs',): 1000,
                ('t','target'): [],
...
...
                ('','priority'):-1024,
...
                }
    append_dic(defaults, user_defaults)
    presets = {}
    append_dic(presets, user_presets)

    return Script(doc=__doc__,argv=argv,defaults=defaults, presets=presets,
                  run=send_the_jobs,).run()
    # ------------------------------------------------------------------------
if __name__ == "__main__":
    from sys import exit
    exit(main())
```

If the module is executed (*__name__ == "__main__"*), the program exits with the result of *main()*. This function initializes some preset options and then returns the result of the method *run()* of the newly created instance of the *Script* class, which lies at the heart of the ODic module.

The *Script* class takes the modules' docstring, the command-line input (*argv*), the *defaults* (which contain information about possible command-line options and their preset values), the *presets* (which contain user-specific parameter sets) and the *send_the_job* function, which is linked to the method *run*, as input. A strength of this approach is that the *defaults* dictionary defines the accepted command-line options, their standard value, and the accepted format of the arguments. In Fig. B.1, we depict the usual flow

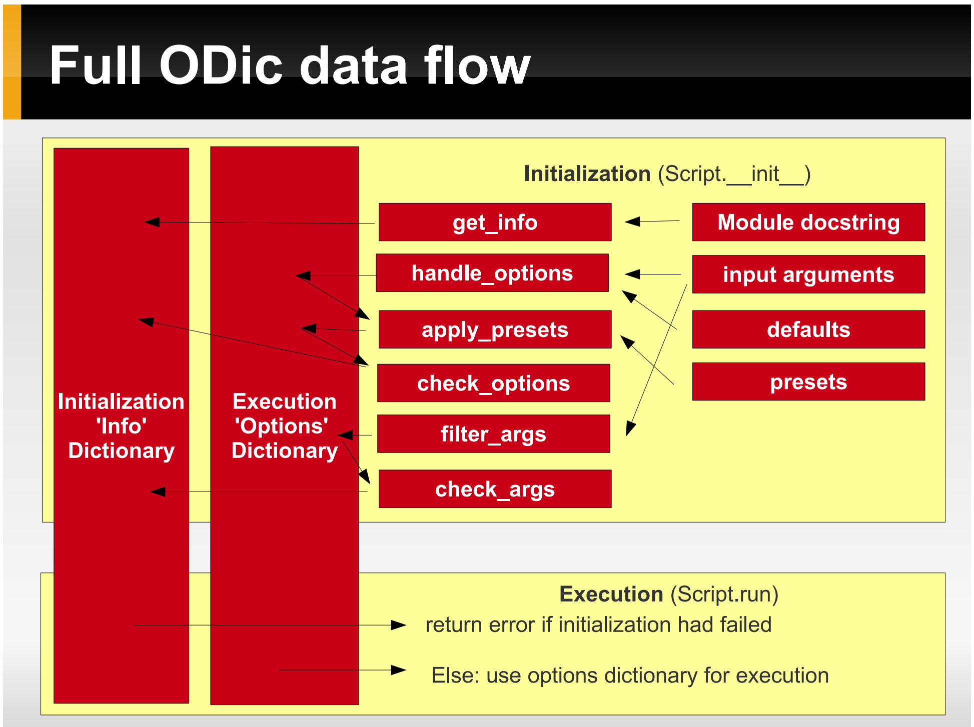

Figure B.1: Handling of presets and arguments in the ODic module. The two dictionaries on the left store relevant information, which is extracted during the initialization step by the class methods in the middle column from the user and programmer defined entities on the right. During the execution, the relevant information is available through the *info* and *options* dictionaries.

of information from programmer and user to a working instance of a *Script* class. The programmer does not have to care about option assignment and can use the automatically checked and assigned option values via the *options* dictionary in other parts of the code. According to line 225 of the presented module, *options['maxjobs']* will return either the default value 1000 or another *integer* value specified by the user via the command-line option *'–maxjobs'*.

So far, we have seen that the ODic module allows for quickly implementing a command line tool with full option and argument handling. The actual functionality of the program is passed to the class instance through the variable *run=send_the_job* in line 237. We want to conclude this example by highlighting the chain of events within this function. For this reason, we have extracted the most important steps and assigned new line numbers. In line 4 the entire parameter set is saved to *config.pickle*. This file is then transferred by means of the UNIX tool *scp* to the remote machine.

We have omitted the part where the job cards and various other files are transferred and only highlight line 10, where *ssh* is used to execute the script *manage_jobs.py* on the remote machine. *manage_jobs.py*, which is written in the same style, then simply imports the *options* dictionary from *config.pickle*, submits the jobs to the cluster and afterwards organizes the output according to the parameters obtained from *config.pickle*.

```
def send_the_jobs(options):
  "send the jobs to the selected grid engine"
  ...
  pickle.dump(options,open(options['project']+'/config.pickle','wb'))
  sh(['scp',options['project']+'/config.pickle',options['user']+'@'+options
      ['host']+':'+options['project']],output='hide')
  ...
  if not options['debug']:
    print str(datetime.now()).split('.')[0]+' SEND_JOBS: Starting
        MANAGE_JOBS on remote machine > jobs will be submitted'

    sh('ssh '+options['user']+'@'+options['host']+' "cd '+options['project'
        ]
                    +'; '+options['pythonpath']+' manage_jobs.py --log"',
                        shell=True)
  else:
  ...
```

As we have seen in this example, the ODic paradigm allows for consistent modular programming, since options dictionaries can be passed from module to module. We have also seen that the defaults dictionary relieves the programmer from explicit setting of values and input handling, since all that needs to be specified is the name of the option and the preset value. We conclude that the programming effort, which was a response to the necessity of treating large amounts of job cards, actually led to a more consistent and powerful collection of tools.

B.2 Separation of the transverse and the longitudinal response

As pointed out in Sec. 6.2, the Rosenbluth-type separation of the longitudinal and the transverse response in Eq. (6.2) is a linear equation for the two variables R_{L} and R_{T}. It is thus theoretically sufficient to supply two measured cross sections with identical q^2 and Q^2 but different scattering angle to obtain the unambiguous solution.

The results of such a separation with two data points are not satisfactory, neither when performed with experimental data (cf. discussion in Sec. 10 of Ref. [BDS08]) nor when performed with GiBUU simulations, where the response takes on unphysical, i.e., negative, values and lacks smoothness as depicted in Fig. B.2. Since the situation does not improve with larger statistics for the single runs, we are forced to generate more points and then perform a least-squares fit on the data. In this way, the separation for Figs. 6.11 and 6.13 was obtained. It is noteworthy that we achieved the best results with 50 data points, resulting in 1000 job cards for every figure. This massive amount of data has been the main motivation for developing the advanced scripting framework described in the previous section.

However, it has not been possible to further increase smoothness of the curve, while the discussion of our model in Sec. 6.2.3 indicates that the separated responses should coincide with the perfectly smooth responses from the scaling extrapolation. Especially

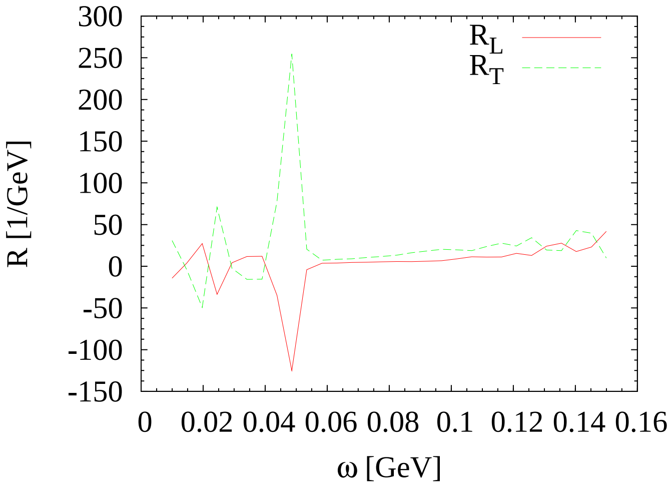

Figure B.2: Longitudinal (solid line) and transverse (green line) for electron scattering on ^{40}Ca with $q = 0.57$ GeV.

interesting is the finding that more precise calculations[1] resulted in less smooth curves. In Fig. B.3 we find that the simulated data with low statistics (dashed line) exhibit larger and apparently random deviations from the linear least-squares fit (dash-dotted line), while the high statistics results (solid line) show a sort of oscillatory behavior.

It is interesting to draw the connection to the concept of superscaling. In order to generate the data points for the Rosenbluth separation, only the incoming energy and scattering angle can be varied, while q^2 and Q^2 have to be kept fixed, thus also fixing ψ'. If our model were to exhibit perfect first-kind scaling, all kinematical combinations with the same ψ' should lead to an identical value of the scaling function, $f(\psi')$. However, in Fig. B.4 we observe an oscillation of small amplitude of the scaling function of the high statistics simulation when plotted over the incoming energy of the electron. This oscillation can be seen for various values of ω, cf. Fig. B.5, though different in amplitude and frequency, leading to an oscillation pattern of the separated responses, that manifests itself in Fig. B.6. We consider this minor scaling violation effect, which only plays a role for the Rosenbluth separation, to be a consequence of the imperfect angular isotropy of our model, that enters as a numerical inevitability through the introduction of spatial grids.

The Rosenbluth separation can still be successfully performed, when reducing the precision for the single calculation but taking more data points into account. We conclude that for the kinematical region of the QEP the scaling-extrapolation method for obtaining the separated responses, presented in Sec. 6.2.3, should be preferred, since it is a factor 20 faster and at the same time leads to maximally smooth results.

[1]As the best parameter set we identified 10 "same-energy runs" with 500 "parallel ensembles". For the meaning of these parameters we refer the reader to Sec. 5.5.1 of Ref. [Bus08]

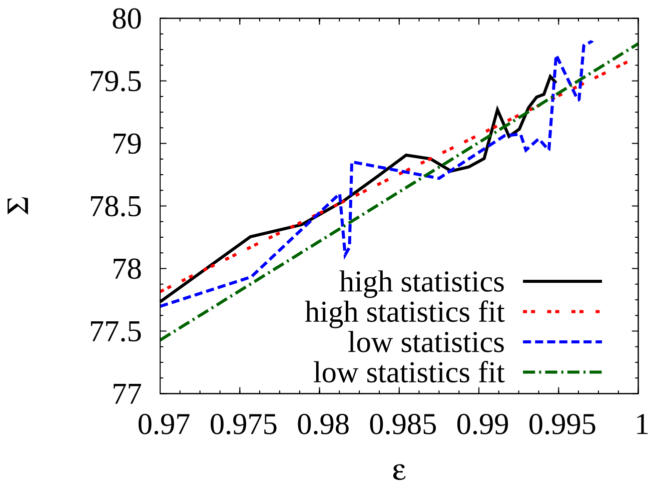

Figure B.3: Rosenbluth plot (Σ vs. ϵ, as defined in Eq. (6.2)) of GiBUU simulated data for electron scattering on ^{40}Ca with $q = 0.3$ GeV and $\omega = 0.097$ GeV. Simulations with high statistics of 30 "same-energy runs" (solid line) are compared with lower statistics of 10 "same-energy runs" (dashed line) and with the least-squares fit to both simulation (dotted and dash-dotted lines).

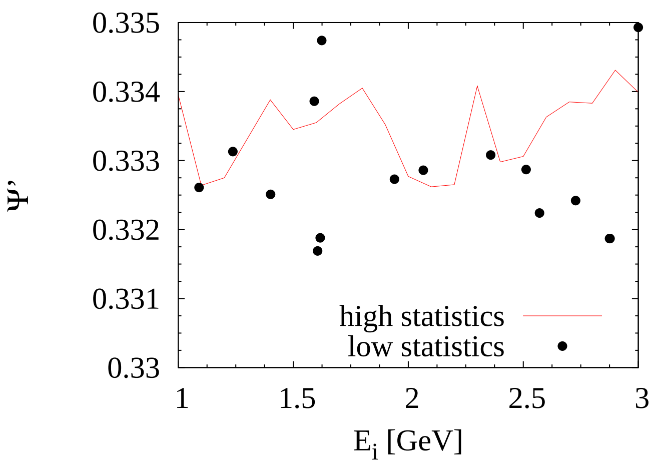

Figure B.4: Scaling function of GiBUU simulated data for electron scattering on ^{40}Ca with $q = 0.3$ GeV and $\omega = 0.097$ GeV vs. incoming electron energy. Simulations with high statistics of 30 runs (solid line) are compared with lower statistics of 10 runs (circles).

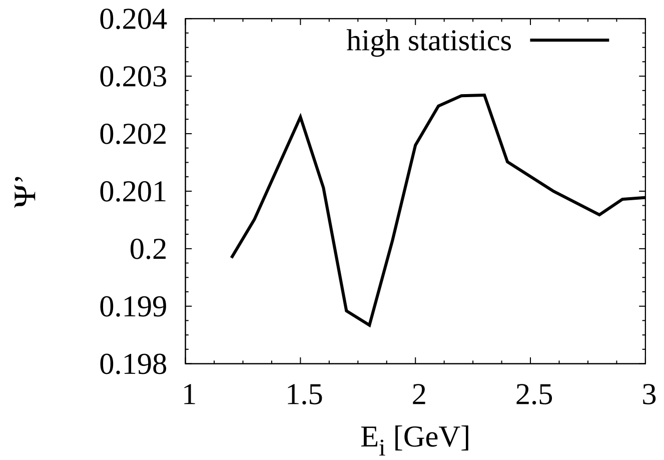

Figure B.5: Scaling function of GiBUU simulated data (high statistics) for electron scattering on ^{40}Ca with $q = 0.3$ GeV and $\omega = 0.01$ GeV vs. incoming electron energy.

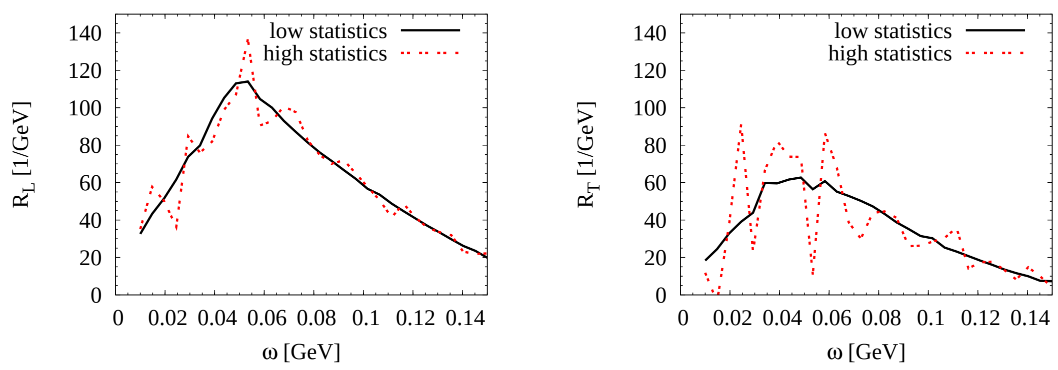

(a) Longitudinal response

(b) Transverse response

Figure B.6: Separated responses for electron scattering on ^{40}Ca at fixed momentum transfer $q = 0.3$ GeV for GiBUU simulations with high statistics (dotted lines) and low statics (solid lines).

Appendix C

Scaling variables

C.1 Derivation of the non-relativistic y-scaling variable

West's seminal analysis [Wes75] has included different scattering processes and different scaling approaches. It has been the inspiration for many following studies. In this section, we focus on how the y-scaling variable, derived in another context in Sec. 4.2, appears in West's original approach. As a starting point, we examine an interaction that takes place in the non-relativistic quantum mechanical picture (cf., e.g., Sec. 9.1 of Ref. [GY03]), where the double-differential cross section is given by

$$\frac{\mathrm{d}\sigma}{\mathrm{d}k^{0\prime}\mathrm{d}\Omega_{k'}} = \sum_f |\langle \mathbf{k}'\psi_f|H_\mathrm{I}|\mathbf{k}\psi_0\rangle|^2 \delta(k^{0\prime} + E_f - k^0 - E_0) \frac{\mathbf{k}'^2}{(2\pi)^3 v} \frac{\mathrm{d}|\mathbf{k}'|}{\mathrm{d}k^{0\prime}}. \tag{C.1}$$

with H_I being the part of the Hamiltonian responsible for the interaction between target and probe, in this specific case given by the Coulomb potential, $\Psi_{0,f}$ being the initial- and final-state nucleus wave with corresponding energies, E_0, E_f, and v the velocity of the incoming electron. Neglecting higher-order effects of the nucleus' Coulomb field on the electron, both, the incoming and the outgoing electron, are modeled as plane waves. The nucleus is supposed to be described as a simple product of radial waves of the form $\psi_0(\mathbf{r}) \propto \exp(-\beta|\mathbf{r}|)/|\mathbf{r}|$.

Expressing the Coulomb potential as the integral over the charge distribution,

$$V_i(\mathbf{r}) = \int \mathrm{d}^3\mathbf{r}' \frac{\rho_i(\mathbf{r}')}{|\mathbf{r} - \mathbf{r}'|}, \tag{C.2}$$

one is led to a separation of the RHS of Eq. (C.1) into the Rutherford cross section,

$$\left(\frac{\mathrm{d}\sigma}{\mathrm{d}\Omega_{k'}}\right)_\mathrm{Ruth} = \frac{\alpha^2}{4k^{0 2}} \frac{1}{\sin^4(\theta/2)} \tag{C.3}$$

and the structure function,

$$W(\omega, q) = \sum_f \left| \langle \psi_f | \sum_i F_i(q^2) \exp(\mathrm{i}\mathbf{q}\mathbf{r}_i) |\psi_0\rangle \right|^2 \delta(E_f - E_0 - \omega), \tag{C.4}$$

which consists of a sum of matrix elements of the elastic form factor[1],

$$F_i(q^2) = \int \mathrm{d}^3\mathbf{r} \exp(\mathrm{i}\mathbf{qr})\rho_i(\mathbf{r}). \tag{C.5}$$

The separation reads

$$\frac{\mathrm{d}^2\sigma}{\mathrm{d}k^{0\prime}\mathrm{d}\Omega_{k'}} = \left(\frac{\mathrm{d}\sigma}{\mathrm{d}\Omega_{k'}}\right)_{\mathrm{Ruth}} W(\omega, q). \tag{C.6}$$

Since one is interested in an inclusive process, in Eq. (C.4) knowledge of all final states, $|\psi_f\rangle$, is required. One can circumvent this by first writing the δ function as a Fourier transform in time[2] and using the relation $\exp(\mathrm{i}tH_{\mathrm{T}})|\psi_{0,f}\rangle = \exp(\mathrm{i}tE_{0,f})|\psi_{0,f}\rangle$. Applying the Heisenberg equation for the position operator[3],

$$[\mathbf{r}_i, H] = [\mathbf{r}_i, H_{\mathrm{T}}] = \mathrm{i}\frac{\partial \mathbf{r}_i}{\partial t} \to \mathbf{r}_i(t) = \exp(\mathrm{i}H_{\mathrm{T}})\mathbf{r}_i(0)\exp(-\mathrm{i}H_{\mathrm{T}}), \tag{C.7}$$

and using the completeness relation, $\sum_f |\psi_f\rangle\langle\psi_f| = 1$, one is led to another representation of the structure function,

$$W(\omega, q) = \int_{-\infty}^{+\infty} \frac{\mathrm{d}t}{2\pi} \exp(\mathrm{i}\omega t)\langle\psi_0| \sum_{i,j} F_i(q^2)F_j(q^2)\exp(\mathrm{i}\mathbf{q}\cdot[\mathbf{r}_j(t) - \mathbf{r}_i(0)]|\psi_0\rangle, \tag{C.8}$$

where instead of the knowledge of the final-state wave functions one demands the knowledge of the position operators' time evolution.

By using Heisenberg's equations once more, one is led to a representation of high symmetry[4],

$$\begin{aligned} W(\omega, q) = &\int_{-\infty}^{+\infty} \frac{\mathrm{d}t}{2\pi} \exp(\mathrm{i}\omega t) \sum_i \langle\psi_0|F_i(q^2)\exp(-\mathrm{i}\mathbf{q}\mathbf{r}_i)\exp[\mathrm{i}(E_0 - H_{\mathrm{T}})t] \\ &\times \sum_j F_j(q^2)\exp(\mathrm{i}\mathbf{q}\mathbf{r}_j)|\psi_0\rangle \end{aligned}. \tag{C.9}$$

This can be rewritten in momentum representation as

$$\begin{aligned} W(\omega, q) = &\int_{-\infty}^{+\infty} \frac{\mathrm{d}t}{2\pi} \exp(\mathrm{i}\omega t) \sum_{i,j} F_i(q^2)F_j(q^2) \\ &\times \int \frac{\mathrm{d}^3\mathbf{k}_1}{(2\pi)^3} \cdots \frac{\mathrm{d}^3\mathbf{k}_N}{(2\pi)^3} \langle\psi_0|\mathbf{k}_1, \ldots, \mathbf{k}_j + \mathbf{q}, \ldots, \mathbf{k}_N\rangle \\ &\times \langle\mathbf{k}_1 \ldots \mathbf{k}_N|\exp[\mathrm{i}(E_0 - H_{\mathrm{T}})t]|\mathbf{k}_1 \ldots \mathbf{k}_N\rangle\langle\mathbf{k}_1, \ldots, \mathbf{k}_i + \mathbf{q}, \ldots, \mathbf{k}_N|\psi_0\rangle \end{aligned} \tag{C.10}$$

[1]Written as a function of q^2 only, since the nucleon charge distributions, $\rho_i(\mathbf{r})$, are supposed to be radially symmetric.

[2]Reading

$$\delta(E_f - E_0 - \omega) = \int_{-\infty}^{\infty} \frac{\mathrm{d}t}{2\pi} \exp[-\mathrm{i}t(E_f - E_0 - \omega)].$$

[3]Here only the nucleon Hamiltonian, H_{T}, describing the nucleon's kinetic energy and the nucleon-nucleon interaction, plays a role since, by assumption of a Coulomb interaction potential, the other Hamilton operators commute with the nucleon positions, $\mathbf{r}_i$.

[4]Note that $F_i^*(q^2) = F_i(q^2)$ due to the assumed radial symmetry of the charge distribution.

Assuming that the nucleon-nucleon interaction is momentum independent and all particles have the same mass, M_N, one can evaluate the Hamilton operator,

$$H_\mathrm{T}\langle \mathbf{k}_1, \ldots, \mathbf{k}_i + \mathbf{q}, \ldots, \mathbf{k}_N|\psi_0\rangle = \left[E_0 + \frac{(\mathbf{k}_i + \mathbf{q})^2 - \mathbf{k}_i^2}{2M_N}\right] \langle \mathbf{k}_1, \ldots, \mathbf{k}_i + \mathbf{q}, \ldots, \mathbf{k}_N|\psi_0\rangle \tag{C.11}$$

and reduce the time integration to a δ function again. One thus obtains

$$\begin{aligned} W(\omega, q) = \sum_{i,j} F_i(q^2)F_j(q^2) \int \frac{\mathrm{d}^3\mathbf{k}_1}{(2\pi)^3} \cdots \frac{\mathrm{d}^3\mathbf{k}_N}{(2\pi)^3} \\ \times \langle \psi_0|\mathbf{k}_1, \ldots, \mathbf{k}_j + q, \ldots, \mathbf{k}_N\rangle \delta \left[\omega - \frac{(\mathbf{k}_i + \mathbf{q})^2 - \mathbf{k}_i^2}{2M_N}\right] \langle \mathbf{k}_1, \ldots, \mathbf{k}_i + \mathbf{q}, \ldots, \mathbf{k}_N|\psi_0\rangle. \end{aligned} \tag{C.12}$$

The δ function demands that in *every* term of the sum the energy loss be compensated by *one* nucleon picking up the momentum transfer. From now on, we focus on the diagonal terms of the sum[5] only. The structure function then reads

$$W(\omega, q) = \sum_i |F_i(q^2)|^2 \int \frac{\mathrm{d}^3\mathbf{k}_1}{(2\pi)^3} \cdots \frac{\mathrm{d}^3\mathbf{k}_N}{(2\pi)^3} |\langle \mathbf{k}_1 \ldots \mathbf{k}_N|\psi_0\rangle|^2 \delta \left[\omega - \frac{(\mathbf{k}_i + \mathbf{q})^2 - \mathbf{k}_i^2}{2M_N}\right]. \tag{C.13}$$

As pointed out before, the nucleus is supposed to be composed of independent particles. Thus, using normalized[6] wave functions, u_i, one can write the momentum-space representation of the ground state as

$$\langle \psi_0|\mathbf{k}_1 \ldots \mathbf{k}_N\rangle = \Pi_{i=1}^N u_i(\mathbf{k}_i). \tag{C.14}$$

One obtains, by using the fact that all integrals not containing the δ function reduce to 1, the following expression for the structure function

$$W(\omega, q) = \sum_i |F_i(q^2)|^2 \int \frac{\mathrm{d}^3\mathbf{k}_i}{(2\pi)^3} |u_i(\mathbf{k}_i)|^2 \delta \left[\omega - \frac{2\mathbf{k}_i\mathbf{q} + \mathbf{q}^2}{2M_N}\right]. \tag{C.15}$$

Finally, one can use the fact that all wave functions are supposed to be identical and given by $u(\mathbf{r}) = (\beta/2\pi)^{1/2} \exp(-\beta|\mathbf{r}|)/|\mathbf{r}|$. Their momentum-space representation then reads $u(\mathbf{k}) = (8\pi\beta)^{1/2}/(\mathbf{k}^2 + \beta^2)$. Integrating the δ function gives

$$W(\omega, q) = \sum_i |F_i(q^2)|^2 \frac{\beta M_N}{\pi q} \frac{1}{[(2M_N\omega - q^2)/2q]^2 + \beta^2}. \tag{C.16}$$

If one now also uses that the particles are supposed to be point-like, i.e., $\sum_i |F_i(q^2)|^2 = ZQ^2$, with charge $Q = 1$, and introduces the kinematical scaling variable

$$y = \frac{2M_N\omega - q^2}{2q}, \tag{C.17}$$

[5] For sufficiently large q, the non-diagonal terms can be shown to vanish, cf. discussion of Eq. (4.36) in Ref. [Wes75].

[6] With the normalization chosen such that $\int \frac{\mathrm{d}^3\mathbf{k}_i}{(2\pi)^3} |u_i(\mathbf{k}_i)|^2 = 1$.

one obtains

$$W(\omega, q) = Z \frac{M_N}{\pi q} \frac{\beta}{y^2 + \beta^2}, \tag{C.18}$$

which clearly peaks at $y = 0$, i.e, for the kinematics of the non-relativistic QEP, where $\omega_{\mathrm{QEP}}^{\mathrm{non-rel}} = q^2/(2M_N)$. To make the connection to the scaling behavior of the non-relativistic Fermi gas in Eq. (4.9), we interpret β as the only free scale and rewrite the fraction in Eq. (C.18) as

$$\frac{1}{\beta} \frac{1}{(y/\beta)^2 + 1}. \tag{C.19}$$

Expanding to first order in $(y/\beta)^2$ we find

$$W(\omega, q) = Z \frac{M_N}{\pi q \beta} \left\{ 1 - \left(\frac{y}{\beta} \right)^2 + \mathcal{O} \left[\left(\frac{y}{\beta} \right)^4 \right] \right\}, \tag{C.20}$$

an expression for the response surprisingly similar to Eq. (4.9).

The appearance of y itself is, however, not very surprising, since y enters during the integration within Eq. (C.15) as the value of the longitudinal momentum, k_z, demanded by energy conservation. The underlying origin of the scaling function is the same energy-conservation condition as in Eq. (4.6).

We conclude with a summary of the derivation: Starting with certain assumptions about the interaction as well as the electron- and nucleus-wave functions, one is able to show that the non-trivial part of the electron-nucleus cross section depends strongly on one-nucleon knockout kinematics. It is noteworthy that here a general expression for the electron-nucleus cross section has been the starting point, while all the approaches presented in Chapter 4 start out with the one-nucleon-knockout scenario and aim to describe the response in the kinematical region around the quasi-elastic peak.

C.2 Scaling in plane-wave impulse approximation

In Eq. (4.18) we have presented the PWIA scaling variable, y. As an analog to Eq. (4.38), we can introduce its dimensionless counterpart, $\Upsilon = y/k_{\mathrm{F}}$, and also perform a superscaling analysis. In the context of the derivation of Eq. (4.38), we have already discussed that the variables y_ψ and y take on similar values in the kinematical region of the QEP. It is an experimental finding, cf. e.g. Ref. [DS99], that the dimensionless PWIA-scaling functions, $f = k_{\mathrm{F}} F$, also satisfy superscaling.

Using de Forest's off-shell prescription [DF83], described in Appendix D.1, we perform a y-scaling analysis on our simulated cross sections. As one can see from Fig. C.1c, the violation of second-kind scaling, namely a spread in the scaling functions at $\Upsilon, \psi' > -0.5$, already seen in Fig. 6.3c, persists. In addition, we see a general lowering of the response as now the curve for ^{12}C (dotted line) fits the data at the QEP, whereas in Fig. C.1c it overshoots the data. We consider this to be an effect of differing parameters in the computation of the off-shell cross sections. In our computation the values $M_A(^{12}\mathrm{C}) = 11.178$ GeV and $M_{A-1}^0(^{11}\mathrm{B}) = 10.255$ GeV ($M_A(^{197}\mathrm{Au}) = 183.473$ GeV and $M_{A-1}^0(^{196}\mathrm{Pt}) = 182.540$ GeV respectively), according to Ref. [WAT03], are used. In addition, we apply the nucleon form factors from Sec. 2.3.2.

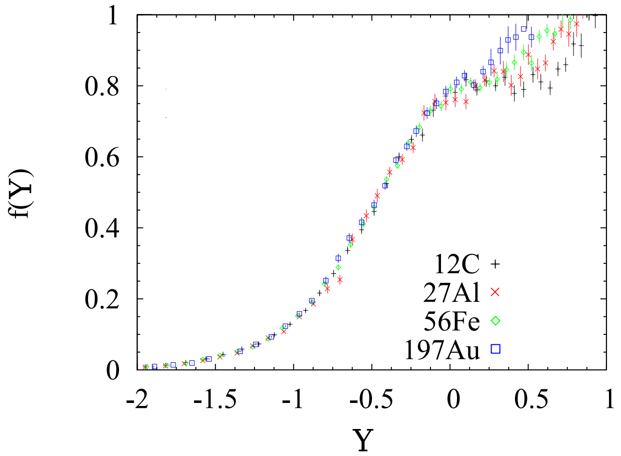

(a) Experimental PWIA scaling functions, $f = k_{\mathrm{F}} F$, with data taken from the world data analysis in Ref. [DS99].

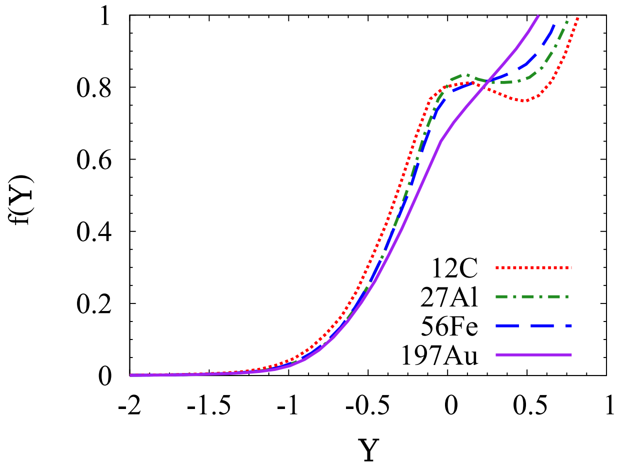

(b) GiBUU simulation of PWIA scaling functions.

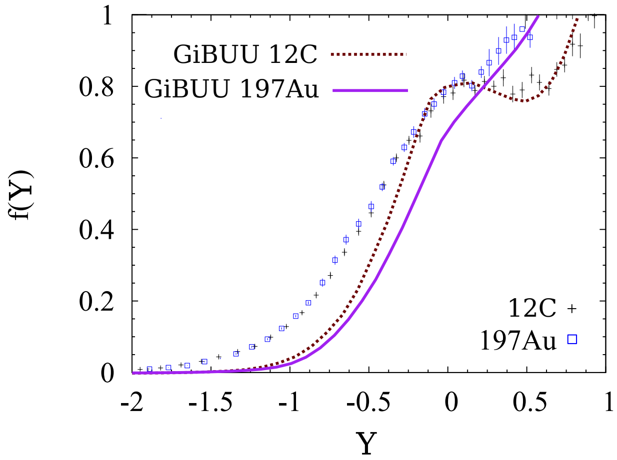

(c) Comparison of data in Fig. (a) with the scaling function for calcium and gold from Fig. (b).

Figure C.1: Second-kind scaling analysis of dimensionless PWIA scaling functions f vs. the corresponding scaling variable, Υ, for electron scattering on ^{12}C, ^{27}Al, ^{56}Fe and ^{197}Au at a constant momentum transfer of q=1.0 GeV and incoming electron energy of 3.6 GeV.

C.3 Scaling of Δ-excitation responses

In Sec. 4.7, we have already pointed out that methods have been developed to apply superscaling techniques to kinematical regions associated with the Δ excitation. Let us state the most important steps of this approach, following the formalism in Ref. [MAB+09]. It is our aim to analyse the non-quasielastic contributions to the cross section, $\mathrm{d}\sigma/\mathrm{d}\Omega_{k'}\mathrm{d}k^{0\prime}$. In the original approach, the QE contribution in the $\psi' > 0$ region is estimated by means of a superscaling extrapolation, meaning that an experimentally motivated scaling function is multiplied with the single-nucleon contributions. When analyzing the GiBUU response this step can be omitted, since the code allows for switching off QE and BG contributions.

Now we will follow the general steps of the scaling analysis, described in Sec. 4.1. Starting from the RFG picture, the scaling variable can be calculated to be [MAB+09]

$$\psi_\Delta = \frac{1}{\sqrt{\epsilon_\mathrm{F} - 1}} \frac{\lambda - \tau\rho_\Delta}{\sqrt{(1+\lambda\rho_\Delta)\tau + \kappa\sqrt{\tau(1+\tau\rho_\Delta^2)}}} \tag{C.21}$$

with the scaled variables introduced in Eq. (4.32) and the following variables accounting for the larger mass of the Δ resonance[7]:

$$\mu_\Delta = \frac{m_\Delta}{M_N}, \quad \rho_\Delta = 1 + \frac{\mu_\Delta^2 - 4\tau}{4\tau}. \tag{C.22}$$

The scaling function can then be obtained through dividing the non-quasielastic cross section by the single-nucleon contributions,

$$f^{\mathrm{non-QE}}(\psi_\Delta) = k_\mathrm{F} \frac{\left(\frac{\mathrm{d}\sigma}{\mathrm{d}\Omega_{k'}\mathrm{d}k^{0\prime}}\right)^{\mathrm{non-QE}}}{\left(\frac{\mathrm{d}\sigma}{\mathrm{d}\Omega_{k'}}\right)_{\mathrm{Mott}} (v_\mathrm{L} G_\mathrm{L}^\Delta + v_\mathrm{T} G_\mathrm{T}^\Delta)}, \tag{C.23}$$

similar to Eq. (4.57). Due to the different spinor structure of the spin-3/2 final state, the single-nucleon contributions take on a more complicated form[8]

$$G_L^\Delta = \frac{\kappa}{4\tau} A\left[(1+\tau\rho_\Delta^2+1)w_2^\Delta - w_1^\Delta\right], \tag{C.24}$$

$$G_T^\Delta = \frac{1}{2\kappa} A w_1^\Delta, \tag{C.25}$$

with

$$w_1^\Delta = \frac{1}{2}(\mu_\Delta+1)^2(2\tau\rho_\Delta + 1 - \mu_\Delta)(G_{\mathrm{M,p}}^2 + 3G_{\mathrm{E,n}}^2), \tag{C.26}$$

$$w_2^\Delta = (\mu_\Delta+1)^2 \frac{2\tau\rho_\Delta + 1 - \mu_\Delta}{1+\tau\rho_\Delta} G_{\mathrm{M,p}}^2 + 3G_{\mathrm{E,n}}^2 + 4\frac{\tau}{\mu_\Delta^2} G_{\mathrm{C}\Delta}^2. \tag{C.27}$$

[7] Here we follow the approach of Ref. [MAB+09], while in Refs. [MDS02, ABC+99, ABC+05] $\rho_\Delta = 1 + (\mu_\Delta^2 - 1)/(4\tau)$ is used instead.

[8] Note that when comparing the single-nucleon responses, e.g. G_T, in Ref. [MAB+09] with the ones in Ref. [ABC+05] we find several differences, the most evident being an overall factor 4. Also when comparing Eq. (20) of Ref. [MAB+09] to Eq. (76) of the original derivation [ABC+99], we find a factor of 2 difference.

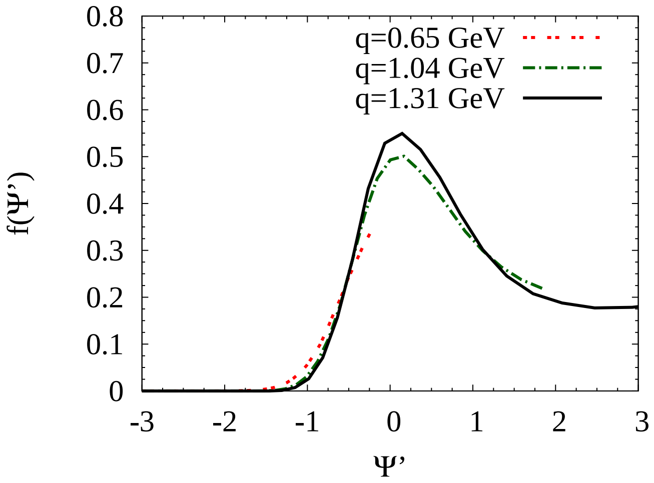

Figure C.2: First-kind scaling analysis of GiBUU simulated Δ excitation data for electron scattering on ^{12}C at momentum transfers, q, of 0.65, 1.04 and 1.31 GeV and incoming energies of 0.55 and 3.6 GeV. Note, that the curve for $q = 0.65$ GeV does not span the entire range of ψ' due to kinematical restrictions.

While in other analyses we have used the form factors given in Sec. 2.3.2, here we apply the parameterization of Ref. [MAB$^+$09] for $G_{\mathrm{E,n}}, G_{\mathrm{M,p}}$ and $G_{\mathrm{C}\Delta}$.

When implementing the approach described above, as well as the one from Ref. [ABC$^+$05] and the one given by Eqs. (77) and (78) in Ref. [ABC$^+$99], we have found scaling functions with shapes similar to those obtained from QE scattering and reasonable scaling behavior following the implementation in Ref. [ABC$^+$05]. However, the absolute values differ strongly and, as the literature on this topic is limited and exhibits some inconsistencies (cf. footnotes in this section), we have not been able to resolve the differences in the scope of this work. Hence, in Figs. C.2 and C.3 we present scaling functions, obtained by multiplying the GiBUU scaling functions by a fixed value, so that the experimental values are reproduced. If Fig. C.3, we find that second-kind scaling is slightly broken. As the deviations strongly resemble those already seen for electron scattering in Sec. 6.1.1, we consider that the same mechanism, i.e., a coupling of density and momentum in the LTF ansatz, is to be held accountable. First-kind scaling is to some degree observed in C.2, while not being as good as for electron scattering. We assume this to be a consequence of the fact that the original derivation [ABC$^+$99] includes the limit of small Fermi momenta[9] and is hence not an exact description of the response. It should also be noted that the form factors used in the aforementioned studies on this topic differ from the ones introduced in Sec. 2.4.3 and used in our simulation.

[9]Confer the derivation of Eq. (71) therein.

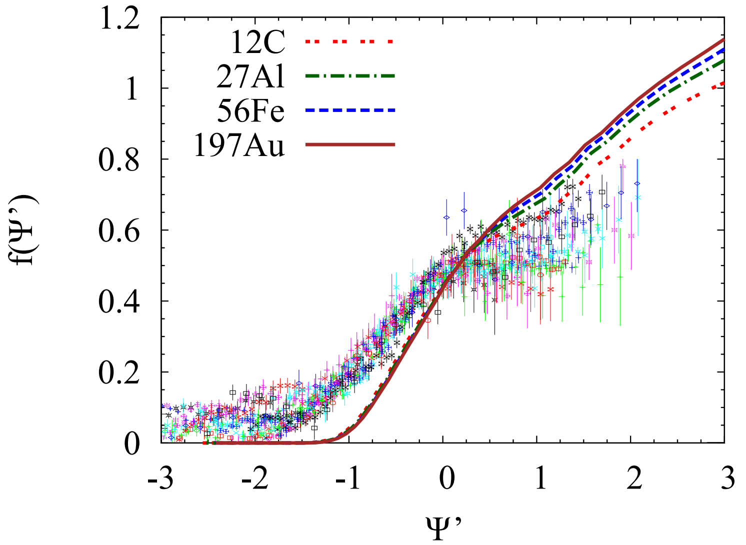

Figure C.3: Second-kind scaling analysis of GiBUU simulated Δ excitation data for electron scattering on ^{12}C, ^{27}Al, ^{56}Fe and ^{197}Au at a constant momentum transfer of q=1 GeV and incoming electron energy of 3.6 GeV.

Appendix D

Additional formulae

D.1 De Forest's cc1 prescription

In his original work [DF83] de Forest introduces an extrapolation of Eq. (2.41) for the off-shell case by modifying the term that involves $\sigma^{\mu\nu}$. With this extrapolation he derives an off-shell prescription for the single-nucleon cross section. He admits, however, that the extrapolation is not based on a fundamental theory and hence not unambiguous, so that he actually presents two possibilities. Here, we will describe the one referred to as σ^{cc1}.

Since we only make use of the off-shell prescription in order to perform the PWIA scaling analysis in Sec. C.2, we do not write the cross section in the original form but instead in the one given in the appendix of Ref. [DS99]. There, the single-nucleon off-shell cross section reads

$$\sigma_{eN}(q,\omega;p,\mathcal{E}) = \left(\frac{\mathrm{d}\sigma}{\mathrm{d}\Omega_{k'}}\right)_{\mathrm{Mott}} \left(v_{\mathrm{L}}\tilde{w}_{\mathrm{L}} + v_{\mathrm{T}}\tilde{w}_{\mathrm{T}}\right), \tag{D.1}$$

where all quantities except the off-shell responses, $\tilde{w}_{\mathrm{L}}$ and $\tilde{w}_{\mathrm{T}}$, are already known from the previous chapters[1]. We will express these factors by means of the scaled variables introduced in Eq. (4.32) and the newly defined quantities [DS99]

$$\begin{aligned}
E_N &= \left[(\mathbf{q}+\mathbf{p})^2 + M_N^2\right]^{1/2}, \\
\bar{E} &= (M_N^2 + p^2)^{1/2}, \\
\bar{\lambda} &= \frac{\bar{\omega}}{2M_N} = \frac{E_N - \bar{E}}{2M_N}, \\
\bar{\tau} &= \kappa^2 - \bar{\lambda}^2, \\
\eta &= \frac{p}{M_N}, \\
\delta^2 &= \frac{\bar{\tau}}{\kappa^2}\left(\frac{E_N + \bar{E}}{2M_N}\right)^2 - (1+\bar{\tau}).
\end{aligned} \tag{D.2}$$

Note that, due to fixing the excitation energy, ω and q are not independent anymore and

[1] The excitation energy, $\mathcal{E}$, is known from Eq. (4.21). The kinematical factors $v_{\mathrm{L,T}}$ were introduced in Eq. (4.45).

inserting Eq. (4.21) into Eq. (4.14) one obtains

$$\omega = E_N - M_A^0 + \sqrt{(M_{A-1}^0)^2 + p^2} + \mathcal{E}. \tag{D.3}$$

Leading to an explicit dependence on the experimentally observed masses.

As one is interested in the single-*nucleon* cross section, an isospin average has to be performed on the Sachs form factors resulting in the quantities

$$\begin{aligned} \tilde{G}_{\mathrm{E}}^2(\tau) &\equiv ZG_{\mathrm{Ep}}^2 + NG_{\mathrm{En}}^2, \\ \tilde{G}_{\mathrm{M}}^2(\tau) &\equiv ZG_{\mathrm{Mp}}^2 + NG_{\mathrm{Mn}}^2, \\ \Delta\tilde{G}(\tau) &\equiv ZG_{\mathrm{Ep}}G_{\mathrm{Mp}} + NG_{\mathrm{En}}G_{\mathrm{Mn}}. \end{aligned} \tag{D.4}$$

This also implicates a modification of the Dirac and Pauli form factors (referred to as F_1, F_2 in Sec. 2.3.2).

$$\begin{aligned} \tilde{W}_1(\tau) &\equiv \tau\tilde{G}_{\mathrm{M}}^2, \\ \tilde{W}_2(\tau) &\equiv \frac{1}{1+\tau}(\tilde{G}_{\mathrm{E}}^2 + \tilde{G}_{\mathrm{M}}^2), \\ \Delta\tilde{W}_1(\tau,\bar{\tau}) &\equiv \frac{\tau-\bar{\tau}}{(1+\tau)^2}(\tilde{G}_{\mathrm{E}}^2 + \tilde{G}_{\mathrm{M}}^2 - 2\Delta\tilde{G}), \\ \Delta\tilde{W}_2(\tau,\bar{\tau}) &\equiv \frac{\tau-\bar{\tau}}{(1+\tau)^2}(\tilde{G}_{\mathrm{E}}^2 + \tilde{G}_{\mathrm{M}}^2). \end{aligned} \tag{D.5}$$

Finally, the off-shell responses of the nucleon read

$$\begin{aligned} \tilde{w}_1(q,\omega;p,\mathcal{E}) &= \frac{1}{2\kappa\sqrt{1+\eta^2}}\left(\frac{\kappa^2}{\bar{\tau}}\right)\left[\tilde{G}_{\mathrm{E}}^2 + \delta^2(\tilde{W}_2 + \Delta\tilde{W}_1) + (1+\bar{\tau})\Delta\tilde{W}_1 + (1+\tau)\Delta\tilde{W}_2\right] \\ \tilde{w}_2(q,\omega;p,\mathcal{E}) &= \frac{1}{2\kappa\sqrt{1+\eta^2}}\left[2\bar{\tau}\tilde{G}_{\mathrm{E}}^2 + \delta^2(\tilde{W}_2 + \Delta\tilde{W}_1)\right]. \end{aligned} \tag{D.6}$$

D.2 Kinematics of the Vacuum QEP

D.2.1 Non-relativistic kinematics

When considering small momentum transfers, $q \ll M_N$, the non-relativistic approximation for the kinetic energy of the nucleon is justified. Energy conservation leads to

$$\omega = E'_{\mathrm{kin}} - E_{\mathrm{kin}} \to \omega_{\mathrm{QEP}} = \frac{q^2}{2M_N} - 0. \tag{D.7}$$

Consequently, the four-momentum transfer is given by

$$Q^2 = q^2 - \frac{q^4}{4M_N^2}. \tag{D.8}$$

Still using the ultra-relativistic approximation for the electron,

$$Q^2 = 2k^0k^{0\prime}(1-\cos\theta), \tag{D.9}$$

one obtains the following relation for the momentum transfer as a function of incoming energy and scattering angle

$$q^2 = 2M_N \left[M_N + k^0(1-\cos\theta) - \sqrt{[M_N + k^0(1-\cos\theta)]^2 - 2k^{0 2}(1-\cos\theta)} \right]. \quad \text{(D.10)}$$

D.2.2 Relativistic kinematics

In the relativistic case, energy conservation at the QEP reads

$$\omega_{\text{QEP}} = \sqrt{M_N^2 + q^2} - M_N. \quad \text{(D.11)}$$

Consequently

$$q^2_{\text{QEP}} = \omega^2_{\text{QEP}} + 2\omega_{\text{QEP}} M_N \quad \text{(D.12)}$$

and

$$Q^2_{\text{QEP}} = 2M_N \omega_{\text{QEP}}. \quad \text{(D.13)}$$

Starting again with the ultra-relativistic expression for the four-momentum transfer, Eq. (D.9), one can relate the three momentum transfer to incoming energy and scattering angle via

$$q^2 = \left(\frac{M_N^2 + (1-\cos\theta)(k^{0 2} + k^0 M_N)}{M_N + k^0(1-\cos\theta)} \right)^2 - M_N^2. \quad \text{(D.14)}$$

D.3 In-medium shift of ψ at the QEP

Let us now translate the above equations into the scaled variables introduced in Eq. (4.32). First of all, as

$$\lambda_{\text{QEP}} = \frac{Q^2}{4M_N^2} = \tau_{\text{QEP}}, \quad \text{(D.15)}$$

the vacuum scaling variable,

$$\psi = \frac{1}{\sqrt{\varepsilon_{\text{F}} - 1}} \frac{\lambda - \tau}{\sqrt{(1+\lambda)\tau + \kappa\sqrt{\tau(\tau+1)}}}, \quad \text{(D.16)}$$

takes on the value 0 at the vacuum QEP. To account for the observed shift of the QEP, one introduces an in-medium energy shift, E_{shift}, leading to the following modifications

$$\lambda' = \frac{\omega - E_{\text{shift}}}{2M_N} = \lambda - \Delta\lambda \quad \text{(D.17)}$$

and

$$\tau' = \kappa^2 - \lambda^2 = \kappa^2 - \lambda^2 + 2\lambda\Delta\lambda - \Delta\lambda^2 = \tau + 2\lambda\Delta\lambda - \Delta\lambda^2. \quad \text{(D.18)}$$

These quantities have to be inserted in Eq. (D.16) in place of λ and τ in order to obtain the shifted scaling variable ψ'. With vacuum-QEP kinematics,

$$\begin{aligned} \tau_{\text{QEP}} &= \kappa^2 - \lambda^2_{\text{QEP}} = \kappa^2 - \tau^2_{\text{QEP}}, \\ \tau_{\text{QEP}} &= \sqrt{\frac{1}{4} + \kappa^2} - \frac{1}{2}, \end{aligned} \quad \text{(D.19)}$$

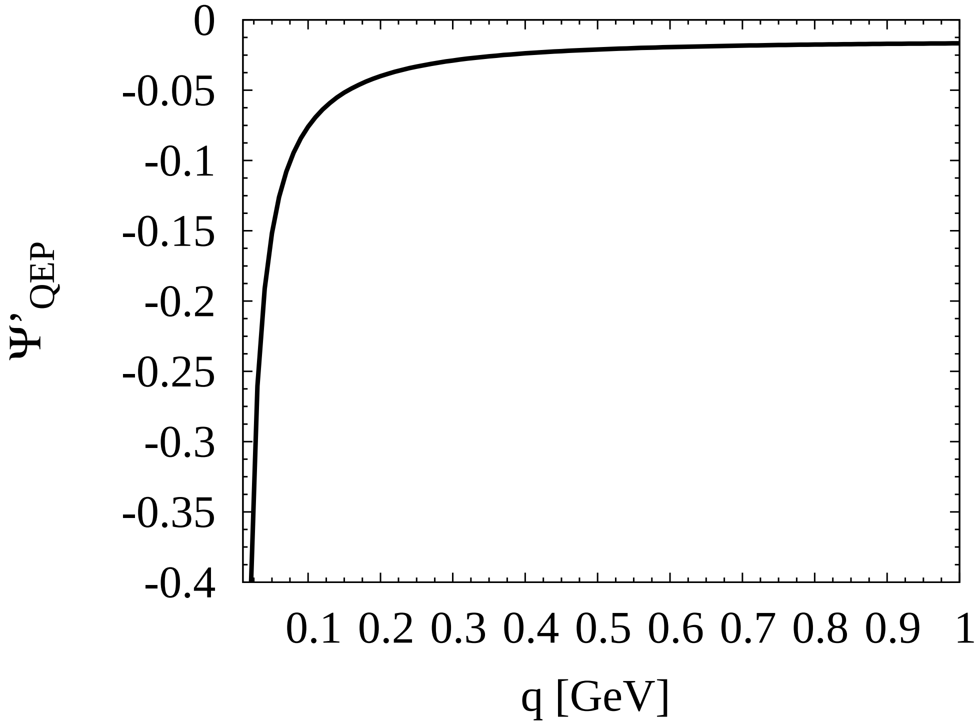

Figure D.1: Value of the shifted scaling variable, ψ' at the vacuum QEP (solid line) as a function of q, calculated with the canonical value of $\delta\lambda = 0.0107$, corresponding to $E_{\text{shift}} = 0.02$ GeV.

it is possible to write $\psi'_{\text{QEP}} = \psi'(\kappa, \omega' = \omega'_{\text{QEP,vac}})$ as a function of κ only:

$$
\begin{aligned}
\psi'_{\text{QEP}} = &- \left[\left(2\sqrt{\kappa^2 + \frac{1}{4}} - 1 \right) \Delta\lambda - (\Delta\lambda)^2 + \Delta\lambda \right] \\
&\times \left\{ -\frac{1}{4} \left(2\Delta\lambda - 2\sqrt{\kappa^2 + \frac{1}{4}} - 1 \right) \left[2 \left(2\sqrt{\kappa^2 + \frac{1}{4}} - 1 \right) \Delta\lambda + 2\sqrt{\kappa^2 + \frac{1}{4}} - 2(\Delta\lambda)^2 - 1 \right] \right. \\
&+ \frac{1}{2} \left[\left(2 \left(2\sqrt{\kappa^2 + \frac{1}{4}} - 1 \right) \Delta\lambda + 2\sqrt{\kappa^2 + \frac{1}{4}} - 2(\Delta\lambda)^2 - 1 \right) \right. \\
&\times \left. \left. \left(2 \left(2\sqrt{\kappa^2 + \frac{1}{4}} - 1 \right) \Delta\lambda + 2\sqrt{\kappa^2 + \frac{1}{4}} - 2(\Delta\lambda)^2 + 1 \right) \right]^{-1/2} \kappa \right\}^{-1/2}
\end{aligned}
\tag{D.20}
$$

Contrary to the non-relativistic case mentioned in the discussion of first-kind scaling in Sec. 6.1.1, it is not easy to see that $\psi' \approx -\text{const}/\kappa$. But when plotting the function, as done in Fig. D.1, this behavior is clearly observed.

Bibliography

[A+96] M. Anghinolfi et al., *Quasi-elastic and inelastic inclusive electron scattering from an oxygen jet target*, Nuclear Physics A **602** (1996), no. 3-4, 405–422.

[A+08] Claude Amsler et al., *Review of particle physics*, Phys. Lett. **B667** (2008), 1–.

[AA+08] A. A. Aguilar-Arevalo et al., *Measurement of muon neutrino quasielastic scattering on carbon*, Phys. Rev. Lett. **100** (2008), no. 3, 032301.

[AA+10] ———, *First measurement of the muon neutrino charged current quasielastic double differential cross section*, Phys. Rev. **D81** (2010), 092005.

[AAA+01] Q. R. Ahmad, R. C. Allen, T. C. Andersen, J. D. Anglin, G. Buehler, J. C. Barton, E. W. Beier, M. Bercovitch, J. Bigu, S. Biller, et al., *Measurement of the rate of $\nu_e + d \to p + p + e^-$ interactions produced by ^{8}B solar neutrinos at the sudbury neutrino observatory*, Physical Review Letters **87** (2001), no. 7, 71301.

[ABB+97] W. M. Alberico, M. B. Barbaro, S. M. Bilenky, J. A. Caballero, C. Giunti, C. Maieron, E. Moya de Guerra, and J. M. Udias, *Inelastic ν and $\bar{\nu}$ scattering on nuclei and "strangeness" of the nucleon*, Nuclear Physics A **623** (1997), no. 3-4, 471–497.

[ABC+99] J. E. Amaro, M. B. Barbaro, J. A. Caballero, T. W. Donnelly, and A. Molinari, *Relativistic effects in electromagnetic nuclear responses in the quasi-elastic delta region*, Nuclear Physics A **657** (1999), no. 2, 161–186.

[ABC+05] J. E. Amaro, M. B. Barbaro, J. A. Caballero, T. W. Donnelly, A. Molinari, and I. Sick, *Using electron scattering superscaling to predict charge-changing neutrino cross sections in nuclei*, Physical Review C **71** (2005), no. 1, 15501.

[ABC+07] J. E. Amaro, M. B. Barbaro, J. A. Caballero, T. W. Donnelly, and J. M. Udias, *Final-state interactions and superscaling in the semi-relativistic approach to quasielastic electron and neutrino scattering*, Physical Review C **75** (2007), no. 3, 34613.

[ABC+10a] J. E. Amaro, M. B. Barbaro, J. A. Caballero, T. W. Donnelly, C. Maieron, and J. M. Udias, *Meson-exchange currents and final-state interactions in* *quasielastic electron scattering at high momentum transfers*, Physical Review C **81** (2010), no. 1, 14606.

[ABC+10b] J. E. Amaro, M. B. Barbaro, J. A. Caballero, T. W. Donnelly, and C. F. Williamson, *Meson-exchange currents and quasielastic neutrino cross sections in the superscaling approximation model*, arXiv:nucl-th/1010.1708 (2010).

[ABCD06] J. E. Amaro, M. B. Barbaro, J. A. Caballero, and T. W. Donnelly, *Superscaling and neutral current quasielastic neutrino-nucleus scattering*, Physical Review C **73** (2006), no. 3, 35503.

[ABF10] Artur M. Ankowski, Omar Benhar, and Nicola Farina, *Analysis of the q^2-dependence of charged-current quasielastic processes in neutrino-nucleus interactions*, arXiv:nucl-th/1001.0481 (2010).

[ACD+80] R. Altemus, A. Cafolla, D. Day, J. S. McCarthy, R. R. Whitney, and J. E. Wise, *Longitudinal and transverse inelastic electron scattering from ^{56}Fe*, Physical Review Letters **44** (1980), no. 15, 965–968.

[Adl68] Stephen L. Adler, *Photo-, electro-, and weak single-pion production in the (3,3) resonance region*, Annals of Physics **50** (1968), no. 2, 189–311.

[AGK+04] A. N. Antonov, M. K. Gaidarov, D. N. Kadrev, M. V. Ivanov, E. Moya de Guerra, and J. M. Udias, *Superscaling in nuclei: A search for a scaling function beyond the relativistic Fermi gas model*, Physical Review C **69** (2004), no. 4, 44321.

[AK10] E. K. Akhmedov and J. Kopp, *Neutrino oscillations: Quantum mechanics vs. quantum field theory*, Journal of High Energy Physics **2010** (2010), no. 4, 1–41.

[AM09] C. C. Atti and C. B. Mezzetti, *Obtaining information on short range correlations from inclusive electron scattering*, Physical Review C **79** (2009), no. 5, 51302.

[AMB+10] J. E. Amaro, C. Maieron, M. B. Barbaro, J. A. Caballero, and T. W. Donnelly, *Pionic correlations and meson-exchange currents in two-particle emission induced by electron scattering*, arXiv:1008.0753 (2010).

[AMD+88] W. M. Alberico, A. Molinari, T. W. Donnelly, E. L. Kronenberg, and J. W. Van Orden, *Scaling in electron scattering from a relativistic Fermi gas*, Physical Review C **38** (1988), no. 4, 1801–1810.

[ARC+95] M. Anghinolfi, M. Ripani, R. Cenni, P. Corvisiero, A. Longhi, L. Mazzaschi, V. Mokeev, G. Ricco, M. Taiuti, A. Teglia, et al., *Inclusive electron scattering from an oxygen and argon jet target*, Journal of Physics G: Nuclear and Particle Physics **21** (1995), L9.

[B$^+$77] S. J. Barish et al., *Study of neutrino interactions in hydrogen and deuterium: Description of the experiment and study of the reaction $\nu + d \to \mu^- + p + p$*, Phys. Rev. D **16** (1977), no. 11, 3103–3121.

[BABB08] A. Bodek, S. Avvakumov, R. Bradford, and Howard Scott Budd, *Vector and axial nucleon form factors:a duality constrained parameterization*, Eur. Phys. J. **C53** (2008), 349–354.

[BBCM86] W. Bauer, G. F. Bertsch, W. Cassing, and U. Mosel, *Energetic photons from intermediate energy proton-and heavy-ion-induced reactions*, Physical Review C **34** (1986), no. 6, 2127–2133.

[BCBH07] D. Barquilla-Cano, A. J. Buchmann, and E. Hernandez, *Axial $N \to \Delta$ (1232) and $N \to N^*$(1440) transition form factors*, Physical Review C **75** (2007), no. 6, 65203.

[BCDM08] M. B. Barbaro, R. Cenni, T. W. Donnelly, and A. Molinari, *Model for BCS-type correlations in superscaling*, Physical Review C **78** (2008), no. 2, 24602.

[BCDP$^+$98] M. B. Barbaro, R. Cenni, A. De Pace, T. W. Donnelly, and A. Molinari, *Relativistic y-scaling and the Coulomb sum rule in nuclei*, Nuclear Physics A **643** (1998), no. 2, 137–160.

[BDK$^+$68] W. Bartel, B. Dudelzak, H. Krehbiel, J. McElroy, U. Meyer-Berkhout, W. Schmidt, V. Walther, and G. Weber, *Electroproduction of pions near the Δ(1236) isobar and the form factor $G^M(q^2)$ of the $(\gamma N, \Delta)$-vertex*, Physics Letters B **28** (1968), no. 2, 148–151.

[BDS08] Omar Benhar, Donal Day, and Ingo Sick, *Inclusive quasielastic electron-nucleus scattering*, Rev. Mod. Phys. **80** (2008), no. 1, 189–224.

[BDW67] F. A. Berends, A. Donnachie, and D. L. Weaver, *Photoproduction and electroproduction of pions (i) dispersion relation theory*, Nuclear Physics B **4** (1967), no. 1, 1–53.

[BEM02] Veronique Bernard, Latifa Elouadrhiri, and Ulf. G. Meissner, *Axial structure of the nucleon*, J. Phys. **G28** (2002), 1.

[BFF89] O. Benhar, A. Fabrocini, and S. Fantoni, *The nucleon spectral function in nuclear matter*, Nuclear Physics A **505** (1989), 267–299.

[BFN$^+$05] O. Benhar, N. Farina, H. Nakamura, M. Sakuda, and R. Seki, *Electron-and neutrino-nucleus scattering in the impulse approximation regime*, Physical Review D **72** (2005), no. 5, 53005.

[BGPR96] S. Boffi, C. Giusti, F. D. Pascati, and M. Radici, *Electromagnetic response of atomic nuclei*, Oxford University Press, USA, 1996.

[BK73] E. Byckling and K. Kajantie, *Particle kinematics*, Wiley London, 1973.

[BL04] V. D. Burkert and T. S. H. Lee, *Electromagnetic meson production in the nucleon resonance region*, International Journal of Modern Physics E **13** (2004), no. 6, 1035–1111.

[BLMAR07] O. Buss, T. Leitner, U. Mosel, and L. Alvarez-Ruso, *Influence of the nuclear medium on inclusive electron and neutrino scattering off nuclei*, Physical Review C **76** (2007), no. 3, 35502.

[BP69] J. D. Bjorken and E. A. Paschos, *Inelastic electron-proton and γ-proton scattering and the structure of the nucleon*, Physical Review **185** (1969), no. 5, 1975–1982.

[BPP93] O. Benhar, V. R. Pandharipande, and S. C. Pieper, *Electron-scattering studies of correlations in nuclei*, Reviews of Modern Physics **65** (1993), no. 3, 817–828.

[Bus08] O. Buss, *Photon- and pion-induced nuclear reactions in a transport approach*, Ph.D. thesis, Justus-Liebig-Universitaet Giessen, 2008, available online at http://theorie.physik.uni-giessen.de.

[CAB$^+$05] J. A. Caballero, J. E. Amaro, M. B. Barbaro, T. W. Donnelly, C. Maieron, and J. M. Udias, *Superscaling in charged current neutrino quasielastic scattering in the relativistic impulse approximation*, Physical Review Letters **95** (2005), no. 25, 252502.

[CBA$^+$10] J. A. Caballero, M. B. Barbaro, A. N. Antonov, M. V. Ivanov, and T. W. Donnelly, *Scaling function and nucleon momentum distribution*, Physical Review C **81** (2010), no. 5, 55502.

[CdAPS91] C. Ciofi degli Atti, E. Pace, and G. Salme, *y-scaling analysis of quasielastic electron scattering and nucleon momentum distributions in few-body systems, complex nuclei, and nuclear matter*, Physical Review C **43** (1991), no. 3, 1155–1176.

[CDM97] R. Cenni, T. W. Donnelly, and A. Molinari, *Relativistic electromagnetic charge response: Finite versus infinite systems, exclusive versus inclusive processes*, Physical Review C **56** (1997), no. 1, 276–291.

[CG63] W. Czy and K. Gottfried, *Inelastic electron scattering from fluctuations in the nuclear charge distribution*, Annals of Physics **21** (1963), no. 1, 47–71.

[Cla79] J. W. Clark, *Variational theory of nuclear matter*, Progress in particle and nuclear physics **2** (1979), 89–199.

[CMHU10] J. A. Caballero, M. C. Martinez, J. L. Herraiz, and J. M. Udias, *Superscaling analysis of the Coulomb Sum Rule in quasielastic electron-nucleus scattering*, Physics Letters B (2010).

[Dan84] P. Danielewicz, *Quantum theory of nonequilibrium processes, I*, Annals of Physics **152** (1984), no. 2, 239–304.

[DEK76] R. C. E. Devenish, T. S. Eisenschitz, and J. G. Körner, *Electromagnetic $N-N^*$ transition form factors*, Phys. Rev. D **14** (1976), no. 11, 3063–3078.

[DF83] T. De Forest, *Off-shell electron-nucleon cross sections the impulse approximation*, Nuclear Physics, Section A **392** (1983), no. 2-3, 232–248.

[dFW66] T. de Forest and J. D. Walecka, *Electron scattering and nuclear structure*, Advances in Physics **15** (1966), no. 57, 1–109.

[DHKT99] D. Drechsel, O. Hanstein, S. S. Kamalov, and L. Tiator, *A unitary isobar model for pion photo- and electroproduction on the proton up to 1 GeV*, Nuclear Physics A **645** (1999), no. 1, 145–174.

[DJDVDV74] C. W. De Jager, H. De Vries, and C. De Vries, *Nuclear charge-and magnetization-density-distribution parameters from elastic electron scattering*, Atomic Data and Nuclear Data Tables **14** (1974), no. 5-6, 479–508.

[DMDS90] D. B. Day, J. S. McCarthy, T. W. Donnelly, and I. Sick, *Scaling in inclusive electron-nucleus scattering*, Annual Review of Nuclear and Particle Science **40** (1990), no. 1, 357–410.

[DMM$^+$87] D. B. Day, J. S. McCarthy, Z. E. Meziani, R. Minehart, R. Sealock, S. T. Thornton, J. Jourdan, I. Sick, B. W. Filippone, R. D. McKeown, et al., *y scaling in electron-nucleus scattering*, Physical Review Letters **59** (1987), no. 4, 427–430.

[DPNA$^+$04] A. De Pace, M. Nardi, W. M. Alberico, T. W. Donnelly, and A. Molinari, *Role of 2p-2h MEC excitations in superscaling*, Nuclear Physics A **741** (2004), 249–269.

[DPR04] P. Degond, L. Pareschi, and G. Russo, *Modeling and computational methods for kinetic equations*, Birkhauser, 2004.

[DS99] T. W. Donnelly and I. Sick, *Superscaling of inclusive electron scattering from nuclei*, Physical Review C **60** (1999), no. 6, 65502.

[DST$^+$04] D. Drakoulakos, P. Stamoulis, G. Tzanakos, M. Zois, D. Casper, J. Dunmore, C. Regis, B. Ziemer, E. Paschos, D. Boehnlein, et al., *MINERνA collaboration*, arXiv:hep-ex/0405002 (2004).

[DT92] D. Dreschsel and L. Tiator, *Threshold pion photoproduction on nucleons*, Journal of Physics G: Nuclear and Particle Physics **18** (1992), 449.

[DY57] R. H. Dalitz and D. R. Yennie, *Pion production in electron-proton collisions*, Phys. Rev. **105** (1957), no. 5, 1598–1615.

[ECM$^+$94] A. Engel, W. Cassing, U. Mosel, M. Schaefer, and G. Wolf, *Pion-nucleus reactions in a microscopic transport model*, Nuclear Physics A **572** (1994), no. 3-4, 657–681.

[EWE88] T. Ericson, W. Weise, and T. E. O. Ericson, *Pions and nuclei*, Clarendon, 1988.

[Fab97] A. Fabrocini, *Inclusive transverse response of nuclear matter*, Physical Review C **55** (1997), no. 1, 338–348.

[FCGM04] T. Falter, W. Cassing, K. Gallmeister, and U. Mosel, *Hadron formation and attenuation in deep inelastic lepton scattering off nuclei*, Physics Letters B **594** (2004), no. 1-2, 61–68.

[FF89] A. Fabrocini and S. Fantoni, *Microscopic calculation of the longitudinal response of nuclear matter*, Nuclear Physics A **503** (1989), no. 2, 375–403.

[FLC84] J. M. Finn, R. W. Lourie, and B. H. Cottman, *Scaling violation in the separated response functions of* ^{12}C, Physical Review C **29** (1984), no. 6, 2230–2238.

[FN79] G. L. Fogli and G. Nardulli, *A new approach to the charged current induced weak one-pion production*, Nuclear Physics B **160** (1979), no. 1, 116–150.

[FP88] S. Fantoni and V. R. Pandharipande, *Orthogonalization of correlated states*, Physical Review C **37** (1988), no. 4, 1697–1707.

[G$^+$06] R. Gran et al., *Measurement of the quasielastic axial vector mass in neutrino interactions on oxygen*, Phys. Rev. D **74** (2006), no. 5, 052002.

[GF05] K. Gallmeister and T. Falter, *Space-time picture of fragmentation in PYTHIA/JETSET for HERMES and RHIC*, Physics Letters B **630** (2005), no. 1-2, 40–48.

[GiB] *GiBUU*, http://gibuu.physik.uni-giessen.de/GiBUU.

[GML60] M. Gell-Mann and M. Levy, *The axial vector current in beta decay*, Il Nuovo Cimento (1955-1965) **16** (1960), no. 4, 705–726.

[Gre00] W. Greiner, *Relativistic quantum mechanics: wave equations*, Springer Verlag, 2000.

[GW57] J. J. Griffin and J. A. Wheeler, *Collective motions in nuclei by the method of generator coordinates*, Physical Review **108** (1957), no. 2, 311–327.

[GY03] K. Gottfried and T. M. Yan, *Quantum mechanics: Fundamentals*, 2003.

[HL98] F. Hofmann and H. Lenske, *Hartree-Fock calculations in the density matrix expansion approach*, Physical Review C **57** (1998), no. 5, 2281–2293.

[HM08] F. Halzen and A. D. Martin, *Quark & leptons: An introductory course in modern particle physics*, Wiley India Pvt. Ltd., 2008.

[HNV07] E. Hernández, J. Nieves, and M. Valverde, *Weak pion production off the nucleon*, Physical Review D **76** (2007), no. 3, 33005.

[inc] *Quasielastic electron nucleus scattering archive*, http://faculty.virginia.edu/qes-archive/.

[Jou96] J. Jourdan, *Quasi-elastic response functions. the coulomb sum revisited*, Nuclear Physics A **603** (1996), no. 2, 117–160.

[K$^+$86] T. Kitagaki et al., *Charged-current exclusive pion production in neutrino-deuterium interactions*, Phys. Rev. D **34** (1986), no. 9, 2554–2565.

[K$^+$90] T. Kitagaki et al., *Study of $\nu d \to \mu^- pp$ and $\nu d \to \mu^- \Delta^{++}(1232)$ using the BNL 7-foot deuterium-filled bubble chamber*, Physical Review D **42** (1990), no. 5, 1331–1338.

[K$^+$05] C. Kraus et al., *Final results from phase ii of the mainz neutrino mass searchin tritium decay*, The European Physical Journal C **40** (2005), no. 4, 447–468.

[K2K] *K2K*, http://neutrino.kek.jp/.

[Kat09] T. Katori, *Measurement of muon neutrino charged current quasielastic (CCQE) double differential cross section in MiniBooNE,*, 2009, talk given at NUINT 09.

[KB62] L. P. Kadanoff and G. Baym, *Quantum statistical mechanics: Green's function methods in equilibrium and nonequilibrium problems*, Benjamin New York, 1962.

[Kel64] L. V. Keldysh, *Diagram technique for nonequilibrium processes*, Zh. Eksp. Teor. Fiz. **47** (1964), 1515–1527.

[KLN08] K. S. Kuzmin, V. V. Lyubushkin, and V. A. Naumov, *Quasielastic axial-vector mass from experiments on neutrino–nucleus scattering*, The European Physical Journal C **54** (2008), no. 4, 517–538.

[LBARM09] T. Leitner, O. Buss, L. Alvarez-Ruso, and U. Mosel, *Electron-and neutrino-nucleus scattering from the quasielastic to the resonance region*, Physical Review C **79** (2009), no. 3, 34601.

[LBMAR09] T. Leitner, O. Buss, U. Mosel, and L. Alvarez-Ruso, *Neutrino induced pion production at MiniBooNE and K2K*, Physical Review C **79** (2009), 038501.

[Leh03] J. Lehr, *In-medium Eigenschaften in semiklassischem Transportmodell*, Ph.D. thesis, Justus-Liebig-Universitaet Giessen, 2003, available for download at http://theorie.physik.uni-giessen.de/.

[Lei09] Tina J. Leitner, *Neutrino-nucleus interactions in a coupled-channel hadronic transport model*, Ph.D. thesis, Justus-Liebig-Universitaet Giessen, 2009, available for download at http://theorie.physik.uni-giessen.de/.

[LEM00] J. Lehr, M. Effenberger, and U. Mosel, *Electron and photon induced reactions on nuclei in the nucleon resonance region*, Nuclear Physics A **671** (2000), no. 1-4, 503–531.

[Leu00] S. Leupold, *Towards a test particle description of transport processes for states with continuous mass spectra*, Nuclear Physics A **672** (2000), no. 1-4, 475–500.

[LL83] L. D. Landau and E. M. Lifschitz, *Lehrbuch der Theoretischen Physik X - Physikalische Kinetik*, Akademie-Verlag, Berlin (1983).

[M+84] Z. E. Meziani et al., *Coulomb Sum Rule for ^{40}Ca, ^{48}Ca, and ^{56}Fe for $|\vec{q}| \leq 550$ MeV/c*, Physical Review Letters **52** (1984), no. 24, 2130–2133.

[MAB+09] C. Maieron, J. E. Amaro, M. B. Barbaro, J. A. Caballero, T. W. Donnelly, and C. F. Williamson, *Superscaling of non-quasielastic electron-nucleus scattering*, Physical Review C **80** (2009), no. 3, 35504.

[MAI] *MAID*, http://wwwkph.kph.uni-mainz.de/MAID/.

[Mar07] P. A. Markowich, *Applied partial differential equations: a visual approach*, Springer Verlag, 2007.

[MDS02] C. Maieron, T. W. Donnelly, and I. Sick, *Extended superscaling of electron scattering from nuclei*, Physical Review C **65** (2002), no. 2, 25502.

[MECM09] M. Martini, M. Ericson, G. Chanfray, and J. Marteau, *Unified approach for nucleon knock-out and coherent and incoherent pion production in neutrino interactions with nuclei*, Physical Review C **80** (2009), no. 6, 065501.

[MFM04] P. Muehlich, T. Falter, and U. Mosel, *Inclusive omega photoproduction off nuclei*, Eur. Phys. J. A **20** (2004), 499–508.

[Mina] *MiniBooNE*, http://www-boone.fnal.gov/.

[MINb] *MINOS*, http://www-numi.fnal.gov/.

[MM01] J. Morgenstern and Z. E. Meziani, *Is the coulomb sum rule violated in nuclei?*, Physics Letters B **515** (2001), no. 3-4, 269–275.

[Mos99] U. Mosel, *Fields, symmetries, and quarks*, Springer Verlag, 1999.

[MP04] R. N. Mohapatra and P. B. Pal, *Massive neutrinos in physics and astrophysics*, Imperial College Pr, 2004.

[MS92] D. M. Manley and E. M. Saleski, *Multichannel resonance parametrization of πN scattering amplitudes*, Physical Review D **45** (1992), no. 11, 4002–4033.

[MSW+71] E. J. Moniz, I. Sick, R. R. Whitney, J. R. Ficenec, R. D. Kephart, and W. P. Trower, *Nuclear Fermi momenta from quasielastic electron scattering*, Physical Review Letters **26** (1971), no. 8, 445–448.

[NO$^+$93] J. Nieves, C. Oset, et al., *A theoretical approach to pionic atoms and the problem of anomalies*, Nuclear Physics A **554** (1993), no. 4, 509–553.

[ODi] *ODic*, http://odic.sourceforge.net/.

[OPE] *OPERA*, http://operaweb.lngs.infn.it.

[Osb95] M. C. Osborn, *Kinematic scaling in quasielastic electron scattering*, Ph.D. thesis, Massachusetts Institute of Technology, 1995.

[PRSZ09] B. Povh, K. Rith, C. Scholz, and F. Zetsche, *Teilchen und Kerne: eine Einfuehrung in die physikalischen Konzepte*, Springer, 2009.

[PS82] E. Pace and G. Salme, *The nuclear scaling function and quasi-elastic electron scattering by nuclei*, Physics Letters B **110** (1982), no. 5, 411–414.

[PS95] M. E. Peskin and D. V. Schroeder, *An introduction to quantum field theory*, Westview Pr, 1995.

[Pyt] *Python*, http://www.python.org.

[R$^+$82] G. M. Radecky et al., *Study of single-pion production by weak charged currents in low-energy νd interactions*, Physical Review D **25** (1982), no. 5, 1161–1173.

[RC53] F. Reines and C. L. Cowan, *Detection of the free neutrino*, Physical Review **92** (1953), no. 3, 830–831.

[Ros80] R. Rosenfelder, *Quasielastic electron scattering from nuclei*, Annals of Physics **128** (1980), 188–240.

[RS81] D. Rein and L. M. Sehgal, *Neutrino-excitation of baryon resonances and single pion production*, Annals of Physics **133** (1981), no. 1, 79–153.

[RST] *REStructured Text, http://docutils.sourceforge.net/rst.html.*

[Sci] *Sciboone*, http://www-sciboone.fnal.gov/.

[SM72] R. A. Smith and E. J. Moniz, *Neutrino reactions on nuclear targets*, Nuclear Physics B **43** (1972), 605–622.

[Sre07] M. A. Srednicki, *Quantum field theory*, Cambridge University Press, 2007.

[STV08] T. Schwetz, M. Tortola, and J. W. F. Valle, *Three-flavour neutrino oscillation update*, New Journal of Physics **10** (2008), 113011.

[T2K] *T2K*, http://jnusrv01.kek.jp/public/t2k.

[TCE$^+$97] S. Teis, W. Cassing, M. Effenberger, A. Hombach, U. Mosel, and G. Wolf, *Pion-production in heavy-ion collisions at SIS energies*, Zeitschrift fuer Physik A Hadrons and Nuclei **356** (1997), no. 4, 421–435.

[Tei97] Stefan Teis, *Transporttheoretische Beschreibung von Schwerionenkollisionen*, Ph.D. thesis, Justus-Liebig-Universitaet Giessen, 1997, available for download at http://theorie.physik.uni-giessen.de/.

[W$^+$97] C. F. Williamson et al., *Quasielastic electron scattering from ^{40}Ca*, Physical Review C **56** (1997), no. 6, 3152–3172.

[W$^+$02] C. Weinheimer et al., *Katrin, a next generation tritium β decay experiment in search for the absolute neutrino mass scale*, Progress in Particle and Nuclear Physics **48** (2002), no. 1, 141–150.

[Wal74] J. D. Walecka, *A theory of highly condensed matter*, Annals of Physics **83** (1974), no. 2, 491–529.

[WAT03] A. H. Wapstra, G. Audi, and C. Thibault, *The 2003 atomic mass evaluation: (i). evaluation of input data, adjustment procedures*, Nuclear Physics A **729** (2003), no. 1, 129–336, The 2003 NUBASE and Atomic Mass Evaluations.

[Wes75] G. B. West, *Electron scattering from atoms, nuclei and nucleons*, Physics Reports **18** (1975), 263–323.

[WLM05] M. Wagner, A. B. Larionov, and U. Mosel, *Kaon and pion production in relativistic heavy-ion collisions*, Physical Review C **71** (2005), no. 3, 34910.

[WPK$^+$88] G. M. Welke, M. Prakash, T. T. S. Kuo, S. Das Gupta, and C. Gale, *Azimuthal distributions in heavy ion collisions and the nuclear equation of state*, Physical Review C **38** (1988), no. 5, 2101–2107.

Deutsche Zusammenfassung

Die vorliegende Arbeit beschäftigt sich mit der Streuung von Leptonen an Kernen. Leichte Leptonen, also Elektronen und Neutrinos, sind bestens als Sonde zur Untersuchung der Eigenschaften von Kernen und Nukleonen geeignet, da sie nur elektroschwach mit diesen wechselwirken und zudem nicht im Vakuum zerfallen. Demgegenüber haben hadronische Sonden, z.B. Pionen, den Nachteil, dass sie auch an der starken Wechselwirkung teilnehmen, die für den Zusammenhalt von Nukleonen verantwortlich ist. Sowohl Kerne als auch Nukleonen stellen Grundbausteine der Materie dar, die sich als komplex gekoppelte Vielteilchensysteme bisher einer umfassenden theoretischen Beschreibung entziehen. Die weitere Erforschung ihrer Eigenschaften ist daher ein wichtiges Ziel im Sinne der Grundlagenforschung.

Streuprozesse von Neutrinos und Kernen sind auch aus einem anderen Grund interessant. Die Entdeckung von Neutrinooszillationen hat aufgezeigt, dass Neutrinos eine zwar kleine aber von Null verschiedene Masse besitzen und zudem von der schwachen Wechselwirkung nur in einer Mischung aus drei Massezuständen an andere Teilchen gekoppelt werden. Weder die Massen noch die Mischungsverhältnisse sind bis dato mit hinreichender Genauigkeit bekannt, so dass eine Lücke in dem Verständnis der elementaren Bausteine der Natur klafft. Streuexperimente mit Neutrinos können helfen, diese Unsicherheiten zu beseitigen. Mehrere Experimente dieser Art werden derzeit weltweit durchgeführt bzw. vorbereitet.

Da Neutrinos nur schwach mit Materie wechselwirken, sind bei der Analyse von solchen Experimenten bestimmte Eigenschaften, wie z.B. die Energie der einfallenden Teilchen, nur indirekt, unter Verwendung von Modellannahmen, zu bestimmen. Folglich ist das theoretische Verständnis der Vorgänge im Kern und seiner Reaktion auf elektroschwache Anregungen unerlässlich, bzw. noch nicht ausreichend, da bestimmte nukleare Eigenschaften, die auch schon bei elektromagnetischer Anregung auftreten, bis dato nicht konsistent beschrieben werden können.

Das Ziel dieser Arbeit ist est es, zu dem Verständnis der Wechselwirkung von Leptonen mit Kernen beizutragen. Dazu wird mit Hilfe des GiBUU-Modells eine numerische Simulation des Streuprozesses vorgenommen, bei der Annahmen über den Grundzustand des Kerns und die Funktionsweise der Wechselwirkung eine entscheidende Rolle spielen. Durch Vergleich mit experimentellen Daten für Elektron-Streuprozesse können wir mehr über die Auswirkungen dieser Annahmen herausfinden und zudem unsere Vorhersagen für Neutrino-Streuprozesse besser einschätzen. Dabei können durch Anwendungen besonderer Analyseverfahren, z.B. der *superscaling*-Analyse oder der Separation der longitudinalen und der transversalen Antwortfunktionen, weitere Erkenntnisse gewonnen werden.

Danksagung

In erster Linie möchte ich meinen Betreuern Dr. Hendrik van Hees und Prof. Dr. Ulrich Mosel für die Möglichkeit danken, in einem spannenden und aktuellen Gebiet der Froschung meine Diplomarbeit schreiben zu können. Besonderer Dank gilt Prof. Dr. Ulrich Mosel für Impulse, die den Fokus der Forschung auf die wichtigen Ziele lenkten, und sein Bemühen um die Vermittlung guter wissenschaftliche Methodik. Dem Verständnis der zugrundeliegenden Physik waren die Gespräche mit Dr. Hendrik van Hees sehr zuträglich und der Stil dieser Arbeit hat stark von seinen genauen Korrekturen profitiert.

Zutiefst zu Dank verpflichtet bin ich Dr. Tina Leitner, auf deren Forschung die vorliegende Arbeit aufbaut und die sich auch nach einem Wechsel des Arbeitgebers die Zeit für eine Korrektur dieser Arbeit genommen hat. Die Gespräche mit ihr waren für das Überwinden von einigen konzeptionellen und technischen Hürden unerlässlich. Zudem waren ihre herausragenden wissenschaftlichen Leistungen eine Quelle der Inspiration.

Danken möchte ich auch Fabian Eichstädt, der mir dabei half, meine Ideen im Bezug auf die effiziente Nutzung der Computer-Infrastruktur umzusetzen, auch wenn sie sich manchmal von der gängigen Vorgehensweise unterschieden. Auch bei allgemeinen methodischen Fragen waren seine Ratschläge hilfreich. Ebenso sei Janus Weil, Kai Gallmeister und Theo Gaitanos gedankt für die Hilfe bei Problemen rund um das Thema Hard- und Software, insbesondere in Bezug auf den GiBUU-Code. Dank geht an meine ZimmergenossInnen Carla Terschlüssen und Jan Fokken, für die angenehme Arbeitsathmosphäre und anregende Gespräche. Insgesamt danke ich den Mitarbeitern des Instituts für den respektvollen und freundlichen Umgang miteinander.

Ein großer Dank geht an Elke Jung, die sich, freundlich, zeitnah und gekonnt zugleich, um organisatorische Fragen gekümmert hat. Zudem danke ich Barbara Thörner und Birgit Bernhardt vom naturwissenschaftlichen Prüfungsamt, sowie Prof. Dr. Winfried Stute, dafür, dass ich in dem Beschluss ein Doppeldiplom in Physik und Mathematik anzustreben bestärkt und bei dessen Durchführung unsterstützt worden bin. Allen Beteiligten möchte ich für das Verständnis danken, welches mir das Engagement im Allgemeinen Studierendenausschuss während des Studiums ermöglicht hat.

Aus meinem Semester möchte ich insbesondere Pierre-Michel Hillenbrand danken. Die Zusammenarbeit mit ihm, ob in Lerngruppen, Projekten oder physikalischen Praktika, verlief konstruktiv und anregend. Sie trug wesentlich zur Vertiefung des Verständnisses und dem Erfolg des Studiums als Ganzes bei. Als Glanzlicht der Zusammenarbeit sticht das gemeinsame ERASMUS-Austauschsemester in Bordeaux, Frankreich, heraus, das unter aktiver Unterstützung von Prof. Dr. Alfred Müller zustande kam.

Natürlich wäre dieses fordernde Studium nicht ohne die moralische Unterstützung seitens der mir nahestehenden Menschen, seitens meiner Freundin, meiner Familie und guter Freunde, zu bewältigen gewesen. Ihnen gilt mein besonderer Dank.

Erklärung zur Urheberschaft

Ich erkläre hiermit, dass ich die vorliegende Arbeit selbstständig verfasst habe und dabei keine anderen als die angegebenen Quellen und Hilfsmittel zum Einsatz kamen.

Gießen, den 8.11.2010,

Ivan Lappo-Danilevski